

Material modification and characterization based on small molecule diffusion

by

Herman Coceancigh

B.S., Universidad de Buenos Aires, 2013

AN ABSTRACT OF A DISSERTATION

submitted in partial fulfillment of the requirements for the degree

DOCTOR OF PHILOSOPHY

Department of Chemistry
College of Arts and Sciences

KANSAS STATE UNIVERSITY
Manhattan, Kansas

2020

Abstract

This dissertation shows the use of small molecule diffusion as a method to control the modification inside poly(ethylene terephthalate) (PET) track-etched membrane pores and to unveil unique qualities of polystyrene-*block*-poly(ethylene oxide) (PS-*b*-PEO). The first project took advantage of electrochemical control of the diffusion length of a Cu (I) catalyst for azide-alkyne cycloaddition click reaction. By controlling the diffusion time of the catalyst generated at an underlying electrode, the modification along 1 μm pores in a PET track-etched membrane could be controlled. The complex of Cu(I) and tris[(1-benzyl-1H-1,2,3-triazol-4-yl)methyl]amine (TBTA) was used as the catalyst for the click reaction between an azide-tagged fluorescent dye and an alkyne group immobilized on the inner surface of the pore. The resulting surface modification was assessed by fluorescence microscopy. This approach was applicable to the asymmetric modification of cylindrical pores with two different fluorescent dyes in the opposite directions and for the selective visualization of the tip and base opening of conical pores. The cross-sectional fluorescence profile of the modified pores confirmed an increase in the surface modification yield for the longer duration of Cu(I) production. The second project measured the diffusion of sulforhodamine B (SRB) inside the PEO microdomains of thin PS-*b*-PEO films. The diffusion of SRB revealed the unique swelling properties of thin PS-*b*-PEO films under ethanol or water vapor. Specifically, the effects of swelling of the PEO microdomains were studied using spectroscopy ellipsometry (SE), single molecule tracking (SMT) and fluorescence correlation spectroscopy (FCS). Results for PS-*b*-PEO were compared with those for a polystyrene homopolymer (hPS_{16.4}) and poly(ethylene oxide) homopolymers (hPEO_{12.5} and hPEO_{3.8}) to confirm the unique swelling behavior. The results showed that while ethanol vapor could swell neither hPS_{16.4} nor hPEO_{12.5} thin films, it could swell the PEO microdomains. Water vapor could swell both the PEO microdomains and the hPEO_{12.5}. SE and SMT videos confirmed the swelling of the PEO microdomains. The immutability of hPS_{16.4} and the PS microdomains of PS-*b*-PEO under these solvent vapors was confirmed from the fluorescence emission of solvatochromic Nile Red (NR) using two-color wide-field microscopy. Furthermore, FCS was used to quantitatively assess swelling-induced changes in diffusion behavior of SRB in PEO microdomains. FCS results showed that hPEO_{12.5} was not swollen by ethanol vapor but smaller PEO microdomains were swollen more significantly, the latter of which was suggested by the SRB diffusion. These two projects strongly relied on the use of small molecule diffusion to control the length of pore surface modification and to verify the unique swelling of the PEO microdomains, respectively.

Material modification and characterization based on small molecule diffusion

by

Herman Coceancigh

B.S., Universidad de Buenos Aires (UBA), 2013

A DISSERTATION

submitted in partial fulfillment of the requirements for the degree

DOCTOR OF PHILOSOPHY

Department of Chemistry
College of Arts and Sciences

KANSAS STATE UNIVERSITY
Manhattan, Kansas

2020

Approved by:

Major Professor
Dr. Takashi Ito

Copyright

© Herman Coceancigh 2020.

Abstract

This dissertation shows the use of small molecule diffusion as a method to control the modification inside poly(ethylene terephthalate) (PET) track-etched membrane pores and to unveil unique qualities of polystyrene-*block*-poly(ethylene oxide) (PS-*b*-PEO). The first project took advantage of electrochemical control of the diffusion length of a Cu (I) catalyst for azide-alkyne cycloaddition click reaction. By controlling the diffusion time of the catalyst generated at an underlying electrode, the modification along 1 μm pores in a PET track-etched membrane could be controlled. The complex of Cu(I) and tris[(1-benzyl-1H-1,2,3-triazol-4-yl)methyl]amine (TBTA) was used as the catalyst for the click reaction between an azide-tagged fluorescent dye and an alkyne group immobilized on the inner surface of the pore. The resulting surface modification was assessed by fluorescence microscopy. This approach was applicable to the asymmetric modification of cylindrical pores with two different fluorescent dyes in the opposite directions and for the selective visualization of the tip and base opening of conical pores. The cross-sectional fluorescence profile of the modified pores confirmed an increase in the surface modification yield for the longer duration of Cu(I) production. The second project measured the diffusion of sulforhodamine B (SRB) inside the PEO microdomains of thin PS-*b*-PEO films. The diffusion of SRB revealed the unique swelling properties of thin PS-*b*-PEO films under ethanol or water vapor. Specifically, the effects of swelling of the PEO microdomains were studied using spectroscopy ellipsometry (SE), single molecule tracking (SMT) and fluorescence correlation spectroscopy (FCS). Results for PS-*b*-PEO were compared with those for a polystyrene homopolymer (hPS_{16.4}) and poly(ethylene oxide) homopolymers (hPEO_{12.5} and hPEO_{3.8}) to confirm the unique swelling behavior. The results showed that while ethanol vapor could swell neither hPS_{16.4} nor hPEO_{12.5} thin films, it could swell the PEO microdomains. Water vapor could swell both the PEO microdomains and the hPEO_{12.5}. SE and SMT videos confirmed the swelling of the PEO microdomains. The immutability of hPS_{16.4} and the PS microdomains of PS-*b*-PEO under these solvent vapors was confirmed from the fluorescence emission of solvatochromic Nile Red (NR) using two-color wide-field microscopy. Furthermore, FCS was used to quantitatively assess swelling-induced changes in diffusion behavior of SRB in PEO microdomains. FCS results showed that hPEO_{12.5} was not swollen by ethanol vapor but smaller PEO microdomains were swollen more significantly, the latter of which was suggested by the SRB diffusion. These two projects strongly relied on the use of small molecule diffusion to control the length of pore surface modification and to verify the unique swelling of the PEO microdomains, respectively.

Table of Contents

List of Figures	ix
List of Tables	xvii
Acknowledgements	xviii
Dedication	xx
Preface	xxi
Acronyms and Definitions	xxii
1. Introduction.....	1
2. Diffusion	3
2.1 Small Molecule Diffusion.....	3
2.2 Diffusion Coefficient Measurement	6
2.2.1 Historical View	6
2.2.2 Fluorescence Based Methods.....	7
2.2.2.1 Fluorescence	7
2.2.2.1.1 Solvatochromism.....	10
2.2.2.2 Fluorescence Microscopy	12
2.2.2.3 Fluorescence Correlation Spectroscopy (FCS).....	15
2.2.2.3.1 FCS General Formalism.....	16
2.2.2.3.2 Instrumentation of FCS Measurements.....	20
2.2.2.3.3 FCS Data Analysis	21
2.2.2.4 Single Molecule Tracking (SMT).....	24
2.2.2.4.1 Instrumentation of SMT	28
2.2.2.4.2 Diffusion Coefficient Calculations from Trajectories.....	29
2.2.2.4.3 Manual Spot Detection and Linking	31
2.2.2.4.4 Automated Spot Detection and Linking.....	31
3. Materials and Characterization Methods	33
3.1 Poly(ethylene terephthalate) Track-Etched Membrane	34
3.1.1 Poly(ethylene terephthalate) (PET).....	34
3.1.1.1 Track-Etched Membrane Fabrication	34
3.2 Block Copolymers	35

3.2.1	Polystyrene- <i>block</i> -Poly(ethylene oxide) (PS- <i>b</i> -PEO).....	37
3.2.1.1	Polystyrene (PS).....	37
3.2.1.2	Poly(ethylene oxide) (PEO).....	38
3.3	Instrumentation Used for Material Preparation and Characterization.	39
3.3.1	Sample Preparation Methods.	39
3.3.1.1	Spin Coating.....	39
3.3.2	Sample Characterization	40
3.3.2.1	Spectroscopic Ellipsometry (SE)	41
3.3.2.2	Sample Characterization Using Microscopy	43
3.3.2.2.1	Fluorescence Microscopy.....	44
3.3.2.2.2	Atomic Force Microscopy (AFM)	44
3.3.2.3	Electrochemical Methods.....	45
3.3.2.3.1	Cyclic voltammetry (CV).....	46
4.	Longitudinally Controlled Modification of Cylindrical and Conical Track-Etched Poly(ethylene terephthalate) Pores Using and Electrochemically Assisted Click Reaction ¹⁶⁷	49
4.1	Contribution of Authors	49
4.2	Introduction.....	49
4.3	Experimental Procedures	52
4.3.1	Chemicals and Materials.....	52
4.3.2	Fabrication of a Comb-Shaped Gold Electrode	53
4.3.3	Pore Modification	54
4.3.4	Electrochemically-Controlled Modification	55
4.3.5	Fluorescence Microscopy Measurements	57
4.3.6	Finite-Element Computer Simulations	58
4.3.7	Computational Procedure.....	60
4.4	Results and Discussion	65
4.4.1	Finite-Element Computer Simulations	67
4.4.2	Effects of Reduction Step Time on Cylindrical Pore Modification.....	70
4.4.3	Asymmetric Modification with Two Fluorescent Dyes in Opposite Directions ..	74
4.4.4	Asymmetric Modification of Conical Pores	76

4.4.5	Further Control of the Pore Modification	77
4.5	Conclusions.....	80
5.	Unique Swelling Properties of PS- <i>b</i> -PEO Thin Films	82
5.1	Contribution of Authors.....	82
5.2	Introduction.....	82
5.3	Experimental Procedure.....	85
5.3.1	Chemicals and Materials.....	85
5.3.2	Sample Preparation	85
5.3.3	FCS Measurements	86
5.3.4	SMT Measurements.....	87
5.3.5	Ellipsometry Measurements.....	87
5.3.6	Two-Color Imaging.....	88
5.3.6.1	Two-Color Ensemble Imaging.....	89
5.3.6.2	Two-Color Single-Molecule Imaging.....	89
5.3.7	Fluorescence Spectroscopic Measurements for Thin Films	89
5.4	Results and Discussion	90
5.4.1	AFM Images	90
5.4.2	Spectroscopic Ellipsometry Data.....	91
5.4.3	SMT Measurements for SRB-Doped Thin Films	95
5.4.3.1	SMT Data Analysis with the “Manual Method”.....	98
5.4.3.2	SMT Data Analysis with the “Software-Based Method”	99
5.4.4	FCS Data for SRB.....	102
5.4.5	Two-Color Imaging	104
5.4.5.1	Two-Color Ensemble Imaging.....	104
5.4.5.2	Nile Red Single Molecule Spectroscopic Imaging.....	108
5.4.6	Nile Red Spectroscopic Measurements in Thin Films.....	111
5.5	Conclusions.....	112
6.	General Conclusion and Future Directions.....	114
	References.....	120
	Appendix A -Spectroscopic Ellipsometry in Time-.....	136

List of Figures

- Figure 2-1: Jablonski diagram for fluorescence emission. This diagram only considers electronic and vibrational states. For simplification, rotational states, spins and phosphorescence decay through triplet states, are not shown..... 7
- Figure 2-2: (a) Fluorescence emission spectra for a series of Nile Red solutions. The toluene solution is shown in blue, showing maxima emission (λ_{em}) peak of ≈ 580 nm, and in red the ethanolic solution of Nile Red is showing the red shift with a $\lambda_{em} \approx 625$ nm. (b) Plot of the E value (emission ratio) against the Claussious-Mossotti factor for the series of Nile Red solutions with mixed solvents (different rations of ethanol:toluene). Reproduced with permission from Ref. ⁴⁵. Copyright 2014 American Chemical Society..... 10
- Figure 2-3: (a) Wide-field microscopy setup with a laser beam (in green) as excitation light; a beam splitter, and a CCD camera as a detector; (b) Wide-field sample illumination; (c) Confocal microscopy setup with a laser beam (in green) as excitation light; a pinhole (for 3D imaging) and an avalanche photo diode (APD) as a detector; (d) Single-point sample illumination..... 14
- Figure 2-4: (a) Representative data from an FCS experiment. Fluorescence signal (F) is in counts per unit time (1 msec) measured with an APD detector, against time (t). (b) An autocorrelation function obtained from the data. The blue dots are values calculated for the autocorrelation function and the red line is the fitting function (in this case anisotropic 3D).
22
- Figure 2-5: Scheme of the laser illumination exploration from a single fluorescent probe. ... 24
- Figure 2-6: Schematic of the single molecule localization enhancement. Reproduced with permission from Ref. ⁹¹. Copyright 2014 Taylor & Francis. 26
- Figure 2-7: SMT process, from spot identification to spot linking across consecutive frames in a video. (a) shows how a video can be thought of as a consecutive series of frames in an time axis(τ); (b) is the identification of the single fluorescent molecules spot in each consecutive frames; (c) shows linking of the spots by “the closest one” method to create trajectories; (d) shows a plot of MSD against time (τ) to obtain the diffusion coefficient from the slope of the plot. 30

Figure 2-8: Schematic of how a crossing molecule can lead to erroneous trajectories. The top 3 frames show consecutive frames for one molecule (in blue). The trajectory from the single molecule is shown as “real trajectory”. However, a new molecule (in red) appears in frame 2, giving a “bad” linking as indicated by “created trajectory” for comparison. 32

Figure 3-1: Molecule structures of poly(ethylene terephthalate) (PET), polystyrene (PS), poly(ethylene oxide) (PEO) and polystyrene-*block*-poly(ethylene oxide) (PS-*b*-PEO), which were used in the projects of this thesis..... 33

Figure 3-2: (a) Synthesis of PET. (b) Fabrication of a PET track-etched membrane. Polymer PET sheet is bombarded by heavy ions and the resulting nuclear tracks are etched to get pores of a desired size. Stopping solution serves to neutralize the basic solution and stop the etching process..... 35

Figure 3-3: Theoretical phase diagram for a linear DBC calculated using self-consistent mean-field theory. DBC morphologies depending on the volume fraction are also shown: From right to the left: sphere (S), cylinder (C), gyroid (G), and lamella (L). For a volume fraction larger than 0.5, the inverse structure is expected. Reproduced with permission from Ref ¹²⁸. Copyright 2010 Elsevier. 36

Figure 3-4: Spin coating process to form a thin film from a polymer solution. (i) A solution is placed on a substrate; (ii) The substrate is spun to remove excess solution; (iii) The solvent remaining on the substrate is evaporated by airflow during spinning; (iv) A uniform thin film is formed after being completely dried. 40

Figure 3-5: Experimental set up of spectroscopic ellipsometry. 41

Figure 3-6: Experimental setup of AFM. The position of the tip on the sample surface is controlled by the piezoelectric stage, and the vertical and torsional deflection of the cantilever is measured from the position of a laser beam reflected on the cantilever. 44

Figure 3-7: Scheme of a galvanic cell with a cathode and an anode. Copper (II) ions in the right solution gains electrons at the copper electrode while zinc at the zinc electrode loses electrons to be zinc (II) ions, making the electrons flow from the zinc electrode to the copper electrode. 46

Figure 3-8: (a) Typical triangular potential waveform application. Point *a* refers to the initial potential ($E_{initial}$); *b* to the potential at the cathodic peak current (i_c); *c* is the returning potential (E_{return}); *d* is the anodic peak current (i_a); and *e* is the initial potential (E_{final}). (b)

Typical cyclical voltammogram. Reproduced with permission from Ref. ¹⁵. Copyright 2001 Wiley. 47

Figure 4-1: (a) Electrochemically-controlled pore modification based on CuAAC. (b) Chemical structures of azide-tagged fluorescent dyes and TBTA, a ligand to Cu(II/I). Reproduced with permission from Ref. ¹⁶⁷. Copyright 2017 American Chemical Society.. 52

Figure 4-2: (a) Scheme of the fabrication procedure, (b) image of the electrode pattern used, and (c) photo of the final electrode as it was used for the experiments..... 54

Figure 4-3: (a) Schematic illustration of an experimental setup used in this study. The experiments were carried out using a two-electrode cell consisting of a planar Au (counter/reference) electrode (CE/RE) at the top, a comb-shaped or planar Au (working) electrode (WE) at the bottom and a PET track-etched membrane sandwiched in between. (b) Potentials applied to the WE in the two-electrode cell. At the WE, Cu(II) was reduced to Cu(I) ($0 \leq t < \tau$; $t_1 = \tau$), and then the generated Cu(I) was oxidized to Cu(II) ($\tau \leq t \leq 3\tau$; $t_2 = 2\tau$). (c) A cyclic voltammogram recorded in a H₂O/DMSO (1:1) solution containing 1 mM CuSO₄, 1 mM TBTA and 0.1 M NaBF₄ using a two-electrode cell consisting of two Au disk electrodes (2 mm in diameter). Reproduced with permission from Ref. ¹⁶⁷. Copyright 2017 American Chemical Society. 56

Figure 4-4: Fluorescence microscopy setups used for recording (a) a planar image and (b) a cross-sectional image. Modified areas in a membrane reflecting the positions of the teeth of a comb-shaped WE during the pore modification are schematically shown in pink. Reproduced with permission from Ref. ¹⁶⁷. Copyright 2017 American Chemical Society.. 57

Figure 4-5: (a) Assumed hexagonal arrangement of the pores in the PET track-etched membrane with cylindrical pores (1 μm in diameter). The center-to-center distance of 2.2 μm was estimated from the pore density (0.25 pores/μm²). (b) Schematic illustration of the simulation geometry of a cylindrical pore between two electrodes: The pore radius was 0.5 μm, the pore length defined by the membrane thickness was 22 μm, and the electrode-membrane gap was d ($= 0, 0.1$ or $1 \mu\text{m}$). The origin of the cylindrical coordinate system was set on the WE at the center of the pore. Reproduced with permission from Ref. ¹⁶⁷. Copyright 2017 American Chemical Society. 58

Figure 4-6: (a) Model geometry ($d = 1 \mu\text{m}$) showing eight boundaries (1-8) and one domain (9). (b) Illustration of the mesh size used in the COMSOL simulations for the

- functionalization of a pore (0.5 μm in radius, 22 μm in length, $d = 1 \mu\text{m}$). The model was built by Dr. Khanh-Hoa Tran-Ba. Reproduced with permission from Ref. ¹⁶⁷. Copyright 2017 American Chemical Society. 61
- Figure 4-7: COMSOL simulation results on the time dependence of Cu(I) concentration profile within a pore (0.5 μm wide, 22 μm high, $d = 0$) at different t for different t_1-t_2 conditions. The Cu(I) concentration ranges from 0 mol/m³ (blue) to 1 mol/m³ (red). The bottom boundary represents the WE. The data were obtained by Dr. Khanh-Hoa Tran-Ba. Reproduced with permission from Ref. ¹⁶⁷. Copyright 2017 American Chemical Society.. 63
- Figure 4-8: COMSOL simulation results ($d = 0$) on the effects of t_1-t_2 conditions ($t_1 = \tau$, $t_2 = 2\tau$) on surface modification yield, $R(z)$, during the reduction step ($0 \leq t < \tau$, dotted line), during the re-oxidation step ($\tau \leq t \leq 3\tau$, dashed line), and after both the reduction and subsequent re-oxidation steps ($0 \leq t \leq 3\tau$, solid line). The data were obtained by Dr. Khanh-Hoa Tran-Ba. Reproduced with permission from reference ¹⁶⁷. Copyright 2017 American Chemical Society. 64
- Figure 4-9: COMSOL simulation results on the effects of d on $R(z-d)$ at three different t_1-t_2 conditions. The data were obtained by Dr. Khanh-Hoa Tran-Ba. Reproduced with permission from Ref. ¹⁶⁷. Copyright 2017 American Chemical Society. 65
- Figure 4-10: COMSOL simulation results ($d = 0$) on (a) Cu(I) concentration, $C_1(0,z,t_1)$, along the center of the pore after the reduction step ($t_1 = \tau$), (b) surface modification yield, $R(z)$, after the reduction and re-oxidation steps ($t_1 = \tau$, $t_2 = 2\tau$), and (c) normalized surface modification yield, $R(z)/R(0)$, obtained from (b). The data were obtained by Dr. Khanh-Hoa Tran-Ba. Reproduced with permission from Ref. ¹⁶⁷. Copyright 2017 American Chemical Society. 68
- Figure 4-11: (a) Typical planar fluorescence images of PET track-etched membranes (1 μm in cylindrical pore diameter) modified with Azide-fluor 545 for $\tau = 30$ sec, $\tau = 120$ sec, $\tau = 360$ sec and $\tau = 1000$ sec. Recorded using a 10x objective lens with a TRITC filter set for the same integration time (5 sec) in the same day. The inset shows a typical fluorescence intensity profile across the inter-electrode region obtained from each planar image. The definition of ΔI is given in the intensity profile for $\tau = 1000$ sec. (b) τ -dependence of ΔI (average \pm 95% confidence interval) obtained from 11-22 different pairs of modified-unmodified regions in a membrane. The low ΔI at $\tau = 60$ sec might be due to the

insufficient removal of air between the membrane and WE. Reproduced with permission from Ref. ¹⁶⁷. Copyright 2017 American Chemical Society..... 71

Figure 4-12: (a) A typical cross-sectional fluorescence image of a PET track-etched membrane (1 μm in cylindrical pore diameter, *ca.* 22 μm thick) modified with Azide-fluor 545 from a homogeneous solution for 1000 sec. Cu(I) was generated via the reduction of Cu(II) by L-ascorbic acid. Recorded using a 100x oil immersion objective lens and a TRITC filter set. (b) An averaged cross-sectional profile obtained from (a). Reproduced with permission from Ref. ¹⁶⁷. Copyright 2017 American Chemical Society..... 72

Figure 4-13: (a) Typical cross-sectional fluorescence images of PET track-etched membranes (1 μm in cylindrical pore diameter, *ca.* 22 μm thick) modified with Azide-fluor 545 for $\tau = 10$ sec, $\tau = 120$ sec, $\tau = 360$ sec and $\tau = 1000$ sec. The bottom side in each image was in contact to a comb-shaped electrode during CuAAC. Recorded using a 10x objective lens with a TRITC filter set for the same integration time (1 sec) in the same day. (b) Cross-sectional fluorescence intensity profile across each membrane shown in (a). The red and orange profiles, reflecting electrode-contact and inter-electrode regions during CuAAC, respectively, were obtained by averaging the profiles in the regions shown by squares in (a). The definitions of fluorescence intensity slope and I_{max} are given in the inset for $\tau = 360$ sec. (c) τ -dependence of fluorescence intensity slope (average \pm 95% confidence interval) obtained from modified regions in a membrane by 4-9 different electrode teeth. (d) τ -dependence of I_{max} (average \pm 95% confidence interval) obtained from modified regions in a membrane by 4-9 different electrode teeth. Reproduced with permission from Ref. ¹⁶⁷. Copyright 2017 American Chemical Society. 73

Figure 4-14: (a) Typical planar fluorescence images of a PET track-etched membrane (1 μm in cylindrical pore diameter, *ca.* 22 μm thick) modified with Azide-fluor 545 for $\tau = 30$ sec, followed by Azide-fluor 488 for $\tau = 30$ sec. The upper two images and the bottom two images were recorded at the same areas through the FITC (left) and TRITC (right) filter sets. Recorded using a 100x oil immersion objective lens for the same integration time (1 sec). (b) Cross-sectional fluorescence images of the PET track-etched membrane recorded at the same area using the FITC (left) and TRITC (right) filter sets. The upper and bottom faces were in contact to a comb-shaped electrode during the modification with Azide-fluor 545 and Azide-fluor 488, respectively. Recorded using a 100x oil immersion objective lens

for the same integration time (0.5 sec). (c) Averaged cross-sectional fluorescence intensity profiles across the membrane shown in (b). Reproduced with permission from Ref. ¹⁶⁷.

Copyright 2017 American Chemical Society. 75

Figure 4-15: (a) SEM images of a PET track-etched membrane with conical pores. (left) Base-side surface image; (right) cross-sectional image. The TEM images were obtained by Natasha Siepser and Prof. Lane A. Baker. (b) Schematic illustration on electrochemically-controlled modification of PET track-etched conical pores with Azide-fluor 545 via CuAAC. Two pieces of membranes (*ca.* 0.5 x 1 cm²) were obtained by cutting a large membrane (*ca.* 1 x 1 cm²). One of them was modified from the tip side, and the other was modified from the base side. (c) Planar fluorescence (left) and optical transmission (right) images recorded at the same areas of PET track-etched membranes with conical pores modified from the base side (upper) and the tip side (lower) for $\tau = 1000$ sec. Recorded using a 100x oil immersion objective lens with a TRITC filter set for the same integration time (15 sec for the fluorescence images; 0.5 sec for the optical images). Reproduced with permission from Ref. ¹⁶⁷. Copyright 2017 American Chemical Society. 77

Figure 4-16: (a) CV obtained in a H₂O/DMSO (1:1) solution containing 1 mM CuSO₄, 1 mM TBTA and 0.1 M NaBF₄ with and without H₂O₂. (b) Planar and cross section analysis of the modification of the membrane modified with Azide-fluor 545 in the presence and absence of H₂O₂. 79

Figure 4-17: Potential steps examined to achieve better control of the modification length. ... 80

Figure 5-1: Experimental setup for spectroscopic ellipsometry measurements of polymer thin films under controlled atmosphere..... 88

Figure 5-2: (a) Typical AFM topographic images of three different dried thin films of PS_{15.5}-*b*-PEO₄ and PS₃₅-*b*-PEO_{10.5} before exposure to ethanol/water vapor (top), after exposure to ethanol vapor (middle) and after exposure to water vapor (bottom). Film thickness = 106 nm (PS_{15.5}-*b*-PEO₄.) and 118 nm (PS₃₅-*b*-PEO_{10.5}). $\Delta z = 10$ nm. 91

Figure 5-3: Typical time course data obtained with spectroscopic ellipsometry measurements (upper: refractive index at 632.8 nm; bottom: thickness) for thin polymer films upon exposure to ethanol vapor (highlighted in red) and water vapor (highlighted in blue). The films were exposed to nitrogen during the unhighlighted periods..... 93

Figure 5-4:	Optical images of a 100 nm thick hPEO _{3.5} film after each solvent exposure condition. The right image shows how the film is destroyed after exposure to water.....	94
Figure 5-5:	Plots for thickness gain (in nm) against initial thickness (in nm) for thin films of hPS _{16.4} ; hPEO _{12.5} ; PS _{35-b} -PEO _{10.5} ; PS _{13.5-b} -PEO ₄ (from left to right). The insets show expanded plots. Individual data points correspond to data obtained from individual different films. Thickness gain was calculated by subtracting initial film thickness from film thickness obtained after solvent vapor exposure.	95
Figure 5-6:	The upper row shows an increase in the number of the fluorescent spots with increasing SRB concentration, which supports the detection of single molecules. The middle row shows typical fluorescence images for thin SRB-doped films of hPEO _{12.5} , hPS _{12.5} , PS _{13.5-b} -PEO ₄ and PS _{35-b} -PEO _{10.5} (0.4 nM SRB; 100 nm film thickness). Bottom images are typical data obtained for thin PS _{35-b} -PEO _{10.5} films imaged under dry condition and ethanol or water vapor. All the images are 16 x 16 μm ²	96
Figure 5-7:	A trajectory of a SRB molecule in a PS _{35-b} -PEO _{10.5} film under ethanol vapor that was obtained using the “manual method”.....	99
Figure 5-8:	(A) Schematic trajectories of mobile and immobile molecules. The former shows larger displacements (step sizes). (B) Histograms of single molecule displacements for SRB molecules in thin films of hPEO _{12.5} (top), PS _{13.5-b} -PEO ₄ (middle) and PS _{35-b} -PEO _{10.5} (bottom) under N ₂ (left, black), water vapor (center, blue) and ethanol vapor (right, red). 100	
Figure 5-9:	Histograms for $D_{LabView}$ values obtained in thin films of hPEO _{12.5} (top), PS _{13.5-b} -PEO ₄ (middle) and PS _{35-b} -PEO _{10.5} (bottom) under N ₂ (left, black), water vapor (center, blue) and ethanol vapor (right, red).	102
Figure 5-10:	Left: Typical fluorescent time course data for hPEO _{12.5} , PS _{35-b} -PEO _{10.5} and PS _{13.5-b} -PEO ₄ films under water vapor and ethanol vapor. Right: Autocorrelation functions obtained from the time course data for each polymer and condition.....	103
Figure 5-11:	Typical two-color images for the three polymers under three vapor conditions. Left: 625 ± 20 nm; Right: 580 ± 20 nm. Film thickness: <i>ca.</i> 100 nm. Image size 16 x 16 μm ²	
		105
Figure 5-12:	(a) Relationship between $E_{ensemble}$ and film thickness for hPS _{16.4} . (b,c,d) $E_{ensemble}$ for (b) hPS _{16.4} , (c) hPEO _{12.5} and (d) PS _{35-b} -PEO _{10.5} films of different thicknesses under N ₂ , ethanol and water vapor.	108

Figure 5-13: (a) Typical two-color images showing individual NR molecules in a two-window set up for hPEO_{12.5}, PS_{35-*b*}-PEO_{10.5} and hPS_{16.4}. (b) Typical two-color images of PS_{35-*b*}-PEO_{10.5} (≈ 100 nm) thin film at different NR concentrations. Left: 580 ± 20 nm; right: 625 ± 20 nm. Image size $16 \times 16 \mu\text{m}^2$ 109

Figure 5-14: Histograms for the E_{SM} values of single NR molecules in thin PS_{35-*b*}-PEO_{10.5} films (*ca.* 100 nm thick) upon exposure to (A) N₂, (B) ethanol vapor and (C) water vapor. 110

Figure 5-15: (a) Spectra from a Ne lamp used for the wavelength calibration of the spectrometer. (b) Calibration curve for the spectrometer pixel position. 111

Figure 5-16: Fluorescence emission spectra of NR in ~ 100 -nm thick films of hPEO_{12.5}, hPS_{16.4} and PS_{35-*b*}-PEO_{10.5} under N₂ (black), ethanol vapor (red) and water vapor (blue). 111

Figure 6-1: Image of $1 \mu\text{m}$ fluorosphere obtained with the APD detector. Same image obtained from the recompilation of spectroscopic fluorescences. Software written by Dr. Higgins. 117

List of Tables

Table 2-1:	Common diffusion coefficient values for different solutes in water solution. ^{31,32} .	6
Table 2-2:	List of probe dyes with their common name, chemical formula, excitation and emission wavelengths and the highlight feature defining why they are commonly used.	9
Table 2-3:	List of formulas used to fit the FCS data depending on the type of diffusion expected in the material.	20
Table 4-1:	Fixed Parameters and Constants Used in the COMSOL Simulations.	62
Table 5-1:	Diffusion coefficients obtained from SMT data obtained in vapor-exposed thin films of hPEO _{12.5} , PS ₃₅ - <i>b</i> -PEO _{10.5} and PS _{13.5} - <i>b</i> -PEO ₄ . $D_{LabView}$ was obtained using the “software-based method”, and D_{Manual} was obtained by the “manual method”.	97
Table 5-2:	Diffusion coefficients obtained using FCS for the polymer films under different vapor conditions.	103
Table 5-3:	$E_{ensemble}$ values (95% confidence interval) from NR doped in 100-nm thick films of hPEO _{12.5} , PS ₃₅ - <i>b</i> -PEO _{10.5} and hPS _{16.4} under N ₂ (dry), ethanol vapor or water vapor.	106

Acknowledgements

I would like to thank my major professor and research advisor Dr. Takashi Ito for his efforts and constant guidance during my whole experience in this PhD at Kansas State University. All the time he dedicated to help me to develop my logic and critical thinking. All the time he spent to correct my drafts and presentations, taught me how to polish my skills and improve day by day.

Secondly, I would like to greatly thanks Dr. Daniel Higgins for introducing me into the microscopy research. He taught me how to use the microscopes and helped me with the analysis based on software he wrote for the research.

I want to deeply thank my current and former committee members, Dr. Christer Aakeroy, Dr. Urara Hasegawa and Dr. Mary Rezac, for their feedback received in every opportunity.

I want to thank Dr. Khanh-Hoa Tran-Ba for providing simulation results used in this thesis, as well as for spending together as group members for several months. His comments and guidance at the very early stages of my program were appreciated. I also thank Prof. Lane Baker and his student Ms. Natasha Siepser (Indiana Univ. Bloomington) for providing PET track-etched membranes with conical pores and their SEM images, and Dr. Lianjie Xue for valuable suggestions on the optical systems and methods of analysis.

I also acknowledge the current and former members of Dr. Ito's and Dr. Higgins' groups, especially Dol Raj Sapkota, Dr. Govinda Ghimire, Dr. Jay Sharma and Judith Bautista, for all the support and time we spent together. I am happy to have met all of you and to have spent time in such a multicultural and international environment.

I also want to extend my gratitude to all the faculty and staff members of the Chemistry Department at Kansas State University. Even before I started, they helped me and all the students with smile. From all the great team the university has, I want to be thankful to Jim Hodgson, Ron

Jackson and Tobe Eggers, because they were always life savers and their insight gave me always a chance to learn more.

I want to acknowledge the Fulbright institution for the chance offered and the scholarship provided to me. Thanks to them I started this journey that put me today where I am. I also acknowledge the US Department of Energy (DE-SC0002362) for financial support that made possible all the research and work I have done.

Finally, I want to thank deeply to all my family for understand the long nights and weekends I spent in this wonderful chapter of my life and the support they had with me. Also, I would like to thank all the friends I had the chance to meet here at Kansas.

Nothing of this would have been possible without all of them.

Dedication

This thesis is dedicated to my beloved wife Federica, my father Ramon, mother Sara, Eduardo Lozano, and Rodolfo who is not with us in presence but in essence. Finally, to Ulises who just came to the world.

Preface

Three monks were watching a flag flapping in the wind. One said to the other,

“The flag is moving.”

The other replied,

“The wind is moving.”

The third overheard this and said,

“Nor the flag, nor the wind; mind is moving.”

Zen Kōans

Acronyms and Definitions

AFM	Atomic force microscopy
APD	Avalanche photodiode
CCD	Charge coupled device
CV	Cyclic voltammetry
DBC	Diblock copolymer
DCLP	Dichroic long pass filter
DIC	N,N-Diisopropylcarbodiimide
DMF	N,N-Dimethyl formamide
DMSO	Dimethyl sulfoxide
FCS	Fluorescence correlation spectroscopy
hPEO	Homopolymer poly(ethylene oxide)
hPS	Homopolymer polystyrene
LASER	Light amplification by stimulated emission of radiation
MSD	Mean square displacement
NBD-X	Nitro-benzoxadiazole
NR	Nile Red
PET	Poly(ethylene terephthalate)
PS-b-PEO	Polystyrene-block-poly(ethylene oxide)
PSF	Point spread function
QE	Quantum efficiency
Rh6G	Rhodamine 6G

SE	Spectroscopic ellipsometry
SMT	Single molecule tracking
SNR	Signal to noise ratio
SOFI	Stochastic optical fluctuation imaging
SPT	Single particle tracking
SRB	Sulforhodamine B
STED	Stimulated emission depletion
TBTA	Tris[(1-benzil-1H-1,2,3-triazol-4-yl)methyl]amine
TICT	Twisted intramolecular charge transfer
TMRM	Tetramethylrhodamine, methyl ester

1. Introduction

Polymers are flexible mechanical materials that can be tailored for potential functionalization or manipulation, and thus are used for various applications.¹ This dissertation will discuss the longitudinally controlled modification of polymer-based pores and the assessment of the solvent-induced swelling of self-organized polymer nanostructures on the basis of the use and observation of small molecule diffusion. Polymers used in this dissertation, including poly(ethylene terephthalate) (PET) track-etched membranes and polystyrene–poly(ethylene oxide) diblock copolymers (PS-*b*-PEO), are potentially important in applications such as fuel cell polyelectrolytes,² filtration membranes,³ ion separation membranes⁴ and chemical sensors.⁵ For these applications, it is crucial to establish a means to functionalize polymers in a controlled manner and also to assess the physical and dynamic properties of polymer monoliths. The main focuses of this dissertation are to demonstrate the longitudinally controlled functionalization of PET track-etched pores and to clarify the swelling properties of PEO microdomains formed in thin PS-*b*-PEO films. These projects were taken advantage of the diffusion of small molecules such as electrochemically-generated catalysts and fluorescent probes in PET-track-etched pores and PEO microdomains, respectively. The pore functionalization and microdomain swelling were assessed using a series of fluorescence microscopic techniques.

This dissertation consists of six chapters. Chapter 1 briefly describes the motivation of the dissertation projects and provides the outline of this dissertation. Chapter 2 summarizes the nature of molecular diffusion, including the mathematical description of the process,^{6,7} diffusion coefficient, which describes the speed of molecular motions and also the properties of the media, and methods used to measure diffusion coefficient. Chapter 3 summarizes the properties of polymers used here, and also the principle and characteristics of instrumental methods used for

characterization of polymer monoliths in this dissertation studies. Chapter 4 describes the demonstration of the longitudinally controlled modification of PET track-etched pores using click reaction with electrochemically generated Cu(I) catalysts. This chapter shows simulation results for the prediction of pore modification behavior and experimental data obtained using fluorescence microscopy. Chapter 5 discusses the swelling properties of PS-*b*-PEO by ethanol and water vapor through comparison with those of PS and PEO homopolymers. The extent of the solvent-induced swelling was assessed by spectroscopic ellipsometry, and the swelling-induced changes in the polarity environment and permeability of each microdomain were measured using a series of advanced fluorescence techniques^{10,11} with two types of fluorescent probes having different characteristics.^{8,9} Chapter 6 provides the summary of the achievements in these two projects, and then possible future directions of these projects.

2. Diffusion

2.1 Small Molecule Diffusion

Diffusion can be defined as a macroscopic motion of a component due to a concentration difference. The diffusion process was first described by Adolf Fick ⁶ in 1855, as is known today as the Fick's first law of diffusion:

$$J = -D \frac{dC}{dx} \quad (\text{eq. 2.1})$$

This equation states that the flux J is proportional to the concentration gradient in the space dC/dx and the diffusion coefficient D . The negative sign is necessary because the driven force of the molecules is given by the motion from a high concentration area to a low concentration one, it is expected from the second law of thermodynamics

At a microscopic level, flux can be thought of as a sum of the motions of many single molecules. The simplest case would be a single molecule moving around. Known and poetically described since ancient Greece by Epicurus and later written by Lucretius in his "*De rerum natura*",¹² the motion of a single particle can be thought of as the motion of a single dust particle in an empty room. This motion was later studied by different researchers, specifically by Jan Ingen-Housz on his report about charcoal particles on the surface of alcohol,¹³ but it was credited to Robert Brown in 1872 from his microscopy observation of pollen particles.¹⁴ Diffusion can be calculated and measured for any particle, molecule or element moving in a solution. In this thesis the diffusion of gases will not be reviewed.^{15,16}

Einstein studied diffusion in the case of diluted solutions in his PhD thesis,¹⁷ where he derived an equation for a Stokes particle under Brownian motion in a quiescent fluid at uniform temperature (known today as the Stokes-Einstein equation). Einstein's result for the diffusion

coefficient (D) of a spherical particle of radius a with a very small Reynolds number in a fluid of dynamic viscosity η at absolute temperature T is:

$$D = \frac{RT}{NA} \frac{1}{6\pi\eta a} \quad (\text{eq. 2.2})$$

where R is the gas constant and NA is Avogadro's Number. This equation has been of utmost importance in history because it was used to make the first absolute measurement of NA , confirming the molecular theory. In addition, this equation shows a relation between the diffusion coefficient D and the viscosity of the medium.⁷ Other models were derived to calculate the D value for many systems, some of them are: Wilke and Chang;¹⁸ Scheibel;¹⁹ Reddy and Doraiswamy;²⁰ and others.²¹⁻²⁴ Each of these models have different assumptions and work in a certain range of solvent conditions, solute concentrations and temperatures.

Einstein²⁵ also described the motion in an isotropic medium and related this motion to the diffusion coefficient D as the mean square root of the diffusion distance following the equation:

$$D = \frac{1}{2n \tau} \langle \mathbf{R} \rangle^2 \quad (\text{eq. 2.3})$$

In this equation τ is the diffusion time, $\langle \rangle$ denotes an ensemble average and $\mathbf{R} = (r - r_0)$ is the net displacement vector, with r_0 the original position of a particle, r its position after the time τ , and n is defined by the dimension of the space (in the volume $n = 3$, in a plane $n = 2$). It is worth mentioning that $\langle \mathbf{R} \rangle^2$ is also known as Mean Square Displacement (MSD). The scalar diffusion coefficient (D) measures the molecule's mobility. In the isotropic case, it depends on the molecule type and the medium properties but not on the direction.

Another way to describe the motion of a particle in a media is by the mathematical "random walk" model.¹⁵ This mathematical model assumes that each step of the molecule has the same probability of occurring and no memory from the previous step. The random walk defines the

length of the particle steps (l) as fixed and it can only perform one step per unit of time t_{step} . To know the position (r) of the particle at any given time t_{length} , the probability of the particle being at different locations at time t_{length} needs to be known. The probability at each step is equal for the n directions possible, the binomial probability function applies for this case, as:

$$P(m, r) = \frac{m!}{r!(m-r)!} \left(\frac{1}{2}\right)^m \quad (\text{eq. 2.4})$$

Where m is the number of steps (in terms of time units m is equal to t_{step}/t_{length}) and r the position at time t_{length} . Then, the *MSD* of the particle can be calculated by adding up the square of the displacements and dividing by the total number of possibilities at each step (2^m). Because the probability is equal for each step in all directions, the total sum of the displacements must always be zero. However, the *MSD* can be expressed by the equation:

$$MSD = ml^2 = \frac{t}{\tau} l^2 \quad (\text{eq. 2.5})$$

Using eq. 2.3, the displacement of a particle exhibiting a Brownian motion, can be related as:

$$d = \sqrt{2nDt} = MSD \quad (\text{eq. 2.6})$$

where d is the distance “walked” from the initial position by the molecule or particle in a time t and n is the number of dimensions considered for the motion. This equation will be useful in Chapter 4 when the length of the inner wall of the PET track-etched membranes modification is correlated to the distance traveled for the copper complex, estimated by the time and the diffusion coefficient of the complex using eq. 2.3.

2.2 Diffusion Coefficient Measurement

2.2.1 Historical View

Before Fick obtained the mathematical relation between the flux and the concentration gradient (Fick's law⁶), diffusion was experimentally studied by Thomas Graham.²⁶⁻²⁸ Graham focused his experiments on the diffusion of gas and colloids in liquids.²⁹ Nevertheless, the diffusion coefficient was later measured for many molecules in a variety of solvents to have a better understanding of the materials and processes. In chromatography, the diffusion coefficient obtained from a set of conditions can be used to optimize the conditions of the system and understand the mass transport processes.³⁰ Table 2-1 shows common values for the diffusion coefficient of molecules in water.

Table 2-1: Common diffusion coefficient values for different solutes in water solution.^{31,32}

Solute	Solvent	Diffusion coefficient (m ² /sec)
Serum Albumin (FW:65000)	H ₂ O	0.12 x 10 ⁻⁹
H ⁺	H ₂ O	9.3 x 10 ⁻⁹
OH ⁻	H ₂ O	5.3 x 10 ⁻⁹
Na ⁺	H ₂ O	1.3 x 10 ⁻⁹
SRB	H ₂ O	4.70 x 10 ⁻¹⁰
Rh6G	H ₂ O	4.05 x 10 ⁻¹⁰

Historically, different methods were developed to obtain a diffusion coefficient of interest using Fick's law. The D value can be derived from the calculation of a change in the concentration in time or in position using an Arnold diffusion cell. Under the assumption of steady state and

unidirectional molecular pure diffusion, the concentration of the solute is measured at different lengths from the base, to calculate the diffusion coefficient using Fick's law (eq. 2.1).

Currently, the diffusion coefficient can be obtained by: measuring the viscosity,³³ by electrochemical methods,^{15,34,35} NMR methods,^{31,36,37} or fluorescence techniques.³⁸⁻⁴³ In Chapter 5 diffusion calculations are based on two fluorescence-based methods, fluorescence correlation spectroscopy (FCS) and single molecule tracking (SMT).

2.2.2 Fluorescence Based Methods

2.2.2.1 Fluorescence

Fluorescence is the emission of light by a molecule that has absorbed light. Shown in Figure 2-1, a Jablonski diagram shows the representation of a fluorescence process happening in the molecule.

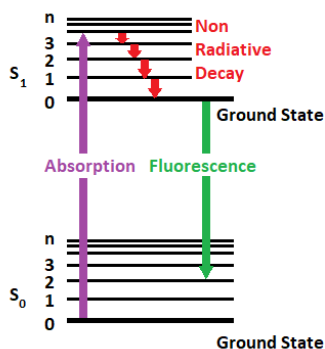


Figure 2-1: Jablonski diagram for fluorescence emission. This diagram only considers electronic and vibrational states. For simplification, rotational states, spins and phosphorescence decay through triplet states, are not shown.

In Figure 2-1, the purple arrow represents an absorbed photon, which moves a molecule to a more energetic electronic and vibrational states. The small red arrows represent non-radiative relaxation from excited vibrational states to the electronic excited ground level. This process is the

result of vibrational relaxations associated with the solvent. Finally, the green arrow is a radiative decay that produces fluorescent light emission. This process is unique because the fluorescence emission is always at a longer wavelength than the excitation, leading to what is known as the Stokes shift of the emission.

The Stokes shift allows emission to be collected and residual light from the excitation source to be removed by filtering. In addition, since the emission happens in all directions, light is commonly collected at 90 degrees (or 180 degrees in microscopy) from the excitation light path. Both features help reduce background signal and therefore achieve a lower detection limit.

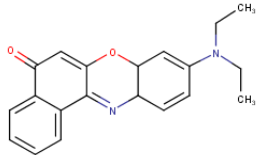
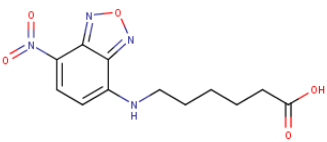
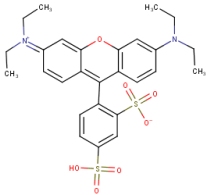
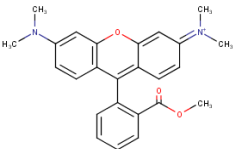
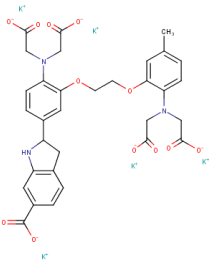
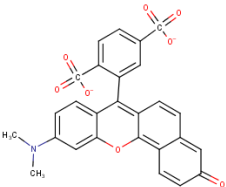
The intensity of the fluorescence emission is defined by the power of the excitation light (P_p), and the capacity of the molecule to emit. This capacity is defined as quantum yield (ϕ_f). Therefore, the higher the power of light and the larger the quantum yield, the more the photons emitted by the fluorescent molecule will be.

Fluorescence methods are commonly based on the fluorescence of a molecule used as a probe. Therefore, the chemistry and properties of a fluorescent probe dye are another factor that makes fluorescent methods highly desired to obtain and measure the diffusion coefficient. If we are observing the diffusion behavior of a fluorescent probe, the diffusion coefficient obtained will be coming from the fluorescent probe in that particular environment. Therefore, it is important to have in mind that the interactions of the probe with a medium (solvent or structure) in which the molecule is moving will dominate the diffusion behavior. For this reason, the selection of a probe is as important as the employed method.

In addition, different dyes have unique properties that the user can take advantage of, like solubility, size and charge, among others. This makes it possible to selectively locate the probe into the domains, or the sample regions that the user wants to study.

Some probe dyes emit fluorescence at different wavelengths depending on the chemical environment they are in. A list of well-known fluorescent dyes is shown to exemplify this point in Table 2-2. In this thesis, the solvatochromic effect is used in Chapter 5.

Table 2-2: List of probe dyes with their common name, chemical formula, excitation and emission wavelengths and the highlight feature defining why they are commonly used.

Name	Chemical formula	$\lambda_{Ex}/\lambda_{Em}$ (nm)	Highlight	Reference
Nile Red (NR)		552/636 (in methanol)	Solvatochromic	44-47
Nitro-benzoxadiazole (NBD-X)		490/550	Solvatochromic	48,49
sulforhodamine B (SRB)		532/560	Preferentially partitioned to PEO	43,50,51
TMRM		532/560	Potential probe	32
Indo-1		338/400	[Ca ²⁺] Probe	32,52
C.SNARF-1		480-530/580-640	pH Probe	32,53

2.2.2.1.1 Solvatochromism

Solvatochromism is the phenomenon in which the fluorescence from a probe shifts to shorter or longer wavelengths depending on local polarity around the probe.⁵⁴ In Figure 2-2.a, a series of fluorescence emission spectra of Nile Red (NR) are shown. A red shifting of the spectra was observed as the solvent became more polar. The most accepted explanation refers the red shifting to the stabilization of the twisted intramolecular charge transfer (TICT) state in a polar solvent. While generally accepted the actual mechanism it is not fully understood.^{44,55}

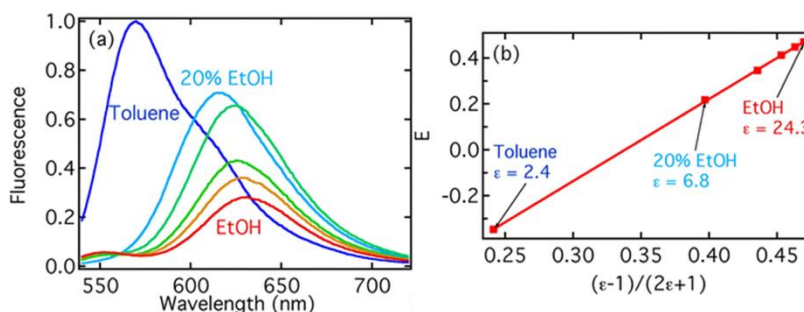


Figure 2-2: (a) Fluorescence emission spectra for a series of Nile Red solutions. The toluene solution is shown in blue, showing maxima emission (λ_{em}) peak of ≈ 580 nm, and in red the ethanolic solution of Nile Red is showing the red shift with a $\lambda_{em} \approx 625$ nm. (b) Plot of the E value (emission ratio) against the Clausius-Mossotti factor for the series of Nile Red solutions with mixed solvents (different ratios of ethanol:toluene). Reproduced with permission from Ref. ⁴⁵. Copyright 2014 American Chemical Society.

One way to take advantage of the solvatochromic effect in a fluorescence experiment is by correlating the intensity at the emission wavelength with the polarity of a solution or the environment surrounding the dye probe. The emission ratio (E) is defined as:

$$E = \frac{I_{polar} - I_{non\ polar}}{I_{polar} + I_{non\ polar}} \quad (\text{eq. 2.7})$$

The “polar” intensity refers to the intensity at the characteristic wavelength from the particular dye of interest in a solvent considered to be polar. Likewise, the “non polar” intensity is the intensity

at the characteristic wavelength from the dye in a “non-polar solvent”. The “polar” or “non polar” designations are arbitrary subscript notations. As an example, Figure 2-2 shows the fluorescence emission spectra of Nile Red (NR) in different ratios of toluene–ethanol mixtures. For the “polar” case the solution was prepared from pure ethanol and for the “non polar” case the solution was made from pure toluene.

The solvatochromic effect can be modeled using the Lippert-Mataga equation^{56–58} which considers the reorientation of the dipole moment of the molecule and the electron redistribution inside the molecule following a change in electronic state. However, assuming that there is no electron redistribution other than the redistribution to produce the change in the dipole moment, a more simplistic view where only the dipole moment of the molecule changes depending on the solvent, is described by the Clasiouss-Mossotti equation.

$$CM = \frac{(\epsilon-1)}{(2\epsilon+1)} \quad (\text{eq 1.8})$$

This simplified version of the Lippert-Mataga equation only considers the dye molecules as perfect spheres in a continuous medium (the solvent). The spectral shifting is related to the reorientation of the dipoles upon the effect of the solvent molecules. Consequently, the reorientation can be expressed from the change in the dielectric constant epsilon (ϵ) at a given solvent condition.

Empirically, the E value is proportional to the CM for a two-solvent mixture.^{46,59} As an example, the case of Nile Red is shown in Figure 2-2b for the ratios of ethanol : toluene series.

In Table 2-2, two examples of common solvatochromic fluorescent probe dyes are shown with their molecular structures. The use of these types of probes dyes can reveal information about the heterogeneity of polarity environments in a thin film, and thus can be used to map those heterogeneities and to reveal information about solvent penetration on the basis of the shift of the

emission.^{45-48,60} In Chapter 5 the solvatochromic dye NR revealed its location based on its E value in diblock copolymer thin films.

2.2.2.2 Fluorescence Microscopy

Microscopic methods and techniques have shown large improvements over the last decade.⁶¹ From the first microscopy developed and used by Antonie Van Leeuwenhoek in the 1600s up to the current days the improvements are astonishing.⁶² There is no doubt about the incredible upgrade the microscopic technique has experienced since 1600.

The introduction of the super-resolved fluorescence microscopy^{64,65} was a great improvement in optical microscopic techniques, as was awarded the Nobel Prize in 2014. Super-resolution microscopy is referred as the microscopy where the optical diffraction-limited resolution, determined by Abbe's law, is surpassed. The diffraction limit was calculated by E. Abbe⁶⁶ in 1873 and established that the maximum resolution that is attainable by pure optics methods is as follows:

$$R_{xy} = \frac{\lambda}{2 n \sin(\theta)} \quad (\text{eq. 2.9})$$

where R_{xy} is the resolvable feature size, λ is the wavelength of the light, n is the refractive index of the medium being imaged in, and θ is the half-angle subtended by the optical objective lens. The denominator is usually referred to as the numerical aperture (NA) defined by the refractive index (n) of the medium and the aperture angle θ (when the angle is small) in eq. 2.10.

$$R_{xy} = \frac{\lambda}{2 NA} \quad (\text{eq. 2.10})$$

This equation explains that the capability to differentiate two different spots in the microscope is defined by the wavelength of the emission light and the optical set up capability to collect light.⁶⁷

However, improved spatial resolution was pushed by different researchers over the last decades using different strategies such as: stochastic optical fluctuation imaging (SOFI) or stimulated emission depletion (STED).⁶⁸⁻⁷⁴ From all the available microscopic methods, single molecule/particle tracking (SMT, SPT) techniques are unique because they give spatio-temporal information about the dynamic behavior of an individual molecule/particle instead of ensemble-averaged information (such as the diffusion coefficient) obtained from the methods explained above in section 2.2.1.

Figure 2-3 shows the scheme of the confocal and widefield microscopy setup depicting excitation and emission beam paths. The scheme shows how the excitation light from the source can be trimmed by the filters and dichroic mirrors and the emitted light from the fluorescent probe can be collected.

In addition, Figure 2-3b and d show the schematics of the rays for the illumination of the sample. The difference in sample illumination is correlated to the name of each microscopic technique. As the name suggests, wide field microscopy illuminates a wider area of the sample, while single-point illumination narrows the illumination to a focused area.

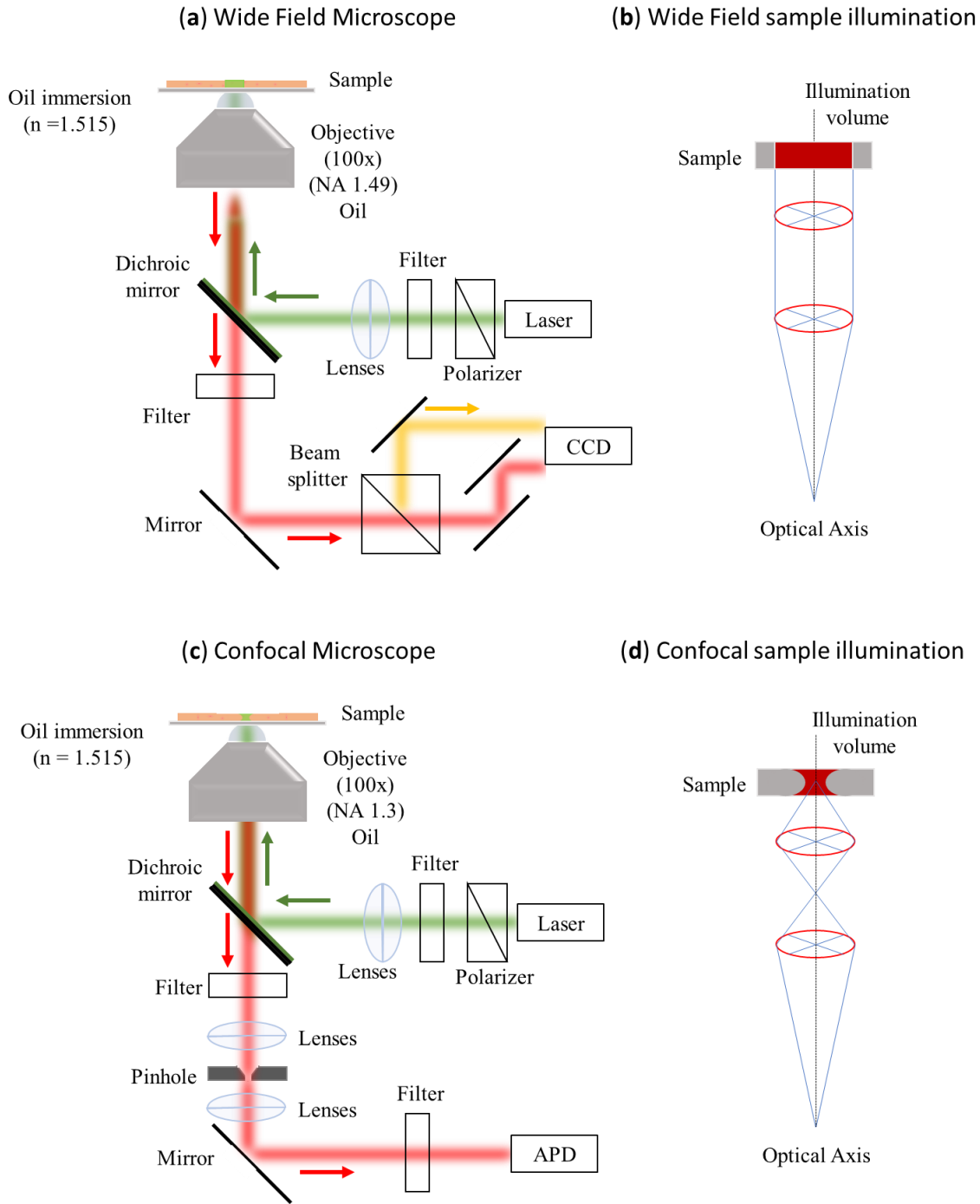


Figure 2-3: (a) Wide-field microscopy setup with a laser beam (in green) as excitation light; a beam splitter, and a CCD camera as a detector; (b) Wide-field sample illumination; (c) Confocal microscopy setup with a laser beam (in green) as excitation light; a pinhole (for 3D imaging) and an avalanche photo diode (APD) as a detector; (d) Single-point sample illumination.

The signal (S_S) from a single in a microscope can be expressed as⁷⁵:

$$S_S = 0.855 CF\phi_f P_p \sigma \tau \left(\frac{NA}{\lambda}\right)^2 \quad (\text{eq. 2.11})$$

Where the C and F are the detection and collection efficiency respectively. The 0.855 value is an estimation for a microscopy setup using several optical lenses to collect the fluorescence. The fluorescence of a probe molecule can be used to study the diffusion of the molecule in a particular environment or solution. That information can be later used to infer or conclude the properties of the medium. In this thesis, the fluorescence of molecules chemically bonded to the inner surface of a PET track-etched membrane was measured to verify the controlled modification of the pores via electrochemically assisted click reaction in Chapter 4. Single molecule tracking and fluorescence correlation spectroscopy were used to verify the unique swelling properties of the PEO microdomains in thin PS-*b*-PEO films by ethanol vapor or water vapor in Chapter 5.

2.2.2.3 Fluorescence Correlation Spectroscopy (FCS)

Fluorescence correlation spectroscopy (FCS) was developed in 1972 by Madge et. al.^{76,77} as a technique to measure the diffusion and binding of ethidium bromide onto a double stranded DNA. This technique uses statistical analysis of the fluorescence fluctuations in a confocal volume given by the laser illumination, to decipher the diffusion of fluorescent molecules (and/or other dynamic molecular events⁷⁸). This technique was mostly used in biophysics⁷⁹ but blossomed over the last decade to include its use in material science.³⁸

FCS measures fluorescence intensity against time from a microscopic volume created by a focused laser beam (Figure 2-3d). The fluctuation of fluorescence signal is the result of a molecule (or a few) passing through the confocal volume. Assuming Brownian motion of the molecules, the fluctuations observed in time can be related to the diffusion of the molecules in the system. From

this correlation, the autocorrelation function ($G(\tau)$) is obtained. This function relates the time (τ) between the events (fluorescent fluctuations). Once the autocorrelation function is obtained, it is fitted using a model that reflects the conditions of the motions of fluorescent molecules. From this fitting, the diffusion coefficient can be obtained.

The mathematical formalism, the instrumentation and the data analysis for the FCS experiment is explained in detail below.

2.2.2.3.1 FCS General Formalism

In this dissertation the mathematical derivation used for FCS is based on the one presented by O. Krichevsky and G. Bonnet.¹⁰

An ideal solution of m molecules/particles where each j components is characterized by its concentration $C_j(\mathbf{r}, t)$ at time t and position \mathbf{r} . The ensemble average concentration $\langle C_j(\mathbf{r}, t) \rangle$ has a local deviation as $\delta C_j(\mathbf{r}, t) = C_j(\mathbf{r}, t) - \langle C_j(\mathbf{r}, t) \rangle$.

Near the equilibrium the components can participate in the diffusion events or in chemical reactions. Therefore, the j components can be converted into others, and the change in time of the local deviation (δC_j) can be written as:

$$\frac{\partial \delta C_j(\mathbf{r}, t)}{\partial t} = D_j \nabla^2 \delta C_j(\mathbf{r}, t) + \sum_{k=1}^m K_{jk} C_k(\mathbf{r}, t) \quad (\text{eq 2.12})$$

The first term of this equation accounts for the diffusion while the second term describes the chemical reaction where K_{jk} is the equilibrium constants (for j chemical components).

FCS measures fluorescence fluctuation from molecules traveling through the confocal volume. The number of photons emitted and collected from each of the molecules is proportional to intensity $I(\mathbf{r})$. The intensity is determined by the illumination light and the detection optical

path. Thus, the number of photons emitted and collected from each molecule per sample time Δt , can be expressed as:

$$n(t) = \Delta t \int d^3 r I(r) \sum_{k=1}^m Q_k C_k(r, t) \quad (\text{eq 2.13})$$

In this expression Q_k is the product of the absorption cross-section and by the fluorescence quantum yield and the efficiency of fluorescence for the component k .

The measured fluorescent signal is associated with the shot noise which is not correlated and therefore should not contribute later to the autocorrelation function $G(t)$. The expression, for the deviation of the photon count ($n(t)$) from the mean ($\overline{n(t)}$) as the result of the shot noise is described as:

$$\delta n(t) = n(t) - \overline{n(t)} = \Delta t \int d^3 r I(r) \sum_{k=1}^m Q_k C_k(r, t) \quad (\text{eq 2.14})$$

The autocorrelation function $G(t)$ is defined for FCS experiments, as the time average of the products of the intensity fluctuations and normalized by the square of the average intensity ($\overline{n(t)}^2$):

$$G(t) = \frac{1}{\overline{n(t)}^2 T} \sum_{i=0}^{T-1} \delta n(t') \delta n(t' + t) \quad (\text{eq 2.15})$$

In this expression T is the total number of accumulated sampling intervals. With this definition, the total duration of the experiments is $T\Delta t$ (Δt is the time required for the measurement, defined by the detector used).

FCS assumes that in the system all the events are equally representative of the whole in terms of time and space, this is called ergodicity. Under the ergodicity condition the autocorrelation function can be described for the system as an ensemble average by the following equation.

$$G(t) = \frac{\langle \delta n(0) \delta n(t) \rangle}{\bar{n}(t)^2} \quad (\text{eq 2.16})$$

Using eq. 2.16 and combining it with eq. 2.13, the autocorrelation function of the intensity fluctuations is a convolution of the auto- and cross-correlation functions of the concentration fluctuation with the excitation profile, defined as:

$$G(t) = \frac{(\Delta t)^2}{\bar{n}(t)^2} \iint d^3r d^3r' I(r) I(r') \sum_{j,l} Q_j Q_l \langle \delta C_j(r,0) C_l(r',t) \rangle \quad (\text{eq 2.17})$$

To simplify, we assume an ideal solution where the distance between molecules is larger than the area of observation, and where there is no correlation between molecules of different species (defined at the beginning as j). With these assumptions the ensemble of the local deviation at time zero is:

$$\langle \delta C_j(r,0) \delta C_k(r'',0) \rangle = \bar{C}_j \delta_{jk} \delta(r - r'') \quad (\text{eq. 2.18})$$

In this expression, \bar{C}_j is the mean-square fluctuations of the number of molecules in a volume unit.

This fluctuation is happening as a variable of time and therefore it is possible to use the Poisson probability distribution to analyze the fluctuation of molecules in a volume unit in time. For this specific case, the Poisson statistic model gives the probability of a molecule going through the confocal volume and emit in a given time. Then the fluctuation in the fluorescent signal is related to the event and the frequency of the fluctuation with the Poisson statistic.

Subsequently, the Fourier transform is applied to the autocorrelation function $G(t)$ (eq. 2.17) to obtain the solution of the fluctuation in time and space. The detailed mathematical procedure is carefully and fully explained by O. Krichevsky and G. Bonnet.¹⁰

After some laborious mathematical work, $G(t)$ can be rewritten in terms of the experimental set up, the diffusion coefficient, chemical reaction rates and concentration of the chemical components. The general expression is as follows:

$$G(t) = \frac{(2\pi)^{-3}}{Q^2 c^2} \int d^3q \exp\left(-\frac{w_{xy}^2}{4}(q_x^2 + q_y^2) - \frac{w_z^2}{4}q_z^2\right) \times \sum_{j,l} Q_j Q_l \bar{C}_j \sum_s X_l^{(s)} \exp(\lambda^{(s)} t) (X^{-1})_j^{(s)}$$

(eq. 2.19)

This general expression utilized and assumes a Gaussian illumination/detection optical setup. From that assumption w_{xy} and w_z arise, representing the laser beam area in the horizontal plane and in the vertical plane, respectively, and thus define the volume of observation or the confocal volume. Since the displacement of the molecule is observed in this volume and under the assumption of Brownian motion, the diffusion coefficient then can be obtained as a function of time for which the particle j spent in the area can be expressed as:⁷⁹

$$D = \frac{w_{xy}^2}{4\tau_D}$$

(eq. 2.20)

Experimentally all the parameters are known but τ_D . This τ_D is the characteristic time at which the molecule spends in the confocal volume, and it is the result from the fitting of equation 2.19. The fitting used to obtain this value must reflect the characteristic conditions. As an example, we can consider a 3D model where the molecules enter and exit the volume of observation from any direction. A 2D model considers only the xy plane, and if there are different distinct diffusion modes, the model might require considering more components to the equation.

Table 2-3 shows the experimental correlation function and the formula for anisotropic 3D diffusion, two components based on 1D and 3D diffusion, anisotropic 2D diffusion, and two 2D components.

Table 2-3: List of formulas used to fit the FCS data depending on the type of diffusion expected in the material.

Diffusion type	Formula	Reference
Experimental Autocorrelation function	$G(t) = \frac{\langle I(t)I(t+\tau) \rangle}{\langle I(t) \rangle^2} - 1$	77,80
Anisotropic 3D	$G(t) = \frac{A}{(1 + \tau \frac{D_x}{w_{xy}^2})^{1/2} (1 + \tau \frac{D_y}{w_{xy}^2})^{1/2} (1 + \tau \frac{D_z}{w_{xy}^2})^{1/2}}$	77,80
1D and 3D 2 components	$G(t) = \frac{A}{(1 + \tau \frac{D_1}{w_{xy}^2})^{1/2}} + \frac{B}{(1 + \tau \frac{D_2}{w_{xy}^2})^{1/2} (1 + \tau \frac{D_2}{w_z^2})^{1/2}}$	81
Anisotropic 2D	$G(t) = \frac{A}{1 + \tau \frac{D}{w_{xy}^2}}$	78,82
2D 2 components	$G(t) = \frac{A}{1 + \tau \frac{D_1}{w_{xy}^2}} + \frac{B}{1 + \tau \frac{D_2}{w_{xy}^2}}$	83,84

From Table 2-3, the two 2D components model was used for analyzing FCS data associated with the diffusion of SRB in the PEO microdomain of thin PS-*b*-PEO films in Chapter 5.

2.2.2.3.2 Instrumentation of FCS Measurements

A typical setup for confocal microscopy is shown in Figure 2-3c. This type of microscope consists of a light source, usually a laser, for the excitation of a dye of interest, suitable optics including optical filters, a dichroic mirror or polarizers, a high magnification objective lens, a pinhole and a light detector.

Because the technique measures changes in fluorescence intensity over time, the detector used is a key component to obtain reliable data. The detector must have high quantum efficiency

(QE). The common choice of a high QE detector is an avalanche photo diode (APD) which can measure a few photons with temporal resolution of nanoseconds. Another common characteristic of a confocal microscope is the use of a pinhole before the APD to define the volume of detection. The pinhole reduces the light coming from regions out of focus.⁸⁵ This is highly recommended for a film thicker than the vertical optical resolution or for a solution sample. Other researchers used an optical fiber to define the volume of detection.⁸⁶⁻⁸⁸ Chapter 5 discusses the diffusion coefficient inside the PEO microdomains of PS-*b*-PEO films, for which the pinhole was not used because of the ultrathin thickness of the films. Some previous studies of molecular diffusion in thin films also avoided using the pinhole due to the loss of signal.⁴¹

There are two common ways to identify and calibrate the confocal volume (w_{xy}). Researchers can either (i) use a solution of a dye with a known D value or (ii) measure a sub-resolution particle (either a single molecule or a fluorosphere). In this thesis the second method was used, since the setup used for the measurements was prepared for ultrathin films. For that reason, the calibration was done using single molecule imaging following previous works⁴¹ and is explained in detail in Chapter 5.

During the FCS experiments, the laser was directed through the appropriate optics before focused into the sample through an objective lens ($NA \approx 1.4$). Then, the emitted fluorescence from the confocal volume was collected by the same objective lens and was transmitted through the dichroic mirror before finally being detected with a single point detector (Avalanche Photo Diode was generally used).

2.2.2.3.3 *FCS Data Analysis*

Using the experimental setup, the fluorescence signal from the molecules when passing through the confocal volume is collected as a function of time. Typical FCS data is shown in Figure

2-4a, where the large spikes correspond to the fluorescence of the probe dye(s) moving through the confocal volume (scheme shown in Figure 2-5). The data is converted to obtain an autocorrelation function $G(\tau)$, which is fitted to an appropriate function, already talked about and gave in Table 2-3.

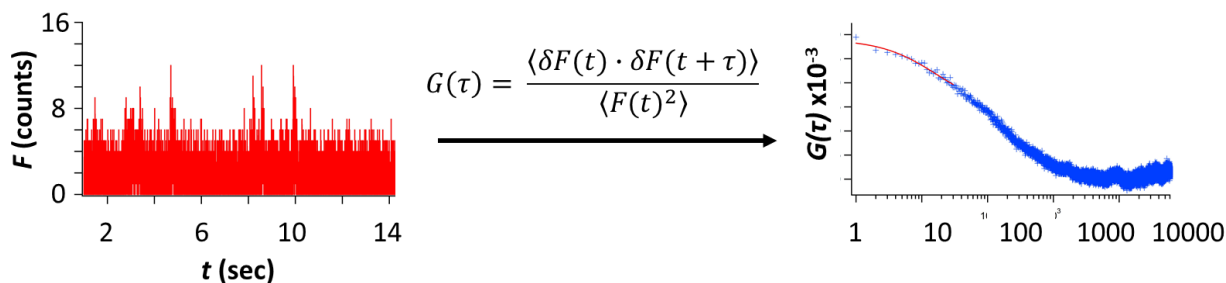


Figure 2-4: (a) Representative data from an FCS experiment. Fluorescence signal (F) is in counts per unit time (1 msec) measured with an APD detector, against time (t). (b) An autocorrelation function obtained from the data. The blue dots are values calculated for the autocorrelation function and the red line is the fitting function (in this case anisotropic 3D).

Correlation of the data is the mathematical method to find a ‘correlation parameter’. What the correlation is meant for is to find the time (τ_D in our notation) at over which the event occurs.

To manually find the correlation parameter, the process requires a series of steps. First the fluorescence signal against time is plotted. Then the signal is shifted by a lag time. If there is a correlation in the fluorescence signal, at a given time one fluorescence signal event will overlap another. The time distance between events Δt that arises from that time over which the signal remains self-similar, is the time used in eq. 2.20 to obtain the diffusion coefficient. The manual method is hard to achieve and is very time-consuming (the longer the measurement duration, the longer the process). Another way, similar in concept, is the autocovariance, defined as:

$$\rho(j) = \frac{\frac{1}{N-j} \sum_{i=j}^N (I_i - \bar{I})(I_{i+j} - \bar{I})}{\frac{1}{N} \sum_j (I_i - \bar{I})^2} \quad (\text{eq. 2.21})$$

Where the I_n are the intensity values at a given time. The underscores i and j correspond to the shifting in time. This is the empirical function that is used as autocorrelation function $G(t)$ as it was presented in the previous section.

Figure 2-4 shows the schematics of the process from the raw data collected by the APD to an autocorrelation function, followed by fitting the $G(\tau)$ with the correct model depending on the system of analysis for obtaining the τ_D . Lastly to obtain the D value from eq. 2.20, the w_{xy} needs to be measured.

To obtain the w_{xy} , the confocal volume must be determined. As mentioned before, there are two common methods: (i) Use a solution of a dye with a known D using the same setup; or (ii) measure the size of a sub-diffraction particle or molecule. The first strategy calculates the diffusion coefficient of a probe using the fitting function given in Table 2-3. From the fitting, and using eq. 2.20, the w_{xyz} for the system defined by laser illumination and lens capability to collect light is determined. The second method measures the laser area from a single molecule as a probe. In this thesis the second method was used to obtain the w_{xy} for the D calculations. Figure 2-5 shows how the single molecule scans the laser showing the actual size of the illuminated area.

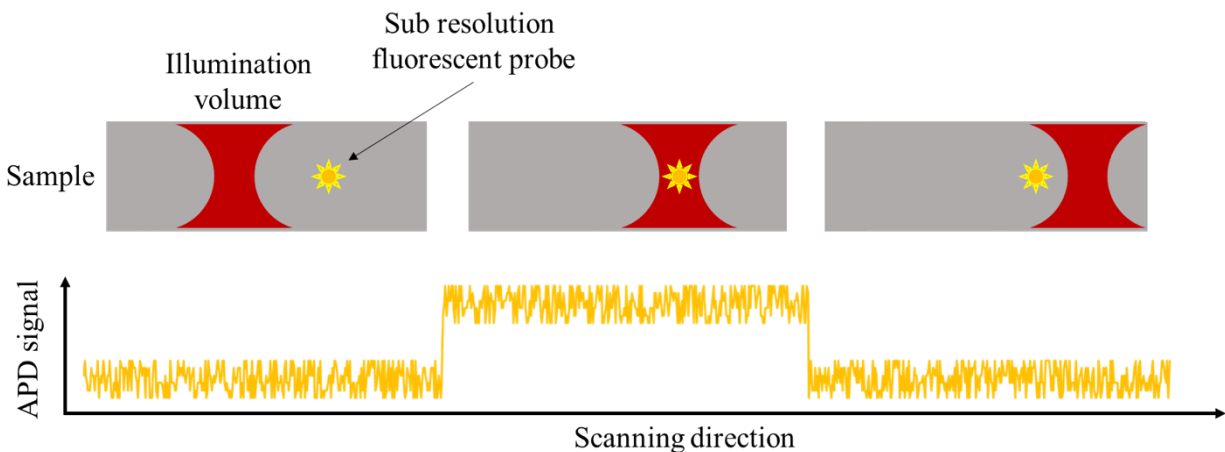


Figure 2-5: Scheme of the laser illumination exploration from a single fluorescent probe.

Once the calibration of the confocal area is obtained, using an adequate equation from Table 2-3 with the empirical w_{xy} (eq. 2.20), the diffusion coefficient can be calculated.

2.2.2.4 Single Molecule Tracking (SMT)

Many conventional methods, including FCS, give a D value as the result of measuring an averaged behavior from an extensive area, time or multiple events. This ensemble-averaged information gives the diffusion behavior of the majority of the molecules but does not reflect unique behaviors that may be interesting.^{89,90} To measure the spatiotemporal behavior of a single molecule, a method needs be able to identify with certain precision a single emission spot from a single molecule, and to create a trajectory following that spot in time (through video frames) and space. The trajectory finally gives the diffusion coefficient of the molecule. To do so, single molecule tracking (SMT) is used. SMT is based on wide-field fluorescence microscopy and relies on three steps: *(i)* spot identification, *(ii)* spot Gaussian fitting, and *(iii)* linking the individual spots into trajectories.

The first step is to identify a fluorescence spot from a single molecule. It is crucial to minimize background signals for observing single molecule fluorescence. The experimental setup based on wide-field fluorescence microscopy as shown in Figure 2-3a can give background low enough for single molecule fluorescence detection because fluorescent light is collected at 180 degrees from the excitation light direction. In addition to this, the red shift of the fluorescence from the excitation light allows for filters to be employed to remove the reflected excitation light and collect light from the fluorescent probe with a low background.

If dye concentration is sufficiently low, a single molecule can be observed as a spot shining in the dark. As Dr. Higgins mentioned in class: “stars are always in the sky, but only at night the background is low enough to see them”.

To be able to measure the diffusion of a single molecule, the molecule needs to be followed in time and space. As shown in eq. 2.6, D can be determined from diffusion distance represented by MSD. The value obtained as D relies in the precision of the spatial resolution measurement. This was a limitation since Abbe’s law in eq. 2.10 limits the spatial resolution of molecular position to a value close to half the emission wavelength. In other words, a molecule with a size of 2 Å that emits at 500 nm wavelength, would be seen as a 250 nm spot, a thousand times larger. This is transduced in a large error in the D measurement. The strategy to determine the position of a single molecule is the fitting of the fluorescence profile from a spot. Figure 2-6 illustrates how the fitting enhances the localization precision for determining the position of a single molecule.⁹¹

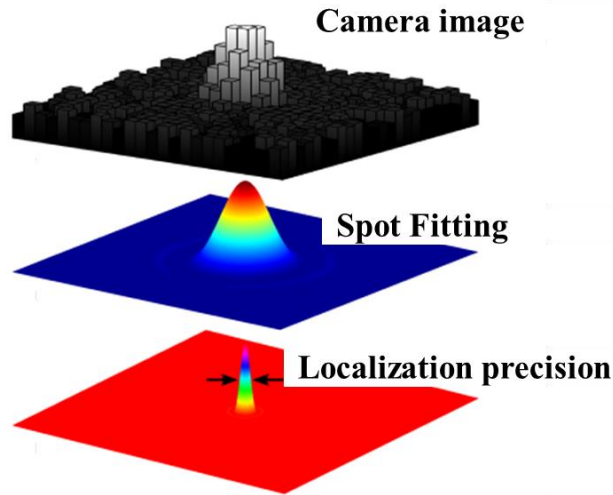


Figure 2-6: Schematic of the single molecule localization enhancement. Reproduced with permission from Ref 91. Copyright 2014 Taylor & Francis.

The fitting of the spot is done using a Gaussian model that accounts for the intensity and distribution of the pixels used to form the image. This method is well known since 1920 when W. Heisenberg demonstrated the localization of a single nanoscale object with nanometer precision.^{91,94} This will be determined by the background noise, which can be identified depending on (i) dark counts/read out noise (from the detector) and (ii) inelastic scattering from the sample (sample background). Signals from each source can be expressed by:

1. Dark counts, S_d :
$$S_d = k_d \tau$$
2. Sample background, S_b :
$$S_b = F d P_p \tau \alpha_b$$

In these expressions, k_d is the dark count rate, F is the collection efficiency, d is the depth of focus, P_p is the laser power and α_b is the scattering efficiency. The total signal from the fluorescence spot (S_τ) is described by eq. 2.11, which includes the signal from the dark counts as well as the signal from scattering by the sample:

$$S_t = 0.855 CF\phi_f P_p \sigma \tau \left(\frac{NA}{\lambda}\right)^2 + k_d \tau + FdP_p \tau \alpha_b \quad (\text{eq. 2.22})$$

The first term in this equation is the signal from a single emitter/molecule taking into account the microscope light collection capability (C), the light detection capability (F); the quantum yield of the fluorescent molecule (ϕ_f); the incident optical power in photons per second (P_p); the illumination area (σ); the signal averaging time (τ); and the wavelength (λ). Thus, the attainable signal to noise ratio (SNR) expression ends up being expressed as¹¹:

$$SNR = \frac{0.855 CF\phi_f P_p \sigma \tau \left(\frac{NA}{\lambda}\right)^2}{\sqrt{0.855 CF\phi_f P_p \sigma \tau \left(\frac{NA}{\lambda}\right)^2 + k_d \tau + FdP_p \tau \alpha_b}} \quad (\text{eq 2.23})$$

With this expression, the number of photons needs to be maximized as well as reducing the background. Experimentally, to reduce the sources of noise, materials should be transparent (in the wavelength range used) and homogeneous (to avoid scattering) if possible. Another reason to try to maximize the photon counts is given by statistics. The error associated with the measurement is inversely proportional to the square root of the photon count N (as a function of the numbers of photons recorded by the camera). For a large number of photons (≈ 200 photons) the localization of a single emitter in absence of background and dark counts is given by the localization precision:⁹¹

$$\delta x = \frac{0.44\lambda}{\sqrt{N} \times NA} \quad (\text{eq. 2.24})$$

As an example, for a single molecule producing 300 photons per frame, with a NA equal to 1.35 and an emission wavelength of 500 nm, the localization precision is around 10 nm. In other words, the position of the molecule can be narrowed down to 5 nm theoretically (half of the localization radius). Factors that can decrease the localization precision are the pixilation and the

background counts. Taking this into account, a most realistic form for the localization precision can be expressed as:⁹⁵

$$\delta x = \sqrt{\frac{0.1936\lambda^2}{N \times NA^2} + \frac{a^2}{12N} + \frac{0.942\lambda^4 B}{a^2 N^2 NA^4}} \quad (\text{eq. 2.25})$$

where a is the pixel size and B is the background counts. With this new expression and using the same values for NA and emission wavelength as used before, but now considering a pixel size of 100 nm and 100 photons coming from the background, the localization precision becomes around 15 nm. These calculations show the importance of sample preparation and choosing the right materials for the experiments. If possible, a probe dye with a high quantum yield, clean optical systems, lens with large NA and transparent materials and substrates are vital to obtain a good measurement.

SMT is an incredibly powerful tool to obtain the visual evidence of the dynamics of individual fluorescent probes in different materials. SMT was previously used to characterize the nanostructure of polymers^{43,96-98} as well as other materials^{30,99} where the fluorescent probe revealed the structure by moving inside and then the image was treated to obtain a super-resolution map of the domain structure.

2.2.2.4.1 *Instrumentation of SMT*

For wide-field fluorescence microscopy, a laser with an adequate wavelength selected for the fluorescent probe of interest is commonly used as a light source, as with confocal fluorescence microscopy. Figure 2-3a shows the setup of a wide-field fluorescent microscope. In this scheme, the laser light is sent through optics and filters and focused into the objective lens. The light then illuminates the whole area of observation. Figure 2-3b shows the diagram for the illumination.

Fluorescence emitted is collected by the same objective lens and delivered through the dichroic mirror which allows only light of longer wavelength than the excitation wavelength to pass. Afterwards, the emitted light travels across a series of optics until it reaches the detector. In the scheme in Figure 2-3a, an optosplit is set before the detector. The optosplit incorporates a dichroic mirror and a bandpass filter. This configuration affords two channels showing fluorescence images in two different wavelength ranges. This feature is often used for a fluorescent probe that changes its emission wavelength depending on some variable such as environmental polarity, potential or pH. For NR, the fluorescence intensities in the two channels can be correlated to environmental polarity in the nanoscale region surrounding each NR molecules.^{45,100}

2.2.2.4.2 *Diffusion Coefficient Calculations from Trajectories*

As mentioned above, using eq. 2.5, the diffusion coefficient of a single molecule moving by Brownian motion can be derived from the MSD. Therefore, once the fluorescent spot is identified in each frame and the position is determined with the localization precision according to the experimental setup, the creation of a trajectory follows. To do so, it is necessary to connect the same spot in each frame along a video. The scheme of the process is shown in Figure 2-7. Many published methods achieve the position determination followed by spot linking.^{101–103}

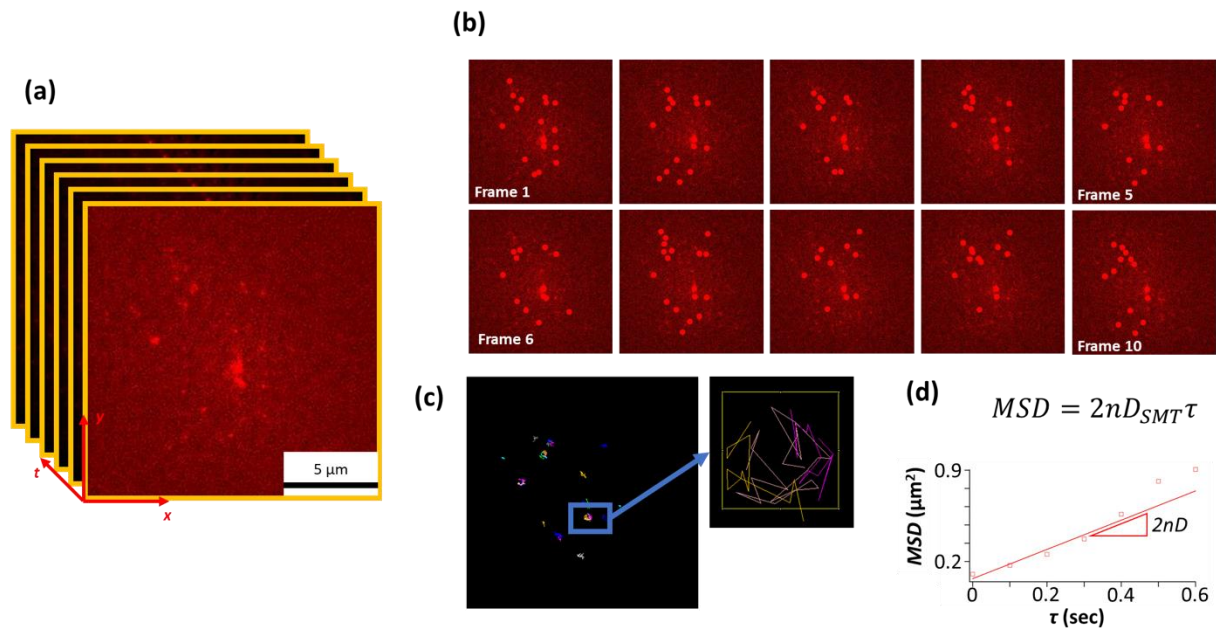


Figure 2-7: SMT process, from spot identification to spot linking across consecutive frames in a video. (a) shows how a video can be thought of as a consecutive series of frames in an time axis(τ); (b) is the identification of the single fluorescent molecules spot in each consecutive frames; (c) shows linking of the spots by “the closest one” method to create trajectories; (d) shows a plot of MSD against time (τ) to obtain the diffusion coefficient from the slope of the plot.

These methods do not rely upon the assumption of specific molecular motions, which helps determine trajectories for systems that involve the fluctuation of movement speed. However, there is no specific labeling on each of the molecules. As a result, every spot linking is done under the assumption that (i) a molecule moves a distance shorter than the observation area between frames; and that (ii) the position of a molecule in the next frame is recognized as the one closest to the original position. The first assumption is inherent to the time resolution of the camera used for imaging. Faster cameras can record videos with shorter time intervals between frames, and thus can follow the faster motions of molecules. The second assumption can only be valid if the probe concentration in the medium is low enough and the steps are short enough (the diffusion is slow enough).

The linking of spots can be done manually or automatically, by computer program. In Chapter 5, the manual method as well as the automated method were used to obtain the D values of SRB molecules diffusing inside PEO microdomains.

2.2.2.4.3 *Manual Spot Detection and Linking*

The manual linking of the spots across the video frames is a meticulous job. Previous publications used this method to identify and create the trajectories to obtain the diffusion behavior of small molecules.^{41,104,105} The biggest problem with this approach is a possible bias in the linking due to human decision. Consequently, the automation of linking is more desirable to avoid this issue.

2.2.2.4.4 *Automated Spot Detection and Linking*

Several publications used the automated linking of fluorescent spots to create trajectories.^{101,106,107} These methods are faster and generate more trajectories. In general, the software picks one spot at a time and looks in the next frame to determine if there is another spot at a given distance. The threshold of the distance is defined by the researcher, but it is expected that the exposure time (frame duration) gives an estimate of the potential maximum length that the molecule can reach (using eq. 2.6).

Aside from the threshold selected by the user, there are two sources of error that can be identified from the assumptions and mechanisms used by the software. The first one is the localization error: If a molecule moves over a distance shorter than the localization precision (typically 20-30 nm in my measurements) it is considered to be immobile. The second one, which can be more relevant to the analysis, is caused by the crossing of molecular pathways (or

trajectories). This situation happens if another molecule appears closer to the position of a moving molecule of interest in the previous frame. In this case, the spots of two different molecules maybe linked, and therefore the trajectory will not correspond to the motion of a single molecule. Figure 2-8 shows the situation where the trajectory of a molecule of interest in blue is incorrectly created when a different molecule in red that shows up in the middle.

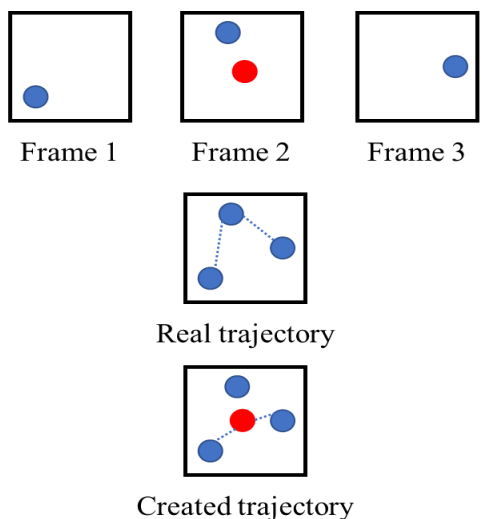


Figure 2-8: Schematic of how a crossing molecule can lead to erroneous trajectories. The top 3 frames show consecutive frames for one molecule (in blue). The trajectory from the single molecule is shown as “real trajectory”. However, a new molecule (in red) appears in frame 2, giving a “bad” linking as indicated by “created trajectory” for comparison.

The “bad” linking gives a smaller D value due to the creation of a false shorter trajectory. Therefore, the automated spot detection with quantified human bias can also lead to false trajectories. Furthermore, the probability of bad linking increases for molecules moving faster. Nevertheless, the threshold selected in the software are figures that can be used to discuss the bias of the linking in comparison with the manual linking which has no figures that allows the discussion of the possible bias as a factor.

3. Materials and Characterization Methods

This chapter summarizes information about polymers used in this dissertation as well as how they are made and characterized. In Chapter 4, poly(ethylene terephthalate) (PET) track-etched membranes were used to demonstrate controlled modification of the inner surface of their pores via a click reaction. In Chapter 5, the swelling of a series of polymers, including polystyrene homopolymer (PS_{16.4}), poly(ethylene oxide) homopolymers (PEO_{3.8} and PEO_{12.5}) and polystyrene-*block*-poly(ethylene oxide) (PS_{15.5}-*b*-PEO₄ and PS₃₅-*b*-PEO_{10.5}), upon solvent vapor exposure was studied. All materials are polymer based, despite their chemistry and different applications as well as the method of synthesis and preparation. Figure 3-1 shows the molecular structure of the polymer used in this thesis. This information will provide readers with the necessary background to understand the projects presented in the next chapters.

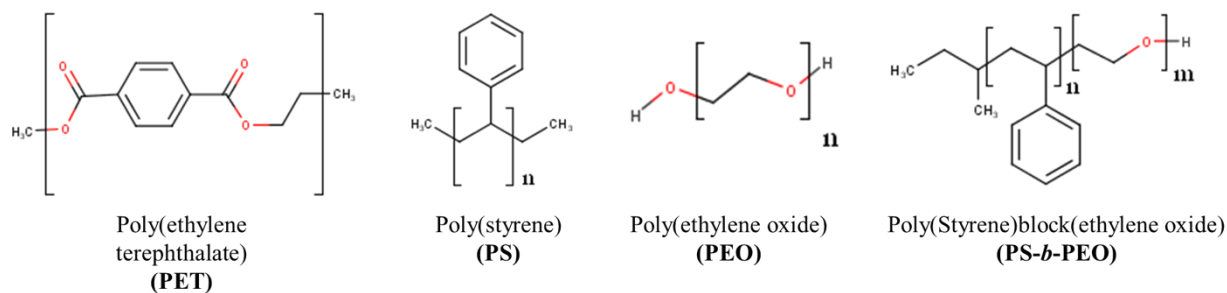


Figure 3-1: Molecule structures of poly(ethylene terephthalate) (PET), polystyrene (PS), poly(ethylene oxide) (PEO) and polystyrene-*block*-poly(ethylene oxide) (PS-*b*-PEO), which were used in the projects of this thesis.

3.1 Poly(ethylene terephthalate) Track-Etched Membrane

3.1.1 Poly(ethylene terephthalate) (PET)

This polymer was patented in 1941 by J. R. Whinfield and J. T. Dickson in Manchester, United Kingdom.¹⁰⁸ Commonly known as one of the largest pollutants due to its use mainly in the manufacturing of plastic bottles,¹⁰⁹ this material has, nevertheless, great properties if it is used with right purposes. It is a flexible, colorless plastic that is stable at high temperature and against a wide range of chemicals. All those characteristics make PET a great material for filtration membranes.^{110–113}

3.1.1.1 Track-Etched Membrane Fabrication

PET is synthesized via the transesterification reaction of ethylene glycol and dimethyl terephthalate.¹¹⁴ The pores of a PET track-etched membrane are created by bombarding a PET sheet with heavy ions. The pore density is controlled by the flow of heavy ions. Subsequently, the nuclear tracks (regions where the heavy ions have passed through) are chemically etched in an aqueous NaOH solution to obtain pores with a diameter controlled by the conditions of the etching process (time and etching reagent concentration).¹¹⁵ Figure 3-2. shows the schematic procedures from the polymerization to the pore preparation. This method gives carboxylic groups on the inner pore surface that can be used for further modification (Chapter 4).

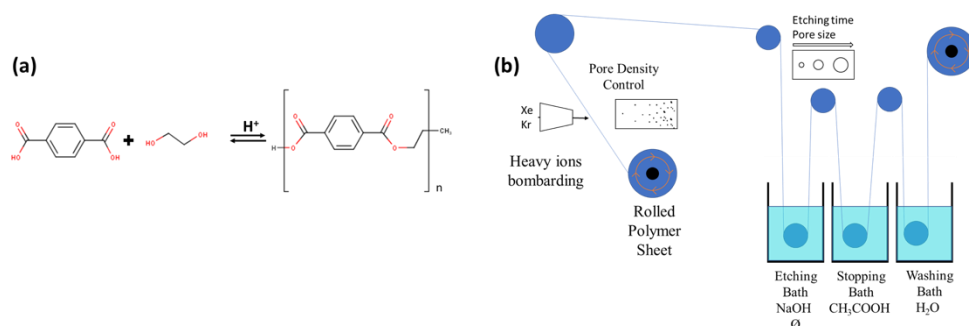


Figure 3-2: (a) Synthesis of PET. (b) Fabrication of a PET track-etched membrane. Polymer PET sheet is bombarded by heavy ions and the resulting nuclear tracks are etched to get pores of a desired size. Stopping solution serves to neutralize the basic solution and stop the etching process.

3.2 Block Copolymers

A block copolymer is defined as a polymer made of multiple different monomer blocks linked covalently.¹¹⁶ The adjacent blocks are different in chemical composition and/or structure. A diblock copolymer (DBC) consists of two distinct polymer chains, linked by a covalent or a non-covalent bond. The compatibility of the two blocks controls the microphase separation of a DBC,¹¹⁷ which leads to the formation of periodic uniform nanostructures. Microphase separation is defined by Matsushita as¹¹⁸ the “phenomenon generated by block copolymers composed of incompatible chemical components, where they tend to spontaneously form phase-separated structures with microscopic length scales due to intramolecular phase separation in bulk or in concentrated solutions.” As a result of the microphase separation, DBCs end up with different morphologies and domain sizes in the nanometer scale (i.e., 10-100 nm). In addition, given the variety of synthetic routes, it is possible to synthesize DBCs with different combinations of block polymer chain lengths (n_x) and the properties of polymer block,¹¹⁹ which allows tuning the size and morphology of the resulting microdomains.^{120,121}

Microphase separation is the result of the immiscibility of the blocks, as mentioned above.¹²² A possible morphology that a particular DBC will provide can be predicted from the

polymerization degree (N), the volume fraction (f_A) and the Flory-Huggins parameter (χ), the latter of which is the chemical incompatibility or the degree of immiscibility as a proportion to the heat of mixing.^{120,123,124} Figure 3-3 shows the theoretical phase diagram for a linear DBC calculated using the self-consistent mean field theory and the predicted equilibrium morphologies.^{125,126} However, microdomain morphology in DBC thin films is controlled not only by the nature of each block and interactions between the two blocks, but also by interactions at the air-film and film-substrate interfaces. Therefore, DBC microdomains in thin films can appear in different morphologies, and need to be controlled according to their applications.¹²⁷

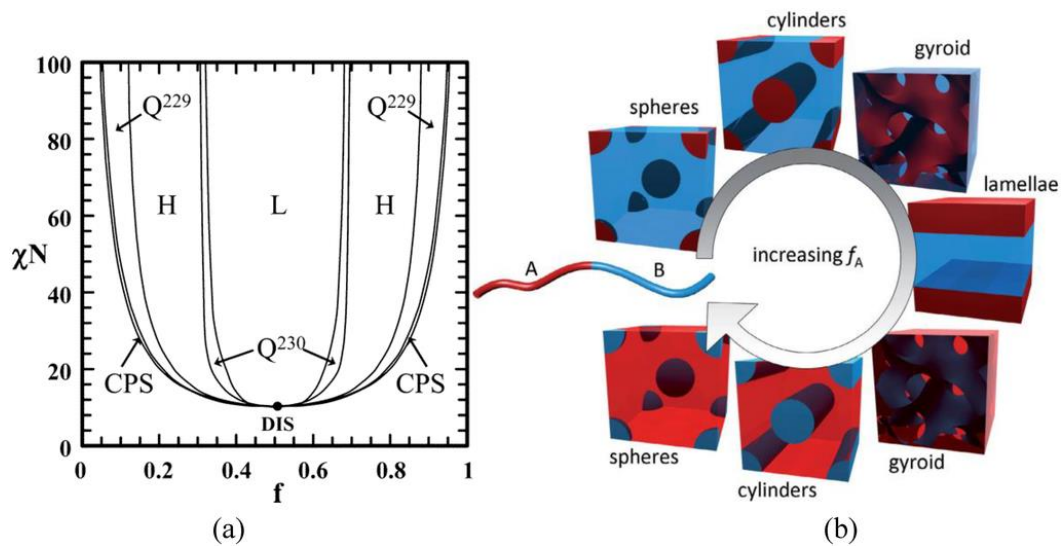


Figure 3-3: Theoretical phase diagram for a linear DBC calculated using self-consistent mean-field theory. DBC morphologies depending on the volume fraction are also shown: From right to the left: sphere (S), cylinder (C), gyroid (G), and lamella (L). For a volume fraction larger than 0.5, the inverse structure is expected. Reproduced with permission from Ref¹²⁸. Copyright 2010 Elsevier.

DBC thin films are relevant for many applications like optoelectronics,¹²⁹ anti-reflection coatings,¹³⁰ nanotempling^{3,131–135} or nanoporous membranes.^{3,136–138} However, the applicability of DBC thin films depends strongly on the nature of the DBC itself, and therefore further research of

these materials may unveil unexpected applications in the future. This thesis will focus on thin films of PS-*b*-PEO comprising cylindrical PEO microdomains that orient horizontally on underlying substrates.

3.2.1 Polystyrene-*block*-Poly(ethylene oxide) (PS-*b*-PEO)

This specific DBC is made of one glassy block of polystyrene and a more rubbery block of poly(ethylene oxide). Figure 3-1 shows the molecular structure of PS-*b*-PEO. Like other DBCs, PS-*b*-PEO is suitable for many applications like nanoporous membrane fabrication or as a template for nanomaterial synthesis. However, the most important feature that drives the attention of many researchers is the Li⁺ transport ability of PEO microdomains with the PS microdomains as a structural scaffold, making this material suitable as solid electrolytes for Li batteries.²

The morphology of the microdomains after spin coating is the result of the kinetic entrapment of the states due to fast evaporation of the solvent.¹³⁹ This morphology in thin DBC films can be modified using solvent vapor annealing (SVA).¹⁴⁰⁻¹⁴³ In this process, the thin film is exposed to a single solvent vapor or to a vapor of mixed solvents for a certain period of time, until the domains are organized. The reorganization of the domains is mainly ruled by the interfacial energy at the air/film interface while the film is swollen by solvent vapor in the chamber.¹⁴⁴

3.2.1.1 Polystyrene (PS)

PS was discovered in 1839 by an apothecary named J. E. Simon in Berlin. He distilled a resin from the tree/bush "*Liquidambar orientalis*" and found that the resulting liquid became more viscous after a few days. He named it "styrol". Hermann Staudinger, a Nobel prize winner who established the concept of "macromolecules", studied, characterized and clarified its structure

(Figure 3-1).¹⁴⁵ After many years of studies and patents, this material has become one of the most popular polymers used for packaging.

This polymer is a glassy solid polymer at room temperature and can be heated up to 100°C, its glass transition temperature. It is electrically insulating, non-polar, highly soluble in organic solvents, and optically transparent with a refractive index of 1.6. Due to these properties, most tissue culture dishes in laboratories are made from this material. This specific use has motivated researchers to study this material related to the protein adsorption process.^{146,147}

3.2.1.2 Poly(ethylene oxide) (PEO)

PEO was first reported in 1859 by A. V. Lourenco. It was formed as the result of the condensation of ethylene glycol and ethylene dibromide.^{148,149} The modern and rigorous characterization of the PEO was done by Hermann Staudinger.¹⁴⁵ It is important to clarify that this polymer is also called poly(ethylene glycol) (PEG). The reason for the name change is the length of the polymer. Conventionally, polymers with a number of monomers <150 are called PEG, otherwise PEO.^{150,151}

This polymer is soluble in water as well as in some organic solvents. It has different crystal structures. Its refractive index is around 1.4, but is smaller for a polymer with a longer chain.¹⁵² It is widely used as a non-toxic additive material in the food, pharmaceutical and cosmetic industries (approved by the FDA).^{153,154} PEO can form complexes with various molecules and ions such as lithium ion,¹⁵⁵ and has been examined as a solid electrolyte for Li batteries.^{156,157} In addition, PEO has been studied as a coating material to reduce the non-specific adsorption of proteins.¹⁵⁸

3.3 Instrumentation Used for Material Preparation and Characterization.

There are a number of methods for sample preparation and characterization of relevance to this dissertation.⁸ This chapter will cover those used for sample preparation and characterization in this dissertation. Fluorescence microscopies are explained in detail in Chapter 2 and therefore, they will be mentioned only briefly in this chapter.

3.3.1 Sample Preparation Methods.

There are as many methods for sample preparation as type of samples. The strategy of each method is related to the application or studies to which the sample will be subjected to. Sample preparation is the beginning of any research and it must be done carefully to avoid unnecessary extra steps that might contribute to errors. As an example, in Chapter 5 all the films used for the fluorescence SMT, must be done with care, avoiding any source of un-identified fluorescence spots. This was accomplished by cleaning the substrates extensively, followed by plasma cleaning (to remove any organic material) and using ultrapure solvents (HPLC grade) for all the solutions.

In Chapter 4, PET track-etched membranes with cylindrical pores were purchased from a company, and those with conical pores were prepared by Ms. Siepser and Prof. Baker at Indiana University as briefly explained in Section 3.1. Thin films used in Chapter 5 were prepared by spin coating on silicon substrates or glass coverslips.

3.3.1.1 Spin Coating

Spin coating is a procedure commonly used to prepare a thin polymer film on a flat surface. The major advantage of this method is the quicker formation of uniform thin films (from nm to μm in thickness) compared with other methods.^{159,160} Figure 3-4 shows the scheme of the process

including (i) the placement of a solution of interest on a substrate, (ii) the spinning of the substrate during which excess solution is expelled by the centripetal force, and (iii) the formation of a uniform film upon airflow drying.

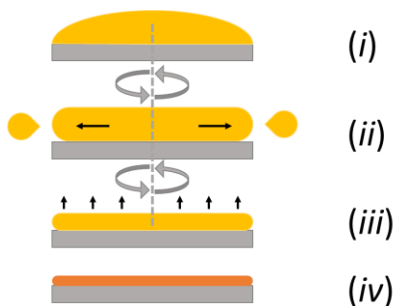


Figure 3-4: Spin coating process to form a thin film from a polymer solution. (i) A solution is placed on a substrate; (ii) The substrate is spun to remove excess solution; (iii) The solvent remaining on the substrate is evaporated by airflow during spinning; (iv) A uniform thin film is formed after being completely dried.

Film thickness can be controlled by the rotational force applied, i.e., the speed of rotation or by controlling the density of the solution. In addition, spinning time is decided on the basis of the nature of the solvent (boiling point). In any case, the solvent of a solution must be volatile under the conditions used for the spin coating process. For example, 30 seconds are recommended for water or short alcohols.^{161,162}

In Chapter 5, the spinning time was 40 seconds and 2000 RPM (rotations per minute) was the fixed speed used to prepare thin films. The different thickness was done by changing the polymer solution concentration.

3.3.2 Sample Characterization

As expected, the nature of a sample determines applicable characterization methods. Appropriate methods need to be selected to measure properties or features of interest. In this

dissertation, spectroscopic ellipsometry was used to measure the thickness of thin polymer films, and atomic force microscopy was used to measure their microdomain morphology. Cyclic voltammetry was used to determine the potential required to generate a Cu(I) catalyst at an electrode. Knowing the objective of the measurement is the key to choosing a suitable characterization method.

3.3.2.1 Spectroscopic Ellipsometry (SE)

Spectroscopic ellipsometry is a non-destructive and non-invasive optical analytical technique used to obtain thickness data and optical constants, such as refractive index (n) or extinction coefficient for thin films. Depending on the specifications of the SE manufacturer, the thickness range that can be measured can range from 0.1 nm to 6 μm . Because this technique can measure optical constants without damaging or contacting the sample, it is commonly used for films, optical components, semiconductors for solar panels, and other applications.^{163,164}

This technique measures the change in the phase, and amplitude of linearly polarized light upon reflection from sample/air and sample/substrate interfaces. Figure 3-5 shows the experimental set up that explains how the measurement is done.

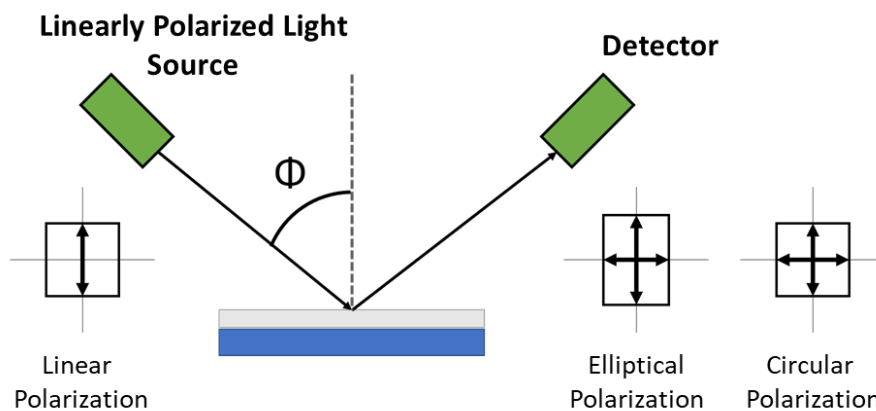


Figure 3-5: Experimental set up of spectroscopic ellipsometry.

The amplitude and phase of the reflected light is measured by the detector and compared with the known phase and amplitude of the linearly polarized light source. The parameters obtained using eq 3.1, are the amplitude ratio ($\tan \Psi$) and the phase difference (Δ).

$$\rho = \frac{\rho_{\pi}}{\rho_{\sigma}} = \tan(\Psi) e^{j\Delta} \quad \text{eq. 3.1.}$$

In eq 3.1, ρ_{π} and ρ_{σ} are reflection coefficients of the light that is polarized parallel and perpendicular to the plane of incidence (Fresnel plane), ρ is the complex ratio, and j is a number related to the cycles of the wave. Psi (Ψ) and delta (Δ) are the parameters collected by the instrument. These values are plotted against wavelength and fitted with an appropriate model created by the user. Monochromatic ellipsometry uses a single wavelength incident beam and therefore only one pair of Psi (Ψ) and delta (Δ) values is obtained. For the case of the spectroscopic ellipsometry, as the name suggests, the incident light sweeps a range of wavelengths and in consequence there is a pair of Psi (Ψ) and delta (Δ) values for each incident wavelength.

The most important information that the model should include are the number of reflective layers the sample has, and type of the material comprising the layers. In our case, we have a single layer of a transparent polymer film. The best model to fit the data is based on the Cauchy dispersion formula (defined by Augustin-Louis Cauchy in 1836).¹⁶⁵ This Cauchy dispersion formula describes the refractive index as a function of the incident wavelength, under the assumption that the material has no optical absorption in the visible spectral range and a normal dispersion. Under those considerations, the refractive index decreases when the wavelength increases, as is shown below in eq. 3.2. Coefficients A; B; C and D depend on the material and are determined empirically.

$$n(\lambda) = B + \frac{C}{\lambda^2} + \frac{D}{\lambda^4} + \dots \quad \text{eq. 3.2.}$$

To know the best model for the sample, the software calculates the response for Fresnel's equations for all the different layers of the model and compares the prediction with the experimental data. From that comparison, the unknown variables are fitted to get the estimated thickness (d) and refractive index (n) of each of the layers. It is also possible to obtain other features of the probed layers such as roughness of the surface.

Potential sources of error in the thickness measurement encountered during research were the roughness of the thin film surface and the tilting of the sample given by the residue of polymer solution that was attached on the backside of the substrate during spin coating. Roughness can be avoided by practice (careful cleaning of the underlying substrates, homogeneity of the solution and good control of the spin coating conditions). Tilting of the film during SE can be solved by using larger pieces of substrates during spin coating or by a gentle cleaning of the backside of the substrate using a piece of cotton and acetone or another solvent to remove the polymer.

3.3.2.2 Sample Characterization Using Microscopy

As mentioned in Chapter 2, optical microscopy has been used since 1600s with the development of Antonie Van Leeuwenhoek's first microscope to characterize and observe a wide variety of samples. From blood cells to charcoal particles in ethanol, this characterization method has provided a vast amount of information about a wide range of samples. The background and the details of fluorescence microscopic techniques used were covered in Chapter 2, and this section mainly focuses on atomic force microscopy, which is based on a totally different principle.

3.3.2.2.1 Fluorescence Microscopy

A detailed explanation of fluorescence microscopy is given in Chapter 2. In this thesis, the following fluorescence microscopy techniques were used:

1. Wide-field fluorescence microscopy to assess the surface modification of pores in PET track-etched membrane by electrochemically-controlled click reaction.
2. Two-window fluorescence wide field microscopy to assess environmental polarity around NR molecules incorporated into thin polymer films.
3. SMT to measure the diffusion behavior of single SRB molecules in polymer thin films before and after solvent-induced swelling.
4. FCS to quantify the diffusion coefficient of SRB molecules in thin polymer films before and after solvent-induced swelling.

3.3.2.2.2 Atomic Force Microscopy (AFM)

Atomic force microscopy (AFM) is a type of scanning probe microscopy where the topography of the sample is explored by a nanometer scale probe (tip). Figure 3-6 shows the instrumental setup of AFM.

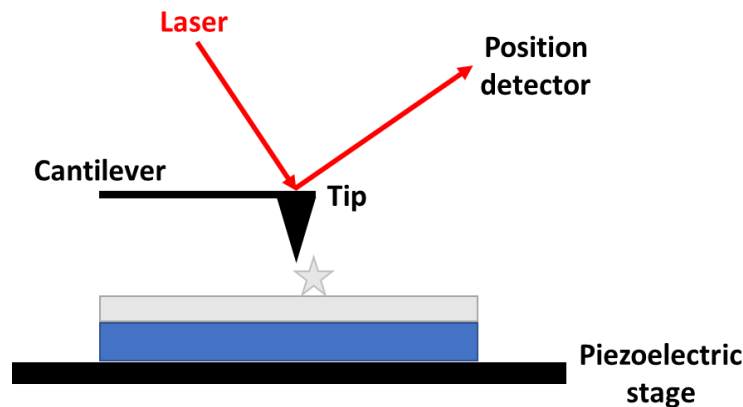


Figure 3-6: Experimental setup of AFM. The position of the tip on the sample surface is controlled by the piezoelectric stage, and the vertical and torsional deflection of the cantilever is measured from the position of a laser beam reflected on the cantilever.

AFM relies on a force between the end of the tip and the surface of the sample. The force can be measured from a displacement of the tip from the equilibrium position (Δz) that can be obtained from the position of a laser beam reflected at the cantilever using Hooke's law:

$$F = -k \Delta z \quad (\text{eq. 3.3})$$

In this equation, k is the spring constant of the cantilever reflecting its stiffness. While the tip scans the surface, a laser beam hits the cantilever. Depending on the forces and interactions between the tip and the surface, the cantilever bends and reflects the laser beam to a different position onto the detector (photodiode). Usually, a topography image of the surface is created by scanning the sample with the tip while keeping the laser position fixed.

In this thesis, the tapping mode was used. This mode is commonly used to measure the surface topography of soft materials or materials submerged in liquids. In this method, the cantilever needs to be oscillated at a frequency close to its resonance frequency. This oscillation makes the tip encounter the surface several times but not stay on it, preventing the tip from damaging the sample surface. Aside from the topography, the chemical nature of the materials exposed on the surface can also be explored. As the result of the different interaction between the tip and the surface (Van der Waals, dipole-dipole, among others) the frequency changes. The images obtained from this strategy are known as phase images.

3.3.2.3 Electrochemical Methods

There is a long list of different electrochemical characterization methods.¹⁵ Many of these characterizations are based on a redox reaction. This reaction is a chemical reaction involving the gain or loss of electrons, like reactions taking place in batteries. Figure 3-7 shows the schematics

of a galvanic cell where the oxidation of the Zn is happening at the anode and the reduction of Cu at the cathode.

Electrochemical methods measure current (I) and voltage (V) from the system and can be used to extract information about the thermodynamics and kinetics of processes happening in the cell. The cell is the name for the minimal required setup in any electrochemical characterization or experiment. The scheme below, shows the simplest case with a cathode and an anode. The cathode and the anode are where the reduction and oxidation happen respectively. The flow of electrons (I) goes from the anode towards the cathode.

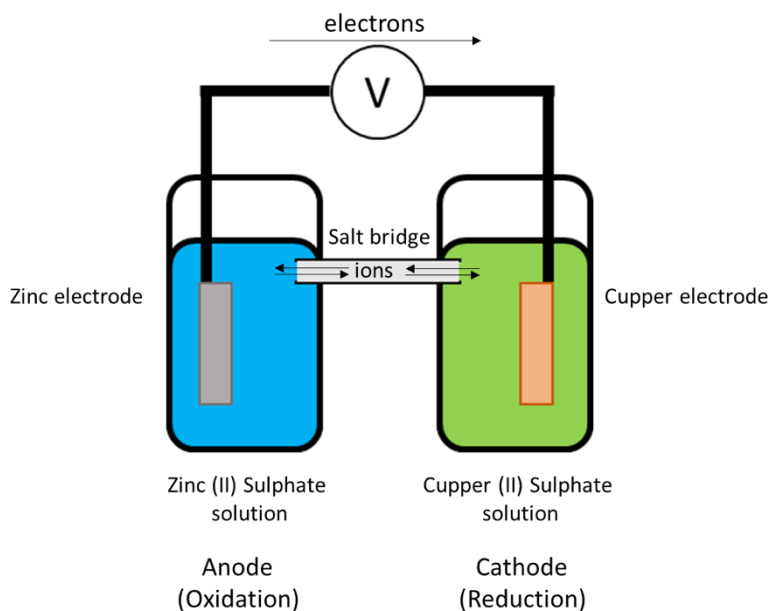


Figure 3-7: Scheme of a galvanic cell with a cathode and an anode. Copper (II) ions in the right solution gains electrons at the copper electrode while zinc at the zinc electrode loses electrons to be zinc (II) ions, making the electrons flow from the zinc electrode to the copper electrode.

3.3.2.3.1 Cyclic voltammetry (CV)

Cyclic voltammetry (CV) measures the current at a working electrode as a function of a potential applied to the electrode at a constant potential sweep rate (V/s).^{8,15,166} From the information of the current plotted against potential it is possible to identify the electrochemical

variables and conditions of the system such as redox potential and diffusion behavior of the redox species or reversibility of the electrochemical system.

As the potential applied to the working electrode is changed at a certain rate, going from the initial potential ($E_{initial}$) to the returning potential (E_{return}) and coming back, the current is measured. The scheme in Figure 3-8a shows the typical triangular potential application in a CV and the typical cyclic voltammogram in Figure 3-8b.

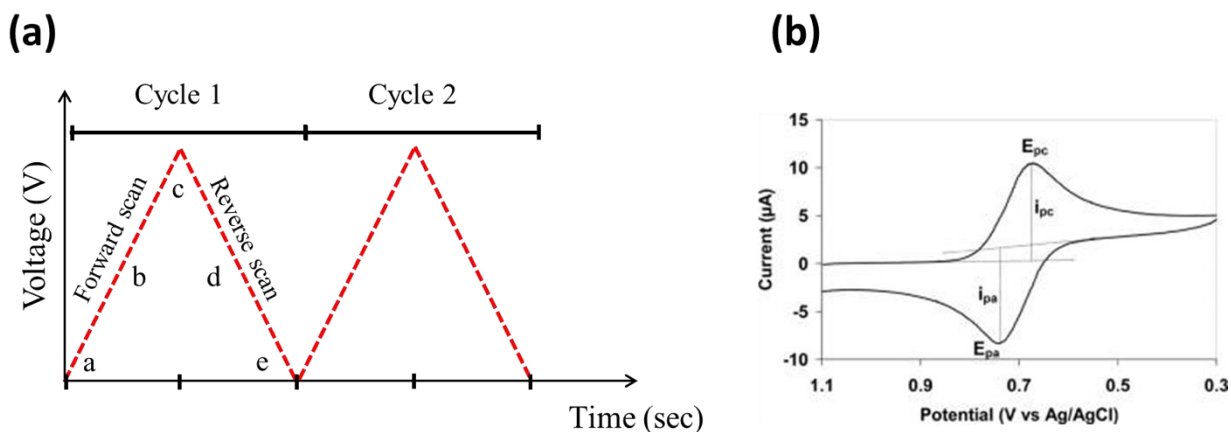


Figure 3-8: (a) Typical triangular potential waveform application. Point *a* refers to the initial potential ($E_{initial}$); *b* to the potential at the cathodic peak current (i_c); *c* is the returning potential (E_{return}); *d* is the anodic peak current (i_a); and *e* is the initial potential (E_{final}). (b) Typical cyclic voltammogram. Reproduced with permission from Ref. ¹⁵. Copyright 2001 Wiley.

The cathodic peak (E_{pc}) and the anodic peak (E_{pa}) are the potentials at which the maximum current is observed. These values, in part, depend on the nature of the redox species and the solution conditions close to the electrodes. Actually, electrode size and mass transport modes of the redox species to the electrode define the shape of a cyclic voltammogram. In a cyclic voltammogram, a faradaic current (which results from the redox reaction) and a non-faradaic current (which comes from changes in the electrical double layer) are observed. As a result, the cathodic current (i_c) and the anodic current (i_a) must be obtained by subtracting the non-faradaic current (lines in grey in Figure 3-8b).

The potential at which the maximum current is observed depends on the nature of redox species and solution conditions close to the electrodes. This method was used in Chapter 4 to select an optimum potential to reduce Cu (II) into Cu(I), the latter of which is the catalyst for the click reaction between alkene groups tethered to the inner surface of track-etched pores and the azide group of a fluorescent dye molecule.

4. Longitudinally Controlled Modification of Cylindrical and Conical Track-Etched Poly(ethylene terephthalate) Pores Using and Electrochemically Assisted Click Reaction¹⁶⁷

Modified with permission from the American Chemical Society.

Published as: Herman Coceancigh, Khanh-Hoa Tran-Ba, Natasha Siepser, Lane A. Baker, and Takashi Ito, *Langmuir* **2017**, 33, 43, 11998-12006.

<https://doi.org/10.1021/acs.langmuir.7b02778>

4.1 Contribution of Authors

TI directed the overall project. NS and LAB prepared PET membranes with conical pores and recorded their TEM images. KHTB did the simulations. HC prepared and designed the gold electrodes by photolithography, performed the membrane pre-modification, the electrochemically-assisted modification, the chemically assisted modification, and measured the horizontal and cross-sectional images with fluorescence microscopy. TI and HC analyzed the images.

4.2 Introduction

Porous membranes with asymmetric chemical compositions on each side have recently attracted considerable interest because of their unique mass transport properties.¹⁶⁸ For example, membranes with asymmetric wettability could be used for efficient oil-water separation based on their directional liquid transport properties.^{169–171} Membranes comprising nanopores with

asymmetric charge properties exhibited unique ionic current rectification behavior that may lead to development of a nanofluidic diode¹⁷² and an ion pump.¹⁷³ These asymmetric membranes have been prepared by the sequential deposition of different fibrous materials or by the asymmetric post-modification of monolithic porous materials.¹⁶⁸

The post-modification has been carried out via a photochemical reaction or a covalent chemical reaction that takes place directionally from one side of a monolithic material.¹⁶⁸ The former can be used mainly for polymeric membranes because it requires the light-induced degradation or cross-linking of the membrane surface/matrix. The latter is applicable for various porous materials on the basis of well-established reactions such as silanization and click reaction.^{169,174,175} However, it is often challenging to reproducibly obtain asymmetric membranes with spatial control at the μm -scale, because the modification is controlled by the directional mass transport of a reactant or catalyst loaded from one side of a membrane.¹⁶⁸ Very recently, post-modification controlled by reactant/catalyst diffusion has been demonstrated for a porous material, and successfully afforded a mm-scale compositional gradient across the material with the higher reaction yield near the loading surface.¹⁷⁴ It should be noted that similar diffusion-based approaches have been used to fabricate in-plane compositional gradients on flat surfaces.¹⁷⁶

In the diffusion-controlled chemical approach, reactant/catalyst loading needs to be regulated for reproducible asymmetric modification of a porous material at μm -scale precision. Faradaic processes at an electrode can be used to control the spatial and temporal distributions of a reactant or catalyst, and thus have been utilized for the fabrication of μm -scale patterns on surfaces.¹⁷⁷ For example, in-plane compositional surface gradients were obtained on the basis of the electrochemically-controlled generation and diffusion of a catalyst in Cu(I)-catalyzed azide-alkyne cycloaddition (CuAAC) click reaction.^{178–180} However, to the best of our knowledge, there

is no report that demonstrates the longitudinally-controlled modification of porous materials by taking advantage of the electrochemical generation of a reactant or catalyst.

In this study, longitudinally-controlled pore modification was explored using electrochemically-assisted CuAAC based on Cu(I) catalysts electrochemically generated at an electrode. CuAAC in a homogeneous solution^{181–183} has been widely used for uniform modification of porous materials such as mesoporous silica,^{174,184–186} porous silicon^{187,188} and polymer monoliths¹⁸⁹ due to its high efficiency and versatility. These modified nanoporous monoliths were used to design catalytic materials¹⁸⁶ and interferometric sensors.^{187,188} Electrochemically-assisted CuAAC employs Cu(I) catalysts generated by the reduction of Cu(II) solutes upon controlled potential application to an electrode.¹⁹⁰ Based on the spatial and temporal control of the catalyst concentration, electrochemically-assisted CuAAC provides a means for position-selective modification of electrode surfaces^{190,191} and also for the fabrication of in-plane compositional surface patterns and gradients.^{179,180,192–194} As porous materials, poly(ethylene terephthalate) (PET) track-etched membranes were used because of their uniform pore sizes and cylindrical/conical shapes^{115,195} and also the capability to decorate the pore surfaces via amidation of the surface –COOH groups.^{115,196,197} Here, PET track-etched pores were first decorated with ethynyl groups, and then modified with azide-tagged fluorescent dyes via CuAAC based on electrochemically-formed Cu(I) catalysts diffusing along the pores (Figure 4-1). The spatial distribution and yield of pore modification with fluorescent dye(s) were measured using fluorescence microscopy. In this study, the electrochemically-controlled modification was demonstrated only for μm -scale pores due to the feasibility of their characterization, but the reported approach will be applicable for asymmetric functionalization of nanoporous monoliths.

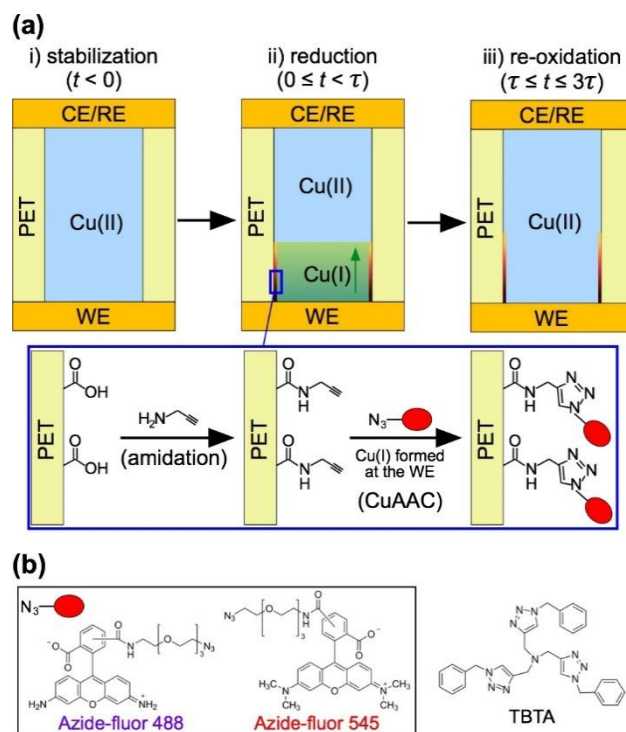


Figure 4-1: (a) Electrochemically-controlled pore modification based on CuAAC. (b) Chemical structures of azide-tagged fluorescent dyes and TBTA, a ligand to Cu(II/I). Reproduced with permission from Ref. ¹⁶⁷. Copyright 2017 American Chemical Society.

4.3 Experimental Procedures

4.3.1 Chemicals and Materials

Potassium hydroxide (KOH; Mallinckrodt Chemicals), formic acid (J. T. Baker), *N,N*-diisopropylcarbodiimide (DIC; Acros Organics), 1-hydroxybenzotriazole hydrate (Aldrich), propargylamine (Aldrich), *N,N*-dimethyl formamide (DMF; Fisher), sodium tetrafluoroborate (NaBF_4 ; Acros Organics), cupric sulfate pentahydrate ($\text{CuSO}_4 \cdot 5\text{H}_2\text{O}$; Fisher), tris[(1-benzyl-1*H*-1,2,3-triazol-4-yl)methyl]amine (TBTA; Aldrich), L-ascorbic acid (Acros Organics), Azide-fluor 545 ($\lambda_{\text{ex}} = 546 \text{ nm}$, $\lambda_{\text{em}} = 565 \text{ nm}$; Aldrich), Azide-fluor 488 ($\lambda_{\text{ex}} = 501 \text{ nm}$, $\lambda_{\text{em}} = 525 \text{ nm}$; Aldrich) and dimethyl sulfoxide (DMSO; Fisher) were used as received. The molecular structures of the fluorescent dyes as well as TBTA, a ligand to Cu(II/I),¹⁹⁸ are shown in Figure 4-1b. PET track-

etched membranes (25 mm in membrane diameter; it4ip) comprising cylindrical pores (1 μm in pore diameter, 22 μm thick, 2.5×10^7 pores/ cm^2) were purchased from AR Brown-US (Pittsburgh, PA). PET track-etched membranes with conical pores were prepared from ion-tracked PET films (12 μm thick, 1.5×10^6 tracks/ cm^2 ; it4ip) according to a previously-reported procedure¹⁹⁹ with slight modifications. A comb-shaped electrode was photolithographically fabricated from a gold-sputtered coverslip with a 200 nm-thick Au layer on a 10 nm-thick Cr layer (25 x 25 mm^2 ; LGA Thin Films, Foster City, CA) according to a procedure reported previously.²⁰⁰ A planar gold electrode on glass which was used as a counter/reference electrode, was purchased from Platypus Technologies (Madison, WI). All the water-containing solutions were prepared with water having resistivity of 18 $\text{M}\Omega\text{ cm}$ or higher (Barnstead Nanopure Systems or Millipore Corp).

4.3.2 Fabrication of a Comb-Shaped Gold Electrode

A gold-coated glass coverslip (25 x 25 mm^2 ; LGA Thin Films, Foster City, CA) was first cleaned with water, acetone and isopropanol and subsequently dried by heating at 60 $^\circ\text{C}$ on a hot plate. The substrate was spin-coated (1500 rpm, 40 sec) by a layer of primer solution (MCC Primer 80/20), followed by a layer of positive-tone photoresist (Shipley 1813TM, Rhom and Hass). The substrate was baked at 105 $^\circ\text{C}$ for 15 min to remove residual solvents. The photoresist was patterned by irradiation of UV light through a laser printed photomask with a desired pattern. The irradiated region was subsequently removed by rinsing in a developer solution (MicropositTM 351 Developer, Rhom and Hass), and then heated at 120 $^\circ\text{C}$ for 20 min to improve adhesion of the photoresist. The exposed gold layer was etched in 4:2:1 HCl:H₂O:HNO₃, and then the photoresist layer was removed by soaking the substrate with acetone. The resulting comb-shaped electrode consisted of nine ~ 0.3 mm rectangular teeth with a spacing of ~ 0.2 mm. The scheme of the

procedure, the mask designed for the comb shape electrode and the final electrode image is shown in Figure 4-2.

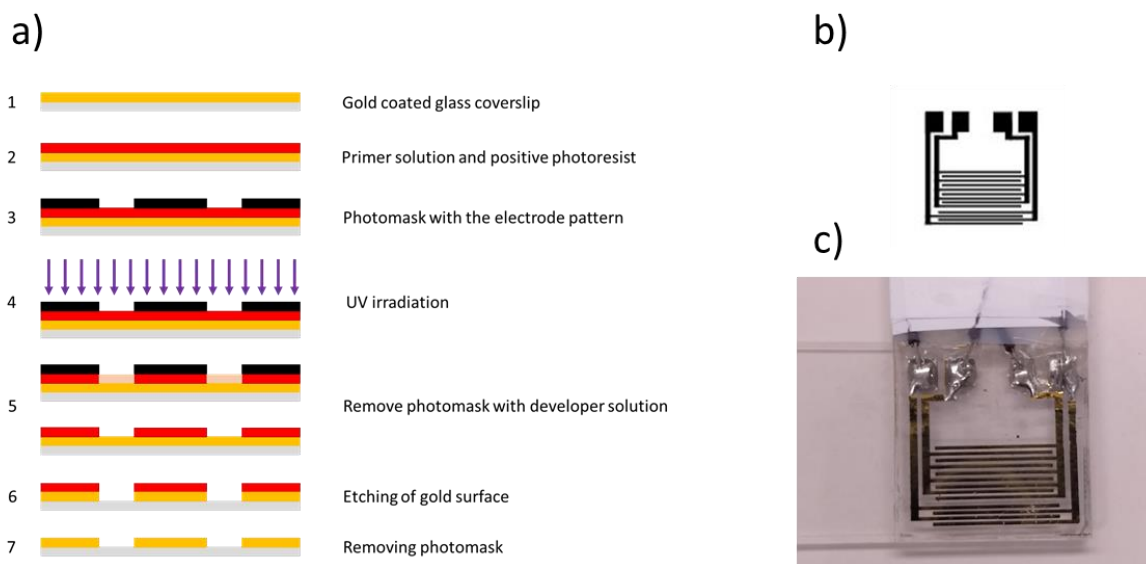


Figure 4-2: (a) Scheme of the fabrication procedure, (b) image of the electrode pattern used, and (c) photo of the final electrode as it was used for the experiments.

4.3.3 Pore Modification

First, ethynyl groups were tethered to the surface of PET track-etched pores via amidation of its -COOH groups according to the following procedure.^{197–201} A PET track-etched membrane was immersed in a DMF solution containing DIC (0.6% w/v) and 1-hydroxybenzotriazole hydrate (1.52% w/v) for 30 min. After being washed with DMF, the membrane was soaked in a DMF solution of propargylamine (1% w/v) for 3 hours. The membrane was washed with DMF and ethanol, and then dried in air at room temperature. It should be noted that pristine PET track-etched pores without surface ethynyl groups could not be modified via CuAAC (data not shown).

4.3.4 Electrochemically-Controlled Modification

Electrochemically-controlled pore modification was carried out as follows. An ethynyl-decorated membrane (*ca.* 0.5 x 1 cm²) was soaked in a DMSO:H₂O (1:1) solution containing fluorescent dye (0.04 mM), CuSO₄ (1 mM), TBTA (1 mM) and NaBF₄ (0.1 M), and then sandwiched between a comb-shaped gold electrode and a planar gold electrode (Figure 4-3a). Potential steps were applied to the comb-shaped working electrode (WE) against the planar counter/reference electrode (CE/RE), as shown in Figure 4-3b, using a WaveNow potentiostat (Pine Research Instrumentation). As a WE, a planar gold electrode instead of the comb-shaped gold electrode was used for the modification of conical PET track-etched pores. The applied potentials ($E_{\text{high}} = +0.5$ V; $E_{\text{low}} = -0.5$ V) were chosen from the cathodic and anodic potentials of Cu(II/I) measured in a solution of Cu(II) and TBTA with a two-electrode cell using cyclic voltammetry. As shown in Figure 4-3c, a cathodic peak for the reduction of Cu(II) and an anodic peak for the oxidation of Cu(I) were measured around -0.3 V and +0.2 V, respectively. Thus, almost all Cu(II) on the WE should be reduced at -0.5 V and almost all Cu(I) on the WE should be oxidized at +0.5 V.¹⁵ As a result, the potential steps shown in Figure 4-3b were anticipated to induce the following chemical processes (Figure 4-1a): During the reduction step at $E_{\text{low}} = -0.5$ V ($0 < t \leq \tau$; $\tau = 10, 30, 60, 120, 360$ or 1000 sec), Cu(I) was generated by the reduction of Cu(II) at the WE and then diffused toward the CE/RE along the pores. At the re-oxidation step ($\tau < t \leq 3\tau$), Cu(I) produced during the reduction step was oxidized to Cu(II) at the WE to stop the pore modification.

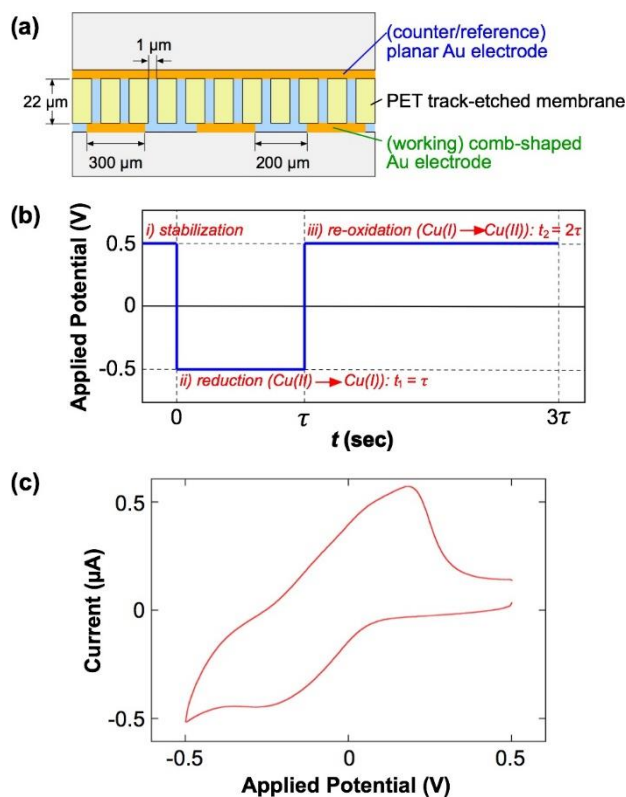


Figure 4-3: (a) Schematic illustration of an experimental setup used in this study. The experiments were carried out using a two-electrode cell consisting of a planar Au (counter/reference) electrode (CE/RE) at the top, a comb-shaped or planar Au (working) electrode (WE) at the bottom and a PET track-etched membrane sandwiched in between. (b) Potentials applied to the WE in the two-electrode cell. At the WE, Cu(II) was reduced to Cu(I) ($0 \leq t < \tau$; $t_1 = \tau$), and then the generated Cu(I) was oxidized to Cu(II) ($\tau \leq t \leq 3\tau$; $t_2 = 2\tau$). (c) A cyclic voltammogram recorded in a H₂O/DMSO (1:1) solution containing 1 mM CuSO₄, 1 mM TBTA and 0.1 M NaBF₄ using a two-electrode cell consisting of two Au disk electrodes (2 mm in diameter). Reproduced with permission from Ref. ¹⁶⁷. Copyright 2017 American Chemical Society.

Homogeneous CuAAC based on Cu(I) generated by Cu(II) reduction with L-ascorbic acid¹⁹⁸ was also explored for the modification¹⁹⁸ of a PET track-etched membrane comprising ethynyl-decorated cylindrical pores (1 μm in pore diameter). The membrane modification was carried out by immersing an ethynyl-decorated membrane in a DMSO:H₂O (1:1) solution containing Azide-fluor 545 (0.04 mM), CuSO₄ (1 mM), TBTA (1 mM), L-ascorbic acid (1 mM) and NaBF₄ (0.1 M) for 1000 sec, followed by rinsing with DMSO:H₂O (1:1) and water.

4.3.5 Fluorescence Microscopy Measurements

The spatial distribution and yield of pore modification with fluorescent dye(s) were assessed from the planar and cross-sectional fluorescence images of modified PET track-etched membranes (Figure 4-4). These images were recorded using a Nikon TE2000 inverted optical/fluorescence microscope equipped with FITC and TRITC filter cube sets and a Roper Scientific CoolSnap ES camera, and then analyzed using the ImageJ software. The excitation and emission wavelengths of the FITC filter set were 470 ± 20 (nm) and 535 ± 20 (nm), and those of the TRITC filter set were 542 ± 10 (nm) and 620 ± 26 (nm). A 10x objective lens (NA = 0.30) and a 100x oil-immersion objective lens (NA = 1.30) were used for the image acquisition. Planar images were measured for a membrane horizontally placed on a glass coverslip (Figure 4-4a). Cross-sectional images were obtained for a vertically-oriented membrane section obtained by cutting across modified band regions and supported between two planar glass substrates (Figure 4-4b).

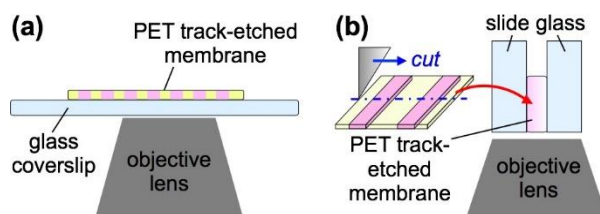


Figure 4-4: Fluorescence microscopy setups used for recording (a) a planar image and (b) a cross-sectional image. Modified areas in a membrane reflecting the positions of the teeth of a comb-shaped WE during the pore modification are schematically shown in pink. Reproduced with permission from Ref. ¹⁶⁷. Copyright 2017 American Chemical Society.

4.3.6 Finite-Element Computer Simulations

Finite-element computer simulations were carried out using COMSOL Multiphysics Version 4.1 operated on a Dell Optiplex GX 520 (Pentium 4 CPU, G GHz, 4 GB RAM).²⁰² The simulations were based on previously reported models^{180,193} with a different electrode geometry. Here, a vertically-oriented cylindrical pore (1 μm in diameter, 22 μm in length) between two planar electrodes were considered. Figure 4-5 shows the model geometries of cylindrical pores used in our simulations. We assumed a uniform hexagonal distribution of cylindrical pores (Figure 4-5a) with the center-to-center distance of 2.2 μm , which was estimated from a pore density (0.25 pores/ μm^2) provided by the manufacturer. We also considered the influences of a small gap ($d = 0, 0.1$ or 1 μm) between a membrane and an electrode, which could be formed due to their incomplete contact (Figure 4-5b). As a result, a cylindrical coordinate system shown in Figure 4-5b was used to simulate the pore modification. Its origin was set on the WE at the center of the pore, and thus the ranges of horizontal (r) and vertical (z) axes to be considered were $0 \leq r$ (μm) ≤ 1.1 and $0 \leq z$ (μm) $\leq (22 + 2d)$.

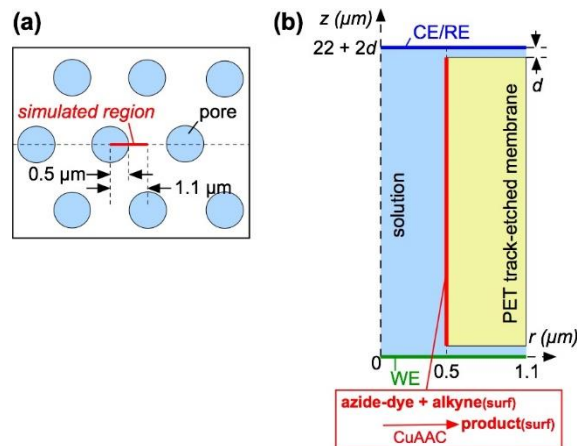
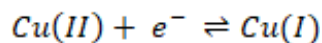


Figure 4-5: (a) Assumed hexagonal arrangement of the pores in the PET track-etched membrane with cylindrical pores (1 μm in diameter). The center-to-center distance of 2.2 μm was estimated from the pore density (0.25 pores/ μm^2). (b) Schematic illustration of the simulation

geometry of a cylindrical pore between two electrodes: The pore radius was 0.5 μm , the pore length defined by the membrane thickness was 22 μm , and the electrode-membrane gap was d ($= 0, 0.1$ or $1 \mu\text{m}$). The origin of the cylindrical coordinate system was set on the WE at the center of the pore. Reproduced with permission from Ref. ¹⁶⁷. Copyright 2017 American Chemical Society.

In the simulations, a simple single electron transfer was assumed for the redox reaction of Cu(II/I) at both the WE and CE/RE:



The reduction of Cu(II) ($0 < t \leq \tau$) and the re-oxidation of Cu(I) ($\tau < t \leq 3\tau$) at the WE (Figure 4-3b) were assumed to completely proceed because of the application of significantly large cathodic and anodic overpotentials ($\geq 120 \text{ mV}$), respectively (*vide supra*).¹⁵ Prior to the potential step application ($t < 0$), the potential applied to the WE was positive enough not to reduce Cu(II) to Cu(I). Note that the sum of Cu(I) and Cu(II) concentrations ($C_1(r,z,t)$ and $C_2(r,z,t)$, respectively) was assumed to be always equal to the initial Cu(II) concentration ($C_0 = 1 \text{ mol/m}^3$), which means $C_1(r,z,t) + C_2(r,z,t) = C_0$. In summary, the following boundary conditions for the Cu(I) and

Cu(II) concentrations could be set at the WE ($z = 0$):

$$\begin{aligned} C_1(r,0,t) = 0 \text{ and } C_2(r,0,t) = C_0 & \quad (t < 0) \\ C_1(r,0,t) = C_0 \text{ and } C_2(r,0,t) = 0 & \quad (0 \leq t < \tau) \\ C_1(r,0,t) = 0 \text{ and } C_2(r,0,t) = C_0 & \quad (\tau \leq t \leq 3\tau) \end{aligned} \quad (\text{eq. 4.2})$$

At the CE/RE, the Cu(I) concentration at the surface was assumed to be always zero due to the application of a sufficiently large anodic overpotential for the complete oxidation of Cu(I) to Cu(II). Thus,

$$C_1(r,z,t) = 0 \text{ and } C_2(r,z,t) = C_0 \quad \text{at } z = 22 + 2d \quad (0 \leq t \leq 3\tau) \quad (\text{eq. 4.3})$$

The diffusion of Cu(I) and azide-tagged dye was described by Fick's second law including a reaction term:^{180,193}

$$\frac{\partial C_1(r,z,t)}{\partial t} = \nabla (D_1 \partial C_1) + R(z,t) \quad (\text{eq. 4.4})$$

$$\frac{\partial C_d(r,z,t)}{\partial t} = \nabla (D_d \partial C_d) + R(z,t) \quad (\text{eq. 4.5})$$

The diffusion coefficients (D_l and D_d , m^2/s) of Cu(I) and azide-tagged dye were assumed to be similar to those of Cu(II) ($\approx 5 \times 10^{-10} \text{ m}^2/\text{s}$), which was experimentally obtained in the solution using chronocoulometry (data not shown). The initial dye concentration ($C_{d,0}$) was $0.04 \text{ mol}/\text{m}^3$. At the solution-pore interface, an azide-tagged molecule was immobilized onto a surface-tethered ethynyl group via CuAAC catalyzed by Cu(I) that was produced at the WE and diffused along the pore (Figure 4-5b). The kinetics of a CuAAC reaction is known to be first order for azide, and second order for Cu(I) and alkyne.¹⁸³ The reaction term of the reaction is thus assumed to be given as:

$$R(z,t) = k[C_d(0.5,z,t)][C_1(0.5,z,t)]^2[\Gamma(z,t)]^2 \quad (\text{eq. 3.6})$$

where k is the reaction rate constant,¹⁸⁰ C_d , C_l , Γ are the concentration of azide-tagged species (mol/m^3), Cu(I) (mol/m^3) and surface ethynyl groups (mol/m^2), respectively. The total surface ethynyl density (Γ_0) was taken from a paper that reported the yield of amidation on a pristine PET track-etched membrane.¹⁹⁷ All the constants and fixed parameters are summarized in Table 4-1.

4.3.7 Computational Procedure

In the COMSOL Model Builder, the space dimension was chosen as 2D axial symmetric (Figure 4-6) to reduce the computational time. The Fick's second law was solved using the Physics Model 'Transport of Diluted Species' with a time dependent solver. In addition, the surface-bound reaction of an azide-tagged species with a surface alkyne group was simulated by a Physics Model 'General Form Boundary PDE' together with a time dependent solver. Importantly, both models

had to be directly coupled to simultaneously simulate the diffusion of the species based on Fick's second law and the reaction at the pore wall (eq. 4.4 and eq. 4.5).

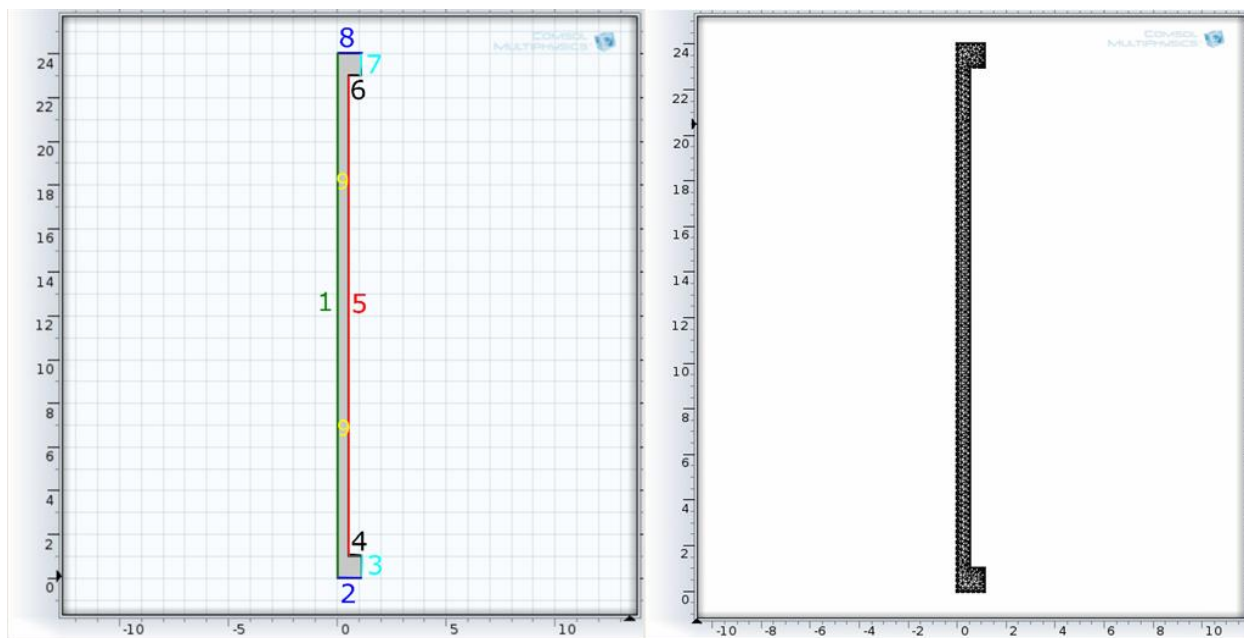


Figure 4-6: (a) Model geometry ($d = 1 \mu\text{m}$) showing eight boundaries (1-8) and one domain (9). (b) Illustration of the mesh size used in the COMSOL simulations for the functionalization of a pore ($0.5 \mu\text{m}$ in radius, $22 \mu\text{m}$ in length, $d = 1 \mu\text{m}$). The model was built by Dr. Khanh-Hoa Tran-Ba. Reproduced with permission from Ref. ¹⁶⁷. Copyright 2017 American Chemical Society.

In the diffusion model, the ‘No Flux’ boundary conditions were set for Boundaries 4 and 6. The ‘Axial Symmetry’ conditions were chosen for Boundaries 1, 3 and 7. The ‘Flux’ boundary conditions for Boundaries 2 and 8 were set to be eq. 3.2 and eq.3.3, respectively. At the reacting surface (Boundary 5), the ‘Inward Flux’ of Cu(I) was described by eq. 4. ‘Initial Values’ represented the initial bulk concentrations of Cu(I) ($= 0$), Cu(II) ($C_0 = 1 \text{ mol/m}^3$) and azide ($C_{d,0} = 0.04 \text{ mol/m}^3$) for Domain 9. To simulate the diffusive motions of all species, diffusion coefficients (Cu(I): $D_1 = 5 \times 10^{-10} \text{ m}^2/\text{s}$, Cu(II): $D_2 = 5 \times 10^{-10} \text{ m}^2/\text{s}$, azide: $D_d = 5 \times 10^{-10} \text{ m}^2/\text{s}$) were set in ‘Diffusion’ for the entire cell (Domain 9), as shown in Figure 4-6b.

Table 4-1: Fixed Parameters and Constants Used in the COMSOL Simulations.

Fixed Parameters	Determined or estimated values/units
Total Cu concentration (C_0)	1 mol/m ³
Initial azide dye concentration ($C_{d,0}$)	0.04 mol/m ³
Cu(I), Cu(II) diffusion coefficients (D_1, D_2)	5 x 10 ⁻¹⁰ m ² /s
Azide-tagged dye diffusion coefficients (D_d)	5 x 10 ⁻¹⁰ m ² /s
Electrode-membrane gap size (d)	0 (or 1 x 10 ⁻⁷ m, 1 x 10 ⁻⁶ m)
Initial density of surface ethynyl groups (Γ_0)	1.3 x 10 ⁻⁷ mol/m ²
CuAAC reaction rate constant (k)	32.69 m ¹² /(s•mol ⁴) ³⁸

The reaction at the pore wall (Boundary 5) was simulated with a ‘General Form Boundary PDE’ Physics Model. The ‘Initial Value’ of the azide and Cu(I) concentrations were set to $C_{d,0} = 0.04$ mol/m² and $C_1 = 0$, respectively. The ‘Initial Time Derivative’ was 0 for both species. The ‘General Form PDE’ consisted of a conservative flux for azide-tagged dye ($-D_d(dC_d/dr)$ and $-D_d(dC_d/dz)$ for r and z -components, respectively) and Cu(I) ($-D_1(dC_1/dr)$ and $-D_1(dC_1/dz)$ for r and z -components, respectively). The ‘Source Term’ was set to $R(z, t)$ (for r and z -components) according to eq. 4.6. In addition, $\frac{\partial C_1(r,z,t)}{\partial t}$ and $\frac{\partial C_d(r,z,t)}{\partial t}$ were accounted in the model by choosing appropriate ‘Damping or Mass Coefficient’ of 1.

In the simulations, an overall, ‘user-defined’ mesh was chosen. The element size was pre-calibrated for ‘General Physics’ at a pre-defined ‘extremely fine’ setting. Specifically, a maximum element size of 0.24 μ m, a minimum element size of 0.5 nm, a mesh grow rate of 1.1 and a mesh curvature factor of 0.2 were employed. The mesh type was chosen to be ‘free triangular’ with a 1:1 aspect ratio. Typically, for $d = 0$ μ m, the number of triangular elements was ~600, the edge elements were ~200 and a mesh area was 11 μ m². One typical simulation with a 10⁻⁴ relative

tolerance required < 5 min. Figure 4-6b depicts a model geometry with typical mesh that was generated using the conditions described above. Here, the simulation cell had a height of $24 \mu\text{m}$ (consisting of the pore length and the two electrode-membrane gaps of $1 \mu\text{m}$). The surface functionalization was obtained from the integration of $R(0.5, z, t)$ by time using the ‘timeint (t_{start} , t_{end} , function)’ operator.

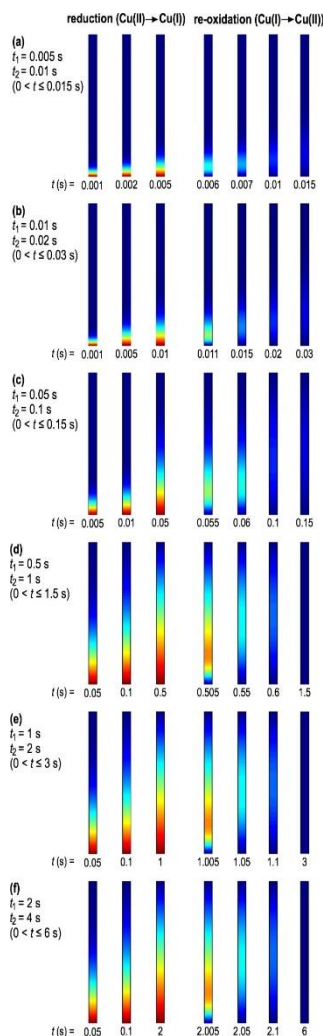


Figure 4-7: COMSOL simulation results on the time dependence of Cu(I) concentration profile within a pore ($0.5 \mu\text{m}$ wide, $22 \mu\text{m}$ high, $d = 0$) at different t for different t_1 – t_2 conditions. The Cu(I) concentration ranges from 0 mol/m^3 (blue) to 1 mol/m^3 (red). The bottom boundary represents the WE. The data were obtained by Dr. Khanh-Hoa Tran-Ba. Reproduced with permission from Ref. ¹⁶⁷. Copyright 2017 American Chemical Society.

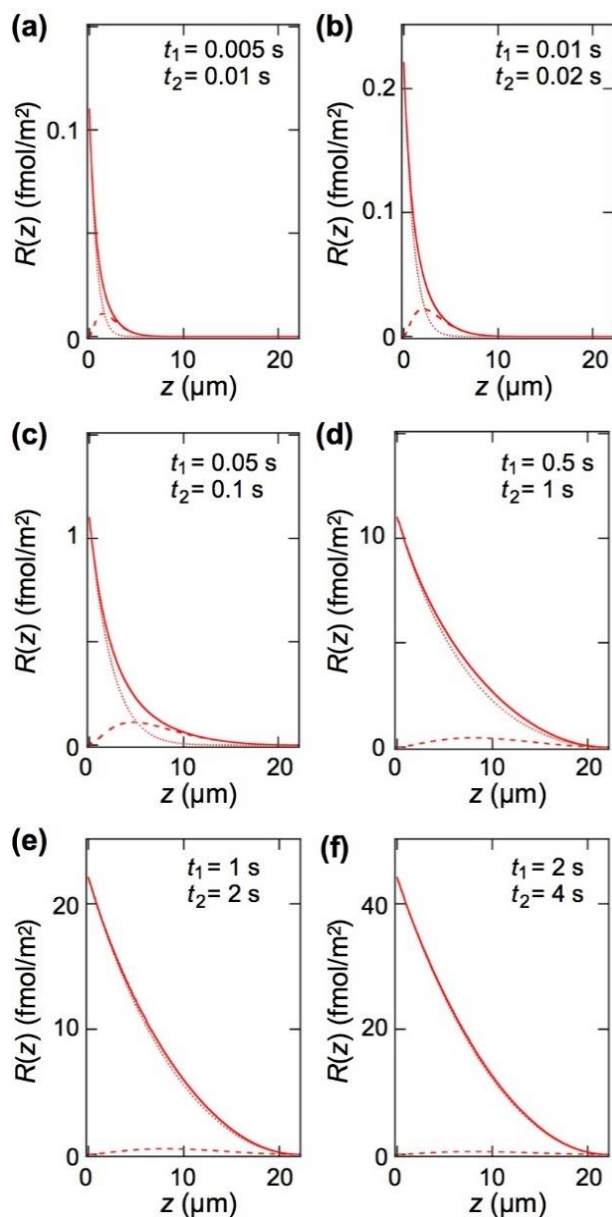


Figure 4-8: COMSOL simulation results ($d = 0$) on the effects of t_1 – t_2 conditions ($t_1 = \tau$, $t_2 = 2\tau$) on surface modification yield, $R(z)$, during the reduction step ($0 \leq t < \tau$, dotted line), during the re-oxidation step ($\tau \leq t \leq 3\tau$, dashed line), and after both the reduction and subsequent re-oxidation steps ($0 \leq t \leq 3\tau$, solid line). The data were obtained by Dr. Khanh-Hoa Tran-Ba. Reproduced with permission from reference ¹⁶⁷. Copyright 2017 American Chemical Society.

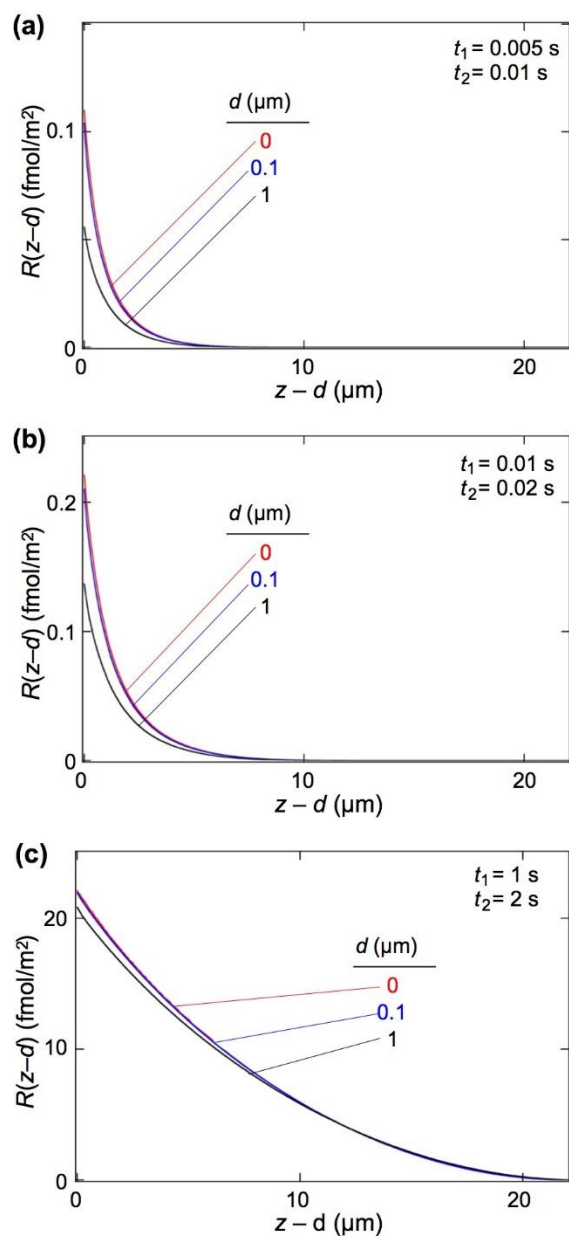


Figure 4-9: COMSOL simulation results on the effects of d on $R(z-d)$ at three different t_1-t_2 conditions. The data were obtained by Dr. Khanh-Hoa Tran-Ba. Reproduced with permission from Ref. ¹⁶⁷. Copyright 2017 American Chemical Society.

4.4 Results and Discussion

In this study, electrochemically-assisted CuAAC was examined for the longitudinally-controlled modification of ethynyl-decorated cylindrical and conical pores with azide-tagged

fluorescent dyes. Cu(I) catalysts were generated by the reduction of Cu(II) at a working electrode (WE), diffused along the long axis of a pore, and induce the CuAAC-based modification of the pore surface with azide-tagged dyes (Figure 4-1a). PET track-etched pores were chosen to demonstrate the proof-of-concept of this approach because of their fairly-defined cylindrical or conical shapes with their surface decoration capability via amidation through surface $-\text{COOH}$ groups.^{197,201} The CuAAC-based pore modification was carried out with a PET track-etched membrane sandwiched between a WE and a planar counter/reference electrode (CE/RE) (Figure 4-2a). A comb-shaped gold electrode (300 μm in width, 200 μm in spacing) was used for the modification of cylindrical pores (1 μm in diameter) to verify the contribution of electrochemically-generated Cu(I) catalysts to pore modification. A planar gold electrode was instead used as a WE for the modification of conical pores (3.5 μm in base diameter, 1 μm in tip diameter). For the pore modification, potential steps (Figure 4-2b) were applied to the WE for the reduction of Cu(II) to Cu(I) and the subsequent re-oxidation of Cu(I) to Cu(II). The length of the reduction step ($t_1 = \tau$) was changed to control the concentration and distribution of Cu(I) in the pores as well as the duration of the CuAAC reaction on the pore surfaces. The re-oxidation step ($t_2 = 2\tau$) was anticipated to terminate the CuAAC-based pore modification.

Here, the results of finite-element computer simulations will first be shown to estimate how electrochemically-generated Cu(I) catalysts control pore surface functionalization. Subsequently, the effects of τ on the spatial distribution and yield of pore modification will be discussed by assessing the fluorescence microscopy images of modified membranes. Finally, the asymmetric modification of cylindrical pores with two different dyes in opposite directions as well as the selective modification of the tip or base side of conical pores were demonstrated using the approach based on electrochemically-assisted CuAAC.

4.4.1 Finite-Element Computer Simulations

Finite-element computer simulations were used to verify how reduction step time (τ) affects the yield of CuAAC-based pore modification at different longitudinal positions, $R(z)$, in the conjunction with Cu(I) inner-pore distribution, $C_1(r,z,t)$. The simulations were carried out under several assumptions including (i) the complete reduction of Cu(II) to Cu(I) at the WE at the reduction step ($t_1 = \tau$) and the complete oxidation of Cu(I) to Cu(II) at the WE at the re-oxidation step ($t_2 = 2\tau$); (ii) the complete oxidation of Cu(I) to Cu(II) on the CE/RE at both the reduction and re-oxidation steps; (iii) a surface CuAAC reaction following the first order kinetics for azide-tagged dye and the second order kinetics for Cu(I) and surface ethynyl groups.¹⁸³ It should be noted that the simulation results could not be quantitatively compared with experimental $R(z)$ because of the uncertainty of k and Γ_0 values used for eq. 3.6. Instead, the simulation results will lead to qualitative understanding of a relationship between $C_1(r,z,t)$ and $R(z)$ and also the effects of τ on $R(z)$. The simulations were also used to assess how $R(z)$ is affected by solution-filled gaps (d in width) that are possibly formed between a membrane and two electrodes (Figures 4-6). Here, $C_1(r,z,t)$ and $R(z)$ obtained for a pore without gaps ($d = 0 \mu\text{m}$) was mainly discussed due to the relatively small influence of the gaps (*vide infra*).

Figure 4-7 shows t -dependent Cu(I) concentration profiles within the pore under different potential step conditions. Figure 4-10a summarizes those along the central axis of the pore ($r = 0$) for different reduction step times ($t_1 = \tau = 0.005 \sim 1$ sec). Cu(I) distribution was expanded from the WE ($z = 0 \mu\text{m}$) toward the CE/RE ($z = 22 \mu\text{m}$) with increasing t_1 up to 0.5 sec, and unchanged thereafter. At the longer t_1 (≥ 0.5 sec), a linear z -dependent decrease in Cu(I) concentration was obtained due to the attainment of the steady state that was defined by the boundary conditions at the WE and CE/RE (*vide supra*). On the other hand, the re-oxidation step led to a quick decrease

in Cu(I): Cu(I) was present within the pore only for a short period of time upon the re-oxidation step (≤ 0.1 sec, Figure 4-7).

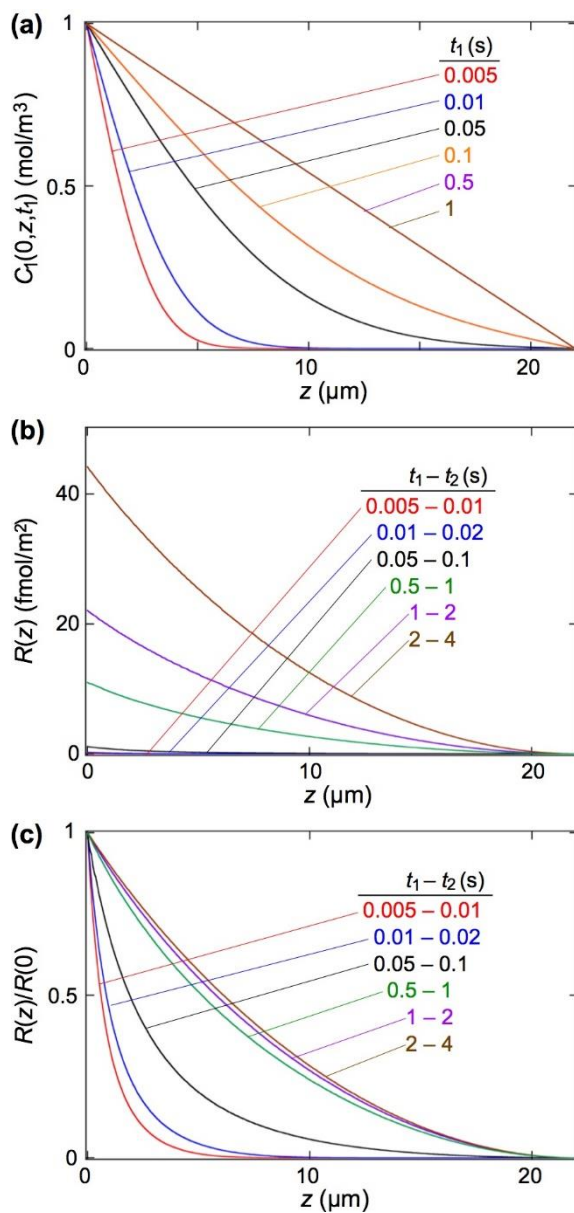


Figure 4-10: COMSOL simulation results ($d = 0$) on (a) Cu(I) concentration, $C_1(0, z, t_1)$, along the center of the pore after the reduction step ($t_1 = \tau$), (b) surface modification yield, $R(z)$, after the reduction and re-oxidation steps ($t_1 = \tau$, $t_2 = 2\tau$), and (c) normalized surface modification yield, $R(z)/R(0)$, obtained from (b). The data were obtained by Dr. Khanh-Hoa Tran-Ba. Reproduced with permission from Ref. ¹⁶⁷. Copyright 2017 American Chemical Society.

$R(z)$ profiles shown in Figure 4-10b were correlated to the corresponding Cu(I) concentration profiles (Figure 4-10a). The pore modification took place only near the WE for the short t_1 (= 0.005 sec), and expanded toward the CE/RE with increasing t_1 up to 0.5 sec. Simultaneously, the reaction yield on the pore surface adjacent to the WE, $R(0)$, increased proportionally to t_1 because of the longer reaction time (Figure 4-10b). The t_1 -dependent increase in $R(0)$ was obtained for a much longer t_1 (e.g., 1000 sec) until all the ethynyl groups on the pore surface are consumed (data not shown). Meanwhile, Cu(I) catalysts remained during the re-oxidation step gave a significant contribution to $R(z)$ only when t_1 was shorter than 0.5 sec (Figure 4-8). In contrast, the shapes of $R(z)$ profiles were very similar when $t_1 \geq 0.5$ sec, as shown in the $R(z)/R(0)$ profiles (Figure 4-10c). For the longer t_1 , $R(z)$ was primarily controlled by a steady-state, linear Cu(I) concentration profile (Figure 4-10a) with the second-order kinetics for Cu(I) in CuAAC (eq. 4.6). Due to the t_1 -dependent increase in $R(0)$ (*vide supra*), the steepness of a gradient ($R(z)/z$) increased with increasing t_1 (Figure 4-10b). On the other hand, the effects of membrane-electrode gaps were insignificant, especially for longer t_1 , due to the relatively fast diffusion of Cu(I), as shown by the similar $R(z)$ profiles at $d = 0, 0.1$ and $1 \mu\text{m}$ (Figure 4-9).

These simulation results lead to the following conclusions. First, the application of a very short reduction step ($\tau \leq 0.01$ sec) enables pore modification only near the WE. Unfortunately, we could not experimentally verify such localized modification because of the limited sensitivity of the fluorescence microscopy measurements under the examined condition (data not shown). Multiple potential steps for short τ should be applied for experimental observation of such short-distance modification. Second, application of a relatively long reduction step ($\tau \geq 0.5$ sec) will lead to longitudinal gradient modification with a higher yield for longer τ . The τ -dependence of modification yield and the steepness of a gradient could be assessed from fluorescence microscopy

images of modified membranes. The next section will discuss experimental results regarding the effects of τ on the CuAAC-based modification of cylindrical pores (1 μm in diameter).

4.4.2 Effects of Reduction Step Time on Cylindrical Pore Modification

The effects of τ on pore modification were investigated by measuring the planar and cross-sectional fluorescence microscopy images of PET track-etched membranes comprising cylindrical pores (1 μm in diameter). It should be noted that membranes modified for $\tau < 10$ sec could not be discussed due to the limited sensitivity of the CCD camera used in this study.

Figure 4-11a shows typical planar images of membranes modified for different τ . The width of the darker band was similar to the inter-teeth spacing (*ca.* 200 μm) of the comb-shaped WE, indicating selective modification above the electrode teeth. The fluorescence intensity of modified areas increased from 10 sec to 360 sec, and then did not significantly change up to 1000 sec, as shown by the fluorescence intensity profiles in the insets (Figure 4-11a) and the τ -dependence of the fluorescence intensity (Figure 4-11b). The τ -dependent increase in fluorescence intensity was anticipated from the simulation results that showed CuAAC-based pore modification controlled by Cu(I) catalysts generated at a WE (*vide supra*). On the other hand, the insignificant modification at the longer τ could result from the reaction of all the surface ethynyl groups, which was possible if the rate constant for CuAAC on the surface was much larger than that used in the simulations.¹⁸⁰

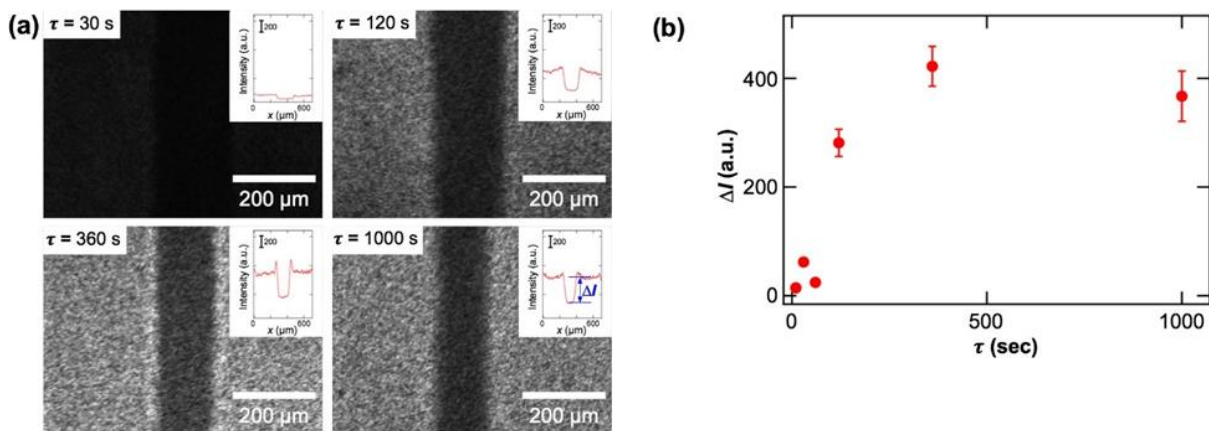


Figure 4-11: (a) Typical planar fluorescence images of PET track-etched membranes (1 μm in cylindrical pore diameter) modified with Azide-fluor 545 for $\tau = 30$ sec, $\tau = 120$ sec, $\tau = 360$ sec and $\tau = 1000$ sec. Recorded using a 10x objective lens with a TRITC filter set for the same integration time (5 sec) in the same day. The inset shows a typical fluorescence intensity profile across the inter-electrode region obtained from each planar image. The definition of ΔI is given in the intensity profile for $\tau = 1000$ sec. (b) τ -dependence of ΔI (average \pm 95% confidence interval) obtained from 11-22 different pairs of modified-unmodified regions in a membrane. The low ΔI at $\tau = 60$ sec might be due to the insufficient removal of air between the membrane and WE. Reproduced with permission from Ref. ¹⁶⁷. Copyright 2017 American Chemical Society.

Figure 4-13a shows typical cross-sectional images of membranes modified for different τ . A brighter region in each of the images corresponds to a modified region where a tooth of the comb-shaped electrode was located during the modification. Interestingly, the modification was not uniform across the membranes. Figure 4-13b depicts cross-sectional profiles obtained from the images shown in Figure 4-13a. In contrast to the symmetric profiles for the darker, unmodified regions, the brighter regions exhibited asymmetric gradient profiles with higher fluorescence intensity near the WE. Slight pore modification near the CE/RE (Figure 4-13) in contrast to the simulation results (Figure 4-10) could be due to the involvement of convection or the insufficient control of the CE/RE potential. Such an asymmetric profile was not obtained with CuAAC-based modification of cylindrical PET track-etched pores in a homogeneous solution containing Cu(I) catalysts produced from Cu(II) by L-ascorbic acid (Figure 4-12). Thus, it can be concluded that

the gradient was formed as a result of pore modification controlled by the longitudinal distribution of Cu(I) catalysts generated at the WE (Figure 4-1a).

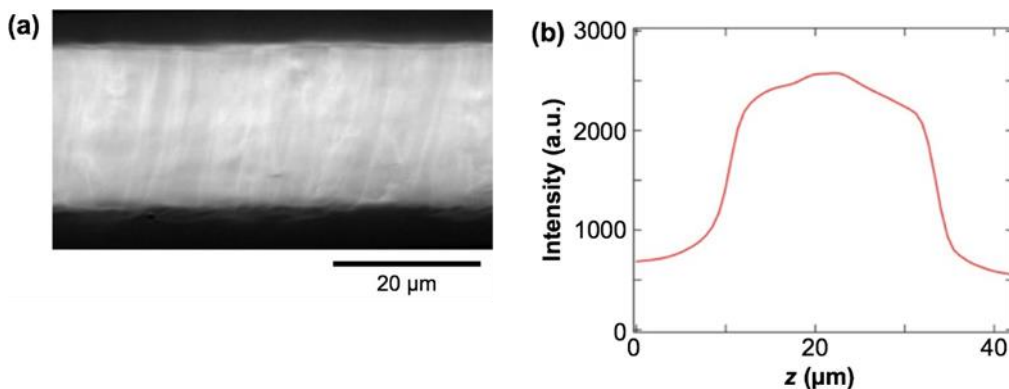


Figure 4-12: (a) A typical cross-sectional fluorescence image of a PET track-etched membrane (1 μm in cylindrical pore diameter, *ca.* 22 μm thick) modified with Azide-fluor 545 from a homogeneous solution for 1000 sec. Cu(I) was generated via the reduction of Cu(II) by L-ascorbic acid. Recorded using a 100x oil immersion objective lens and a TRITC filter set. (b) An averaged cross-sectional profile obtained from (a). Reproduced with permission from Ref. ¹⁶⁷. Copyright 2017 American Chemical Society.

Indeed, τ -dependent increases in gradient slope (Figure 4-13c) and fluorescence intensity, I_{\max} , (Figure 4-13d) were qualitatively consistent to the trends obtained with the finite-element computer simulations. The smaller increase in slope and I_{\max} for $\tau > 360$ sec were consistent to the τ -dependence in the horizontal images (Figure 4-11b). These results indicate that asymmetric gradient modification across a porous membrane is possible by taking advantage of electrochemically-assisted CuAAC.

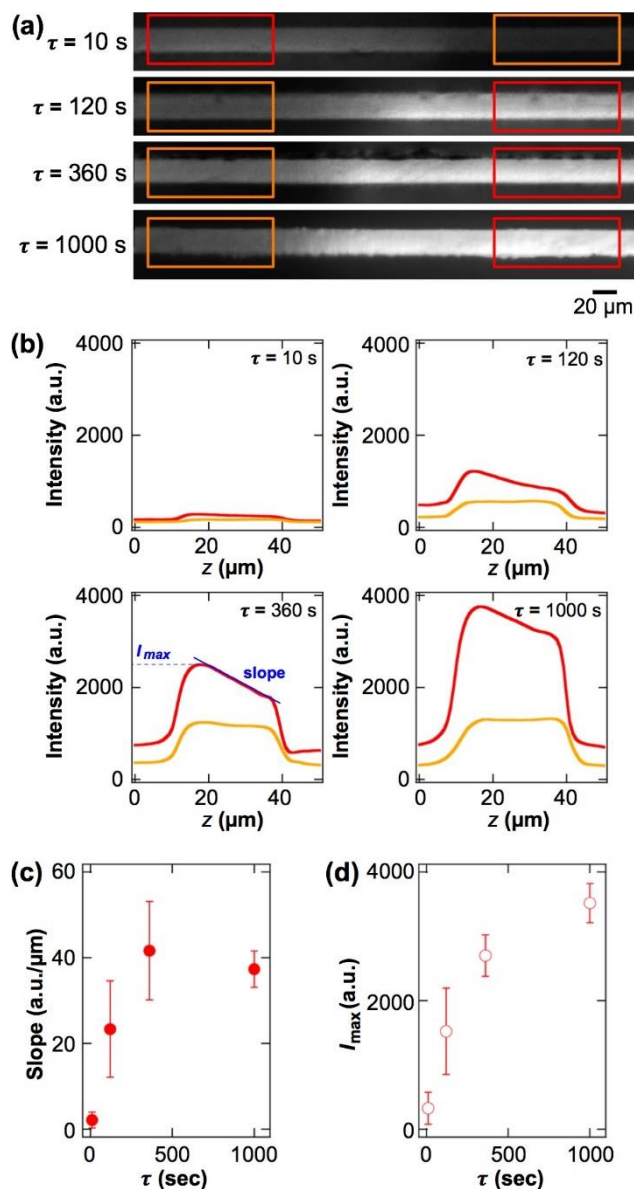


Figure 4-13: (a) Typical cross-sectional fluorescence images of PET track-etched membranes ($1 \mu\text{m}$ in cylindrical pore diameter, *ca.* $22 \mu\text{m}$ thick) modified with Azide-fluor 545 for $\tau = 10$ sec, $\tau = 120$ sec, $\tau = 360$ sec and $\tau = 1000$ sec. The bottom side in each image was in contact to a comb-shaped electrode during CuAAC. Recorded using a $10\times$ objective lens with a TRITC filter set for the same integration time (1 sec) in the same day. (b) Cross-sectional fluorescence intensity profile across each membrane shown in (a). The red and orange profiles, reflecting electrode-contact and inter-electrode regions during CuAAC, respectively, were obtained by averaging the profiles in the regions shown by squares in (a). The definitions of fluorescence intensity slope and I_{max} are given in the inset for $\tau = 360$ sec. (c) τ -dependence of fluorescence intensity slope (average $\pm 95\%$ confidence interval) obtained from modified regions in a membrane by 4-9 different electrode teeth. (d) τ -dependence of I_{max} (average $\pm 95\%$ confidence interval) obtained from modified regions in a membrane by 4-9 different electrode teeth. Reproduced with permission from Ref. ¹⁶⁷. Copyright 2017 American Chemical Society.

4.4.3 Asymmetric Modification with Two Fluorescent Dyes in Opposite Directions

The electrochemically-controlled approach provides a means for the gradient modification of pores with two different species in the opposite directions. Figure 4-14a shows planar images of a PET track-etched membrane with cylindrical pores (1 μm in diameter) that was first modified with Azide-fluor 545 from one side, and then with Azide-fluor 488 from the other. These images were recorded using a 100x oil immersion lens instead of a 10x objective lens. The upper and lower images were obtained on membrane surfaces that were placed in proximity to a WE during the modification with Azide-fluor 545 and Azide-fluor 488, respectively. The left and right images were recorded at the same sample region using FITC ($\lambda_{\text{ex}} = 470 \pm 20 \text{ nm}$; $\lambda_{\text{em}} = 535 \pm 20 \text{ nm}$) and TRITC ($\lambda_{\text{ex}} = 542 \pm 10 \text{ nm}$; $\lambda_{\text{em}} = 620 \pm 26 \text{ nm}$) filter sets that were suitable for the fluorescence measurements of Azide-fluor 488 and Azide-fluor 545, respectively. These images exhibited ring-shaped patterns with a diameter of *ca.* 1 μm that corresponded to dye-modified cylindrical pores. Importantly, images obtained with the FITC and TRITC filter sets showed more distinct ring-shaped patterns on the surfaces modified with Azide-fluor 488 (lower left) and Azide-fluor 545 (upper right), respectively. These results reflected the more efficient pore modification in proximity to the WE during electrochemically-assisted CuAAC.

The asymmetric pore modification with the two dyes was further verified from the cross-sectional fluorescence images and profiles of the membrane. Figure 4-14b shows cross-sectional images recorded using the FITC and TRITC filter sets at an identical region. These images reveal asymmetric modification with the two dyes in the opposite directions, as anticipated from the planar images (Figure 4-14a). The cross-sectional fluorescence intensity profiles (Figure 4-14c)

revealed the gradient modification of the two dyes in the opposite directions. These results indicate the success of the two-step asymmetric gradient modification across a porous membrane.

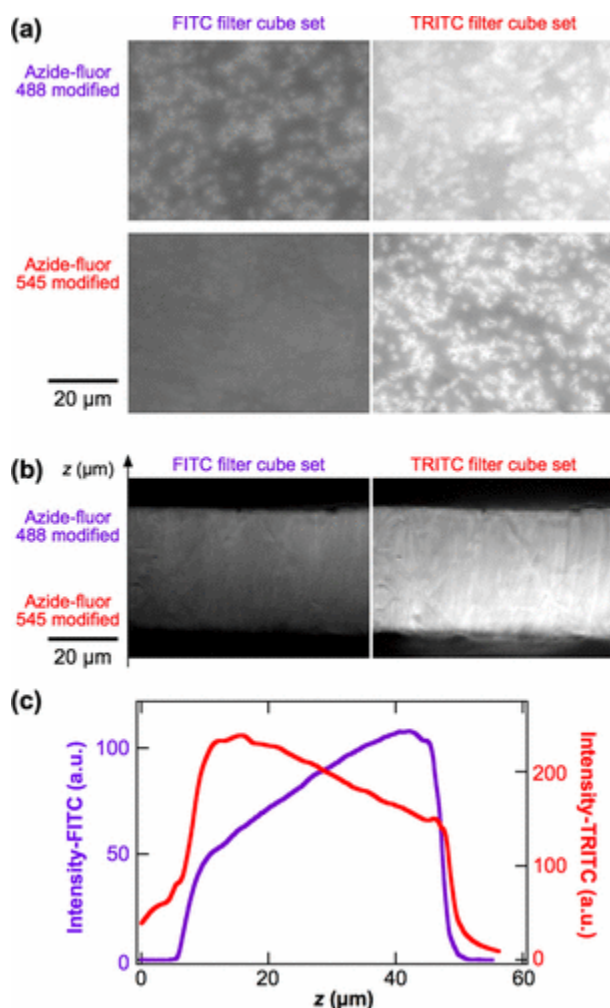


Figure 4-14: (a) Typical planar fluorescence images of a PET track-etched membrane (1 μm in cylindrical pore diameter, *ca.* 22 μm thick) modified with Azide-fluor 545 for $\tau = 30$ sec, followed by Azide-fluor 488 for $\tau = 30$ sec. The upper two images and the bottom two images were recorded at the same areas through the FITC (left) and TRITC (right) filter sets. Recorded using a 100x oil immersion objective lens for the same integration time (1 sec). (b) Cross-sectional fluorescence images of the PET track-etched membrane recorded at the same area using the FITC (left) and TRITC (right) filter sets. The upper and bottom faces were in contact to a comb-shaped electrode during the modification with Azide-fluor 545 and Azide-fluor 488, respectively. Recorded using a 100x oil immersion objective lens for the same integration time (0.5 sec). (c) Averaged cross-sectional fluorescence intensity profiles across the membrane shown in (b). Reproduced with permission from Ref. ¹⁶⁷. Copyright 2017 American Chemical Society.

4.4.4 Asymmetric Modification of Conical Pores

The asymmetric pore modification based on electrochemically-assisted CuAAC provided a means to selectively visualize the base and tip openings of a conical PET track-etched pore. Figure 4-15a shows base-side (left) and cross-sectional (right) SEM images of a PET track-etched membrane with conical pores that was used in this study. The former can be used to measure the base-side pore diameter of $3.3 \pm 0.4 \mu\text{m}$, and the latter reveals the conical pore shapes with the tip-side diameters of *ca.* $1 \mu\text{m}$. The membrane (*ca.* $1 \times 1 \text{ cm}^2$) was cut to half, and the resulting two pieces were used for the asymmetric pore modification with Azide-fluor 545 from the base or tip side (Figure 4-15b). Figure 4-15c shows planar fluorescence (left) and optical transmission (right) images recorded at the same areas of the membrane pieces modified from the base side (upper) and the tip side (lower). Ring- or dot-shaped patterns in the fluorescence images were observed at the positions where pores were found in the optical transmission images. Importantly, the base-side modification afforded ring-shaped patterns with a diameter of $3.5 \pm 0.5 \mu\text{m}$ (Figure 4-15c, left), which was close to that obtained from the SEM image (Figure 4-15a, left). In contrast, the tip-side modification offered significantly smaller ring-shaped patterns with a diameter of $1.2 \pm 0.4 \mu\text{m}$ or dot-shaped patterns. The dot-shaped patterns were possibly obtained from tip openings with radii close to or smaller than the diffraction-limited resolution ($\sim 0.29 \mu\text{m}$ for $\text{NA} = 1.30$ at 620 nm). These results indicate that the reported approach based on electrochemically-assisted CuAAC provides a simple means to characterize conical pores based on its capability to asymmetrically modify the membrane surfaces.

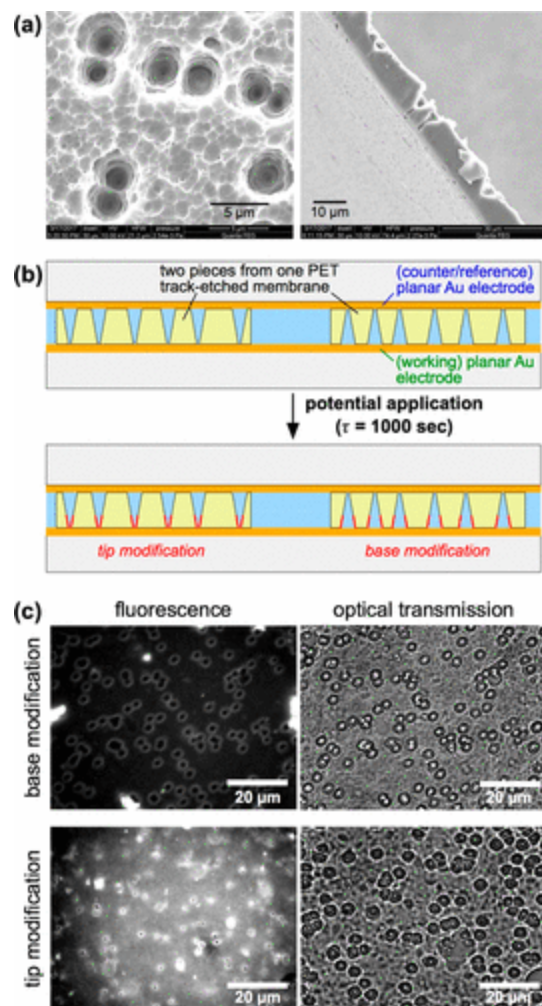


Figure 4-15: (a) SEM images of a PET track-etched membrane with conical pores. (left) Base-side surface image; (right) cross-sectional image. The TEM images were obtained by Natasha Siepser and Prof. Lane A. Baker. (b) Schematic illustration on electrochemically-controlled modification of PET track-etched conical pores with Azide-fluor 545 via CuAAC. Two pieces of membranes (*ca.* 0.5 x 1 cm²) were obtained by cutting a large membrane (*ca.* 1 x 1 cm²). One of them was modified from the tip side, and the other was modified from the base side. (c) Planar fluorescence (left) and optical transmission (right) images recorded at the same areas of PET track-etched membranes with conical pores modified from the base side (upper) and the tip side (lower) for $\tau = 1000$ sec. Recorded using a 100x oil immersion objective lens with a TRITC filter set for the same integration time (15 sec for the fluorescence images; 0.5 sec for the optical images). Reproduced with permission from Ref. ¹⁶⁷. Copyright 2017 American Chemical Society.

4.4.5 Further Control of the Pore Modification

The control of pore modification with electrochemically-assisted CuAAC was not as good as that expected from the simulation results (Figure 4-10), as shown by the wider modification

length and by the modification near the CE/RE (Figure 4-13b). These results could be due to the involvement of convection or the insufficient control of the CE/RE potential. The following two experiments were performed for better control of the modification length of cylindrical PET track-etched membrane pores. Unfortunately, these experiments did not give a positive outcome.

The first approach is the use of a chemical species that oxidizes the Cu(I) complex to modify pores only near the RE. H₂O₂ was selected as the oxidizing agent because its standard reduction potential seems to be sufficiently positive ($E^0 = +1.8$ V for $\text{H}_2\text{O}_2 + 2\text{H}^+ + 2\text{e}^- \rightleftharpoons 2\text{H}_2\text{O}$) as compared with that for Cu(II)/(I) (-0.15 V). In addition, H₂O₂ and its reduced product (H₂O) is unlikely to react with other species in the solution. Pore modification with electrochemically-assisted CuAAC was examined in the presence of 20–80 mM H₂O₂. Figure 4-16a shows the CV obtained in a H₂O/DMSO (1:1) solution containing 1 mM CuSO₄, 1 mM TBTA and 0.1 M NaBF₄ with and without H₂O₂. The addition of H₂O₂ suppressed the reduction of Cu(II), which was more significant at the higher H₂O₂ concentration. Figure 4-16b shows the planar and cross-sectional fluorescence images of PET track-etched membranes (1 μm in pore diameter) modified in the presence of H₂O₂ of different concentrations. The addition of H₂O₂ significantly suppressed the pore modification with Azide-fluor 545 via click reaction, but the suppression seemed to occur along the entire pores. This means that the addition of H₂O₂ inhibited the pore modification significantly, but did not clearly help localize pore modification in the proximity of the RE.

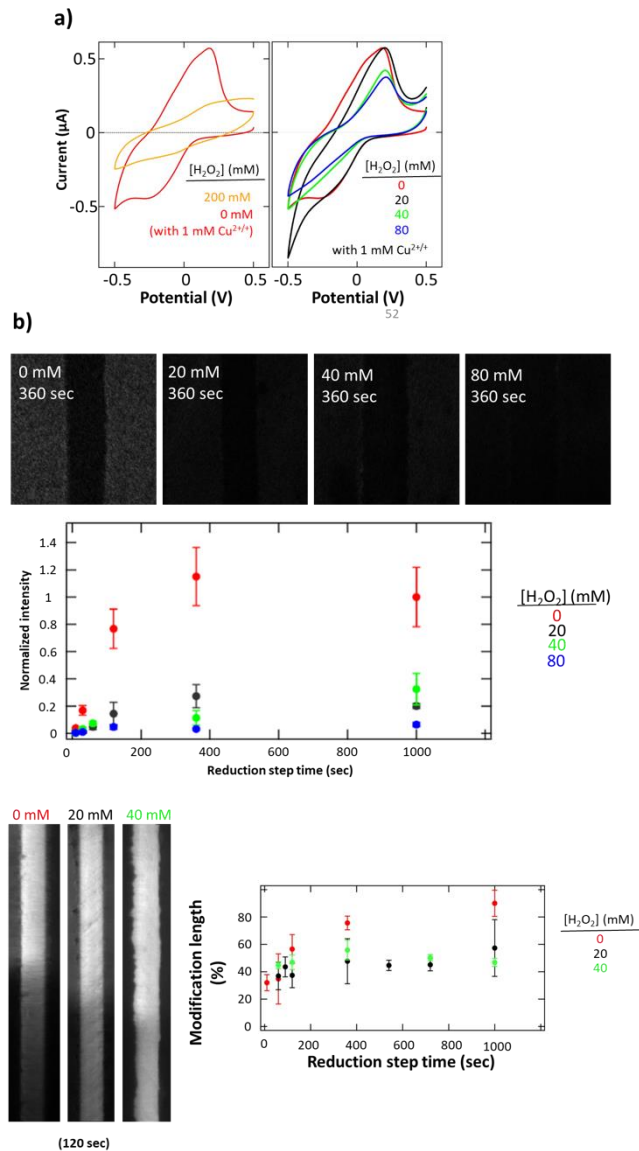


Figure 4-16: (a) CV obtained in a $\text{H}_2\text{O}/\text{DMSO}$ (1:1) solution containing 1 mM CuSO_4 , 1 mM TBTA and 0.1 M NaBF_4 with and without H_2O_2 . (b) Planar and cross section analysis of the modification of the membrane modified with Azide-fluor 545 in the presence and absence of H_2O_2 .

Another approach was the multiple application of short potential steps, as shown in Figure 4-17, for functionalization in the proximity of the underlying electrode. The application of a short reduction potential step was expected to achieve shorter modification length, as suggested by the result shown in Figure 4-10c. Multiple potential steps were applied to increase the amount of

fluorescent dyes immobilized onto the pore surface, giving higher fluorescence intensity. I tried to functionalize cylindrical pores by applying ≤ 50 potential steps for different durations of a potential application ($\Delta\tau$) as short as 0.05 sec. However, I could not show the functionalization of the pore surface, probably because the total duration ($= 0.05 \text{ sec} \times 50 \text{ steps} = 2.5 \text{ sec}$) was not long enough to immobilize a sufficient number of fluorescent dyes for fluorescence detection by the microscope used in this study.

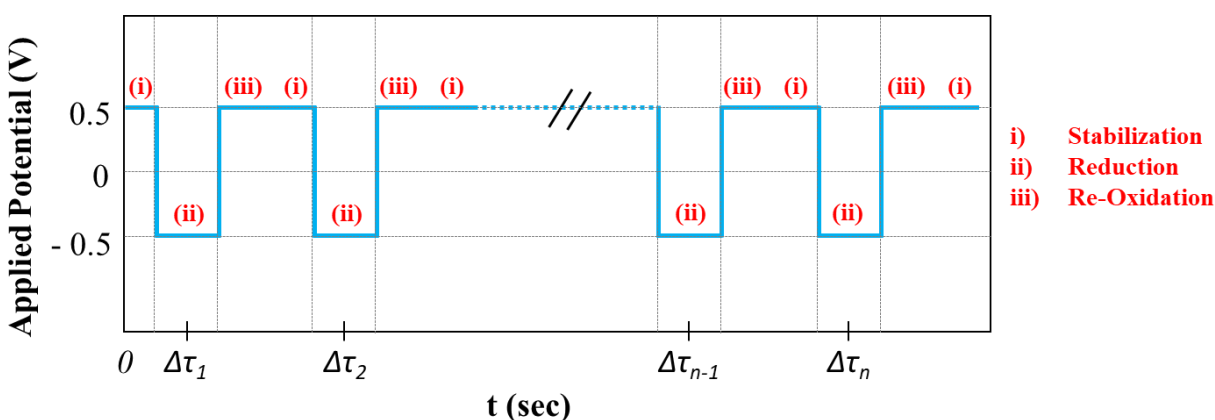


Figure 4-17: Potential steps examined to achieve better control of the modification length.

4.5 Conclusions

This chapter reports longitudinally-controlled, asymmetric pore modification using electrochemically-assisted CuAAC. Cu(I) catalysts were produced by the reduction of Cu(II) at an underlying WE to control the modification of ethynyl-decorated PET track-etched pores with azide-tagged fluorescent dyes. Fluorescence microscopy images revealed gradient modification along the pore axis together with a τ -dependent increase in modification yield, which reflected the distribution of Cu(I) catalysts inside the pores. The results of finite-element computer simulations qualitatively supported these experimental observations, and also showed a possibility to modify a narrower region in proximity to the WE by applying short potential steps ($\leq 0.01 \text{ sec}$). The

electrochemically-controlled approach enabled asymmetric modification of cylindrical pores with two different dyes in the opposite directions and also the selective modification around the base or tip side of conical pores. It should be pointed out that this method is applicable for the longitudinally-controlled modification of smaller, nanoscale pores regardless of their shapes. In the future, this electrochemical approach will be used for sequential pore modification with multiple species to design porous membranes for chemical separations and sequential catalytic reactors.

5. Unique Swelling Properties of PS-*b*-PEO Thin Films

5.1 Contribution of Authors

TI directed the overall project. HC prepared all the samples and did all the ellipsometry and microscopic measurements. Analysis of the data was done by HC using LabView software developed by DAH.

5.2 Introduction

Diblock copolymers (DBC) have emerged as unique materials for the fabrication of well-organized functional structures on the nanometer scale. Nanostructures formed from DBCs result from a self-assembly process, called microphase separation, that occurs due to the distinct chemical nature of each of the polymer blocks.¹¹⁷ The morphology of the nanostructures (microdomains) can be spherical, gyroid, cylindrical or lamellar, depending on the volume fractions of the polymer chains in a DBC. The size of microdomains is defined by the polymer molecular weight.²⁰³ The orientation of cylindrical and lamellar microdomains is often controlled by interactions for each of the polymer blocks at the air-film and substrate-film interfaces.²⁰⁴ With the control of these parameters, DBCs have been used for various applications such as templating, separations, catalysis and sensors.²⁰⁵

Albalak et. al.²⁰⁶ and Kim G et.al.¹⁴¹ reported that the order and orientation of DBC microdomains could be improved by exposing DBC monoliths to a solvent vapor. Importantly, this method, called solvent vapor annealing (SVA), shows the improvement of microdomain structures more quickly than thermal annealing. During SVA, microdomains change from a non-equilibrium morphology entrapped by rapid solvent evaporation during spin-coating, to the

equilibrium morphology of a solvent swollen DBC. Later, Russel et. al.¹⁴³ demonstrated that SVA led to improved microdomain organization with orientation controlled by the solvent evaporation for thin PS-*b*-PEO films. This strategy could also induce the morphological transformation of the microdomains from cylindrical horizontally oriented domains into a permeable porous structure comprised of vertically oriented domains that can be used for water filtration purposes or as new templates for material science.²⁰⁷ PS-*b*-PEO monoliths with porous morphologies in PS architectural structures were applicable as separation membranes,²⁰⁸ by taking advantage of the hydrophilic antifouling properties of PEO chains on pore surfaces.^{209,210}

Polymer swelling involves the relaxation of the polymeric chains induced by solvent penetration.^{211,212} The presence of a penetrant solvent can change significantly the physical properties of the polymer. This ability to change volume when exposed to an appropriate solvent can be used in technological application such as protein separation,²⁰⁸ sensors²¹³ and microelectronics.²¹⁴ Gensel et. al. reported that chloroform uptake led to a 10% increase in film thickness for cylinder-forming polystyrene-*block*-polybutadiene when the film thickness was close to the domain size.²¹⁵ Tsarkova et al. found that the swelling of a thin film of cylinder forming PS-*b*-PB was not homogeneous, and swelling was larger closer to the film interface.²¹⁶

The swelling of a thin polymer film is commonly measured by X-ray or neutron reflectivity,²¹⁷⁻²¹⁹ grazing incidence small-angle X-Ray scattering (GISAXS),²²⁰ quartz crystal microbalance (QCM)²²¹ or spectroscopic ellipsometry (SE).^{222,223} Among them, SE is a simple and non-invasive method that can simultaneously measure the thickness and optical properties such as refractive index of a polymer film.²²⁴ However, SE gives averaged information from a relatively wide (mm scale) sample area, and cannot provide more detailed information about the swelling behavior of nanoscale structures such as DBC microdomains.

Many efforts have been made to unveil the domain structure and molecular diffusion behavior inside DBC microdomains,^{51,225} but a very limited number of papers reported how solvent-induced swelling affects these properties of DBC microdomains.²²⁶ Fluorescence microscopy can be used to extract information on each of the microdomains by choosing the right fluorescent probe dyes that selectively partition to one of the DBC microdomains.⁶²

The diffusion coefficient inside cylindrical PEO microdomains in PS-*b*-PEO films was investigated previously in Dr. Ito's lab under different conditions.^{43,51,98} Interestingly, these studies have shown that fluorescence microscopy can be used to measure the shape and transverse width of a microdomain in a thin PS-*b*-PEO film,⁹⁶ in addition to microdomain permeability.⁹⁸ However, these previous studies mainly focused on investigating the effects of the deswelling of PS-*b*-PEO films prepared from its solutions in benzene and tetrahydrofuran, which are good solvents for both PS and PEO, on diffusion of fluorescent small molecules. In contrast, the swelling of DBC microdomains by the exposure to the vapors of poor solvents for either or both of the polymer fragments (*i.e.*, water or ethanol) was not investigated in detail, even though the addition of water was shown to improve microdomain orientation in SVA.^{143,204}

In this work, we investigated changes in the properties of PS-*b*-PEO thin films upon exposure to water and ethanol vapor. We measured film thickness, environment polarity, and molecular permeability of thin films of PS-*b*-PEO having two different molecular weights with a very similar PEO volume fraction (0.22) using SE and a series of fluorescence methods. We compared the results of the PS-*b*-PEO films with those of thin films of PS homopolymer (hPS) and PEO homopolymers with two different molecular weights (hPEO). We verified that PEO microdomains in thin PS-*b*-PEO films could be swollen by ethanol, in contrast to hPS and hPEO

films. The unique swelling behavior of the PEO microdomains possibly reflects the poorer packing of PEO chains controlled by the nanostructured PS framework.

5.3 Experimental Procedure

5.3.1 Chemicals and Materials

Poly(ethylene glycol) methyl ether (hPEO₁₂, $M_n = 12,000$ g/mol; hPEO_{3.8}, $M_n = 3,800$ g/mol), polystyrene (hPS_{16.4}, $M_n = 45,000$ g/mol), PS_{15.5-*b*-PEO₄ ($M_n = 15,500$ g/mol for PS and $M_n = 4,000$ g/mol for PEO) and PS_{35-*b*-PEO_{10.5} ($M_n = 35,000$ g/mol for PS and $M_n = 10,500$ g/mol for PEO) were obtained from Polymer Source and used as received. Nile red (NR) and sulforhodamine B (SRB) were obtained from Aldrich and Acros Organics respectively and used without further purification. These dyes were dissolved in HPLC/spectrophotometric grade ethanol (Sigma-Aldrich®) to prepare stock solutions. HPLC grade toluene (Fisher Chemicals®) was used for preparation of polymer solutions for spin coating. Ultrapure water (18 MΩ/cm) and anhydrous ethanol (USP specs, Decon Laboratories inc.) were bubbled by N₂ which carries the water and ethanol vapor used to expose the thin films for spectroscopic ellipsometry and fluorescence microscopy measurements. Glass coverslip (FisherFinest® Premium; 25 x 25 mm², 0.2 mm thick) were employed as the substrate for SMT and FCS experiments. Si (100) wafers (p-type) were purchased from University Wafer and cut to 1 x 1 cm² substrate for ellipsometry experiments.}}

5.3.2 Sample Preparation

Substrates employed in these studies were cleaned by rinsing with ultrapure water and exposing to an air plasma for 5 min. A thin film of a polymer (20-200 nm thick) was prepared by

spin casting a toluene solution of the polymer containing an appropriate dye on the substrate. Polymer films used for two-color ensemble and single-molecule measurements contained 100 nM and 10 nM NR, in separate experiments. The concentrations of SRB in thin films used for SMT and FCS measurements were 0.4 nM and 10 nM, respectively. These fluorescence measurements were carried out for films with thicknesses around 100 nm. Polymer films were stabilized under a N₂ flow for 4-5 minutes prior to each measurement, and then exposed to N₂ saturated with water or ethanol that was obtained by bubbling N₂ through the corresponding pure solvent.

5.3.3 FCS Measurements

FCS measurements for SRB molecules in polymer thin films were carried out using a sample scanning fluorescence microscope. A film sample was mounted on a piezoelectric stage that was attached to an inverted, epi-illumination microscope (modified-Nikon). A beam (532 nm, 4 μ W) emitted by a Nd:YVO₄ laser (Verdi V series) was introduced to the back aperture of an oil-immersion objective lens (Nikon 100X; 1.3NA) to produce a nearly diffraction-limited focused laser spot (\approx 300 nm in diameter) on the sample. Fluorescence emitted by SRB molecules was collected by the same objective lens, passed through a long pass filter (532 nm dichroic mirror) and an appropriate notch filter (Kaiser Optical), and detected by a single photon counting avalanche photo diode (APD) from EG&G Optoelectronic Components. The APD detector was positioned in a secondary image plane of the microscope to record a time-dependent, spectrally-integrated, fluorescence signal from the observation volume. The observation volume was calibrated according to a procedure reported by Hou et. al.⁴¹

5.3.4 SMT Measurements

All SMT data were recorded on a wide-field fluorescence microscope. The microscope was built on an inverted epi-illumination setup (Nikon Eclipse Ti). Light emitted by an argon ion laser (Coherent Sapphire LP; 514 nm; 3 mW) was introduced to the back aperture of an oil-immersion objective (Nikon Apo TIRF 100X; 1.49NA) by reflection from a dichroic beam splitter (Chroma, 555 DCLP). Emitted fluorescence was collected by the objective, directed through the dichroic mirror and a bandpass-filter (Chroma 580/40 HQ), and then detected using a back-illuminated electron-multiplying, thermoelectrically-cooled CCD camera (EM-CCD camera; Andor iXon DU-897). All SMT videos were recorded with an electron multiplying gain of 30. Regions of the sample $32 \times 32 \mu\text{m}^2$ in size were collected a 256 pixel x 256 pixel image at 2 x 2 binning (1 pixel = 125 nm). The videos acquired were 200 frames in length, and recorded at 0.1 sec as a cycle time, and a readout rate of 10 MHz. SMT data was analyzed by generating single-molecule trajectories according to a procedure in Chapter 2. Detection of fluorescent spots in each frame of the video and consecutive spot linking to create a trajectory were accomplished using Dr. Higgins' Labview software or manually.

5.3.5 Ellipsometry Measurements

All ellipsometry data for thin films of hPEO_{3.8}, hPEO_{12.5}, hPS₄₅, PS_{13.5}-*b*-PEO₄ and PS₃₅-*b*-PEO_{10.5} were recorded by a spectroscopic ellipsometer (J.A. Woollam Alpha-SE). The thickness and refractive index of a polymer film were simultaneously recorded as a function of time. Figure 5-1 shows an experimental setup that was used to continuously monitor the two parameters under dry N₂, ethanol-saturated N₂ (ethanol vapor) and water-saturated N₂ (water vapor). An increase in film thickness (thickness gain) was calculated from thickness values obtained for 3 minutes after

stabilization of the atmosphere and thickness signal. A detailed procedure for the ellipsometry measurements is explained in Appendix A.

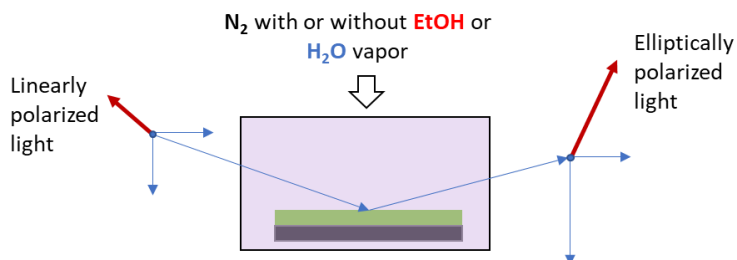


Figure 5-1: Experimental setup for spectroscopic ellipsometry measurements of polymer thin films under controlled atmosphere.

5.3.6 Two-Color Imaging.

All data was collected using the invert epi-illumination setup (Nikon Eclipse Ti) according to a procedure reported by Giri et al.⁴⁵ NR molecules were excited by a laser at 514 nm (Sapphire Coherent). Fluorescence emitted by the NR molecules was passed through a dichroic beam splitter (555 DLCP) and through a 550 nm colored-glass long-pass filter, divided into two image channels centered at 580 and 625 nm using an image splitter (Cairn Research OptoSplit II) incorporating a second dichroic beam splitter (Chroma 610, DLCP) with appropriate bandpass filters (625 ± 20 nm and 580 ± 20 nm). Fluorescence in these two channels was simultaneously detected using an EM-CCD camera (Andor iXon DU-897). Images were recorded several times at different positions of the films for each vapor condition. Each image was collected for a $32 \times 32 \mu\text{m}^2$ film region as 512 pixels \times 512 pixels at 1×1 binning (1 pixel = 62.5 nm).

5.3.6.1 Two-Color Ensemble Imaging

Two-color ensemble images were recorded for polymer films containing 100 nM NR (~100 nm thick) with an exposure time of 1 sec. Images were analyzed by cropping ≈ 80 pixels² from each band. ImageJ software²²⁷ was used to measure the average fluorescence intensity of the cropped region. The intensity was later used to calculate an E_{ensemble} value for each polymer thin film under each vapor condition.

5.3.6.2 Two-Color Single-Molecule Imaging

Two-color single-molecule images were obtained for polymer films containing 10 nM NR (~100 nm thick) with an exposure time of 5 sec. The images were analyzed using software written by Dr. Higgins, in a LabView programming environment. This software permitted for dividing the original image into two images, each one from each individual spectral channel (625 ± 20 nm and 580 ± 20 nm), and then allowed the adjustment of the tilts of the images for matching the positions of individual molecules in the two images. The software searches, fits (with a 2D Gaussian function), and gives fluorescence intensity values of each molecule in the two images. An E_{SM} value was calculated from the fluorescence intensity values of each molecule.

5.3.7 Fluorescence Spectroscopic Measurements for Thin Films

The fluorescence spectra of 100-nm thick films used for the two-color imaging were recorded using a 0.3 m imaging spectrograph (Acton Research) equipped with a thermoelectrically-cooled CCD camera/detector (Andor Newton). The integration time of the measurements was 10 seconds. Calibration of the wavelength axis was done using known emission peaks emitted by a Ne lamp.

5.4 Results and Discussion

5.4.1 AFM Images

Figure 5-2 shows typical AFM topographic images of 100 nm thick films of PS_{15.5}-*b*-PEO₄ and PS₃₅-*b*-PEO_{10.5}. These images show “fingerprint” structures that were possibly formed from horizontally-oriented cylindrical microdomains. PEO microdomains appeared with darker contrast.⁹⁸ The width of PEO microdomains were larger for PS₃₅-*b*-PEO_{10.5} (15.3 ± 2.1 nm, averaged from 10 domains) than PS_{15.5}-*b*-PEO₄ (12.5 ± 1.8 nm averaged from 10 domains), as qualitatively expected from the larger molecular weight of the former. In addition, Figure 5-2 shows the surface morphology of these films did not significantly change upon exposure to ethanol or water vapor, though several pits were formed on a water-exposed PS_{15.5}-*b*-PEO₄ film (Figure 5-2, left bottom). Upon vapor exposure, the microdomain size did not change for PS₃₅-*b*-PEO_{10.5} films, whereas the microdomains seemed to be a little larger for PS_{15.5}-*b*-PEO₄ films. These results suggest that the PEO microdomains were retained upon exposure to ethanol or water vapor.

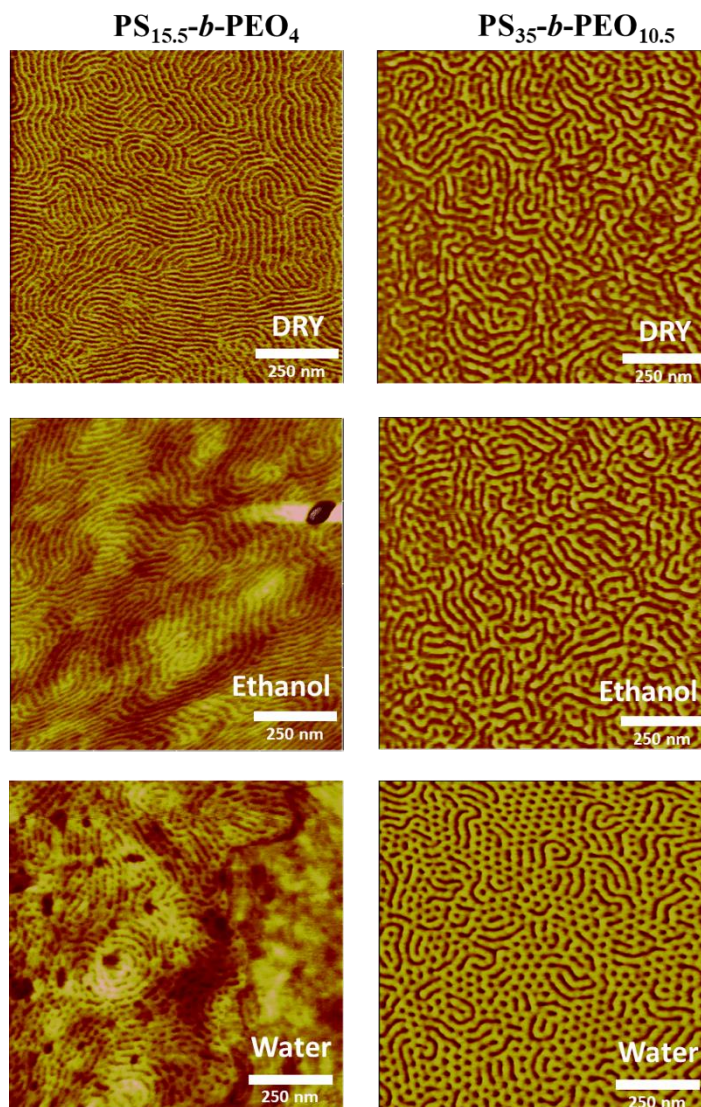


Figure 5-2: (a) Typical AFM topographic images of three different dried thin films of $PS_{15.5}\text{-}b\text{-}PEO_4$ and $PS_{35}\text{-}b\text{-}PEO_{10.5}$ before exposure to ethanol/water vapor (top), after exposure to ethanol vapor (middle) and after exposure to water vapor (bottom). Film thickness = 106 nm ($PS_{15.5}\text{-}b\text{-}PEO_4$.) and 118 nm ($PS_{35}\text{-}b\text{-}PEO_{10.5}$). $\Delta z = 10$ nm.

5.4.2 Spectroscopic Ellipsometry Data

Figure 5-3 shows typical time course data obtained with spectroscopic ellipsometry measurements for thin films of four polymers. The refractive index at 632.8 nm, n , and thickness of the films are shown in the upper and lower graphs, respectively. The durations of the exposure

to ethanol and water vapor are highlighted in red and blue, respectively. In general, the swelling led to an increase in film thickness and a decrease in n . The latter is consistent with the smaller refractive indexes (at 589 nm) of the solvents ($n_{\text{water}} = 1.333$ and $n_{\text{ethanol}} = 1.362$) compared to those of the polymers (1.454 for a PEO homopolymer and 1.586 for a PS homopolymer @632.8 nm). hPS_{16.4} showed negligible change in thickness and n upon exposure to either ethanol or water vapor, indicating that the polymer film was not swollen by these solvents, as reported previously.²²⁸ hPEO_{3.8} and hPEO_{12.5} did not show any changes in thickness and n for ethanol vapor, as PEO was not swollen by ethanol.²²⁹ In contrast, the PEO homopolymers were swollen by water as shown by an increase in film thickness and a decrease in n . The thickness and n did not return to the initial values after exposure to water vapor, probably because the film morphology changed due to its dissolution. Interestingly, thin films of both PS-*b*-PEO showed a reversible increase and decrease in thickness and refractive index (n), respectively, upon exposure not only to water vapor but also to ethanol vapor, indicating that PS-*b*-PEO films were swollen by ethanol and water vapor. These observations were unexpected, considering that ethanol is a poor solvent for both hPS_{16.4} and hPEO_{12.5}, as verified by the ellipsometry data.

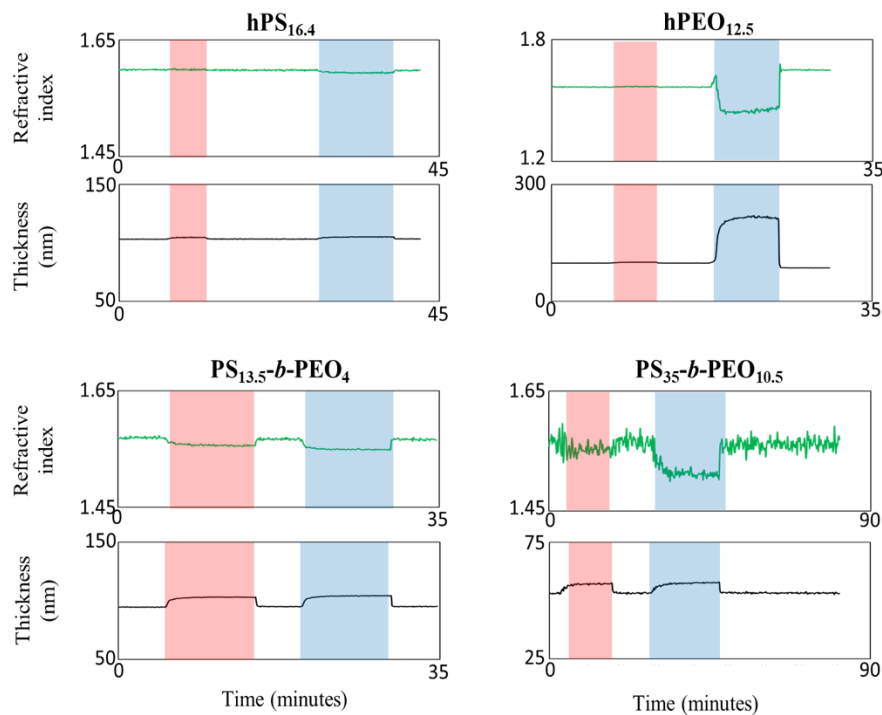


Figure 5-3: Typical time course data obtained with spectroscopic ellipsometry measurements (upper: refractive index at 632.8 nm; bottom: thickness) for thin polymer films upon exposure to ethanol vapor (highlighted in red) and water vapor (highlighted in blue). The films were exposed to nitrogen during the unhighlighted periods.

Figure 5-4 shows the pictures of a 100-nm thick hPEO_{3.5} film on Si substrates before and after its exposure to ethanol and water vapor. The picture clearly shows the disruption of the film homogeneity after the water vapor exposure, probably due to the dissolution of the polymer in water. Indeed, the ellipsometric thickness of the hPEO films did not recover to the initial thickness after water vapor exposure (Figure 5-3), indicating that the ellipsometric thickness change primarily reflected the change in the film structure rather than the swelling-induced change in film thickness.

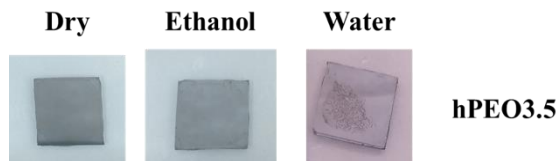


Figure 5-4: Optical images of a 100 nm thick hPEO_{3.5} film after each solvent exposure condition. The right image shows how the film is destroyed after exposure to water.

Figure 5-5 summarizes relationships between thickness gain, an increase in film thickness at a plateau upon exposure to each solvent vapor, and initial film thickness obtained under N₂ for hPS_{16.4}, hPEO_{12.5}, PS_{15.5-*b*}-PEO₄ and PS_{35-*b*}-PEO_{10.5}. Data for hPEO_{3.5} were not included because of the significant change in the homogeneity of its films after water vapor exposure (Figure 5-4). Thin films of hPS_{16.4} showed a negligible thickness change for water and a very small thickness gain for ethanol. The latter was independent of the initial thickness, suggesting that the thickness gain was due to the formation of a thin ethanol layer. In contrast, thin films of hPEO_{12.5} showed a water-induced thickness gain that is proportional to the initial thickness, indicating that the entire polymer film was swollen by water. These same films exhibited negligible thickness change for ethanol, demonstrating they were not swollen by ethanol. Interestingly, both PS_{15.5-*b*}-PEO₄ and PS_{35-*b*}-PEO_{10.5} films showed that exposure to ethanol and water vapor led to thickness gain that was proportional to initial thickness, indicating that they were swollen by ethanol and water in contrast to homopolymer counterparts. It is worth mentioning that the extent of the swelling for PS_{13.5-*b*}-PEO₄ was slightly larger than that for PS_{35-*b*}-PEO_{10.5}, as clarified by the insets in Figure 5-5.

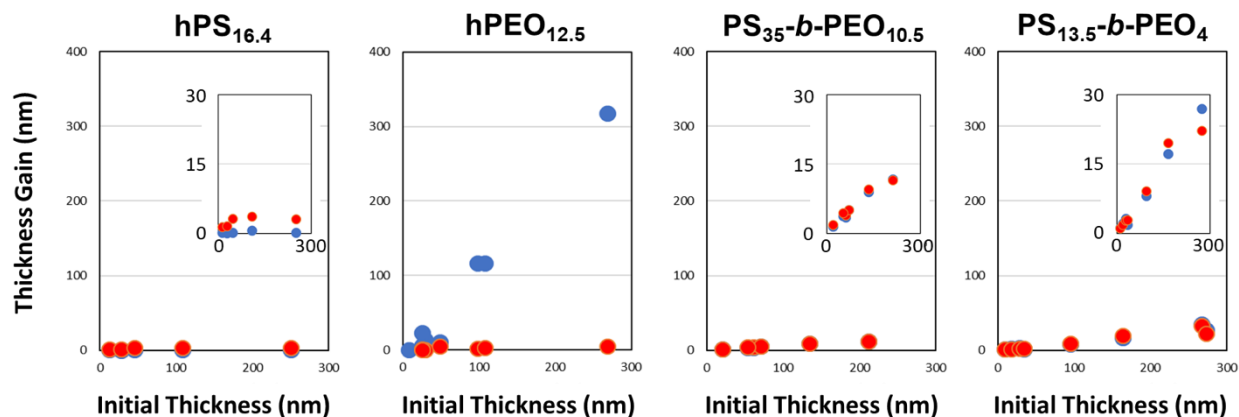


Figure 5-5: Plots for thickness gain (in nm) against initial thickness (in nm) for thin films of hPS_{16.4}; hPEO_{12.5}; PS₃₅-*b*-PEO_{10.5}; PS_{13.5}-*b*-PEO₄ (from left to right). The insets show expanded plots. Individual data points correspond to data obtained from individual different films. Thickness gain was calculated by subtracting initial film thickness from film thickness obtained after solvent vapor exposure.

5.4.3 SMT Measurements for SRB-Doped Thin Films

The solvent-induced increase in the thickness of PS-*b*-PEO films is likely due to the swelling of the PEO microdomains. The swelling is expected to enhance molecular diffusion in the microdomains.^{98,230} Here, SMT was used to assess the diffusion of SRB, which is shown to preferentially partition to PEO microdomains in a PS-*b*-PEO film, in thin PS-*b*-PEO and hPEO_{12.5} films before and after exposure to ethanol and water vapor. Figure 5-6 shows typical fluorescence images for thin SRB-doped films of hPEO_{12.5}, PS₃₅-*b*-PEO_{10.5} and PS_{13.5}-*b*-PEO₄. Isolated fluorescent spots corresponding to SRB molecules.

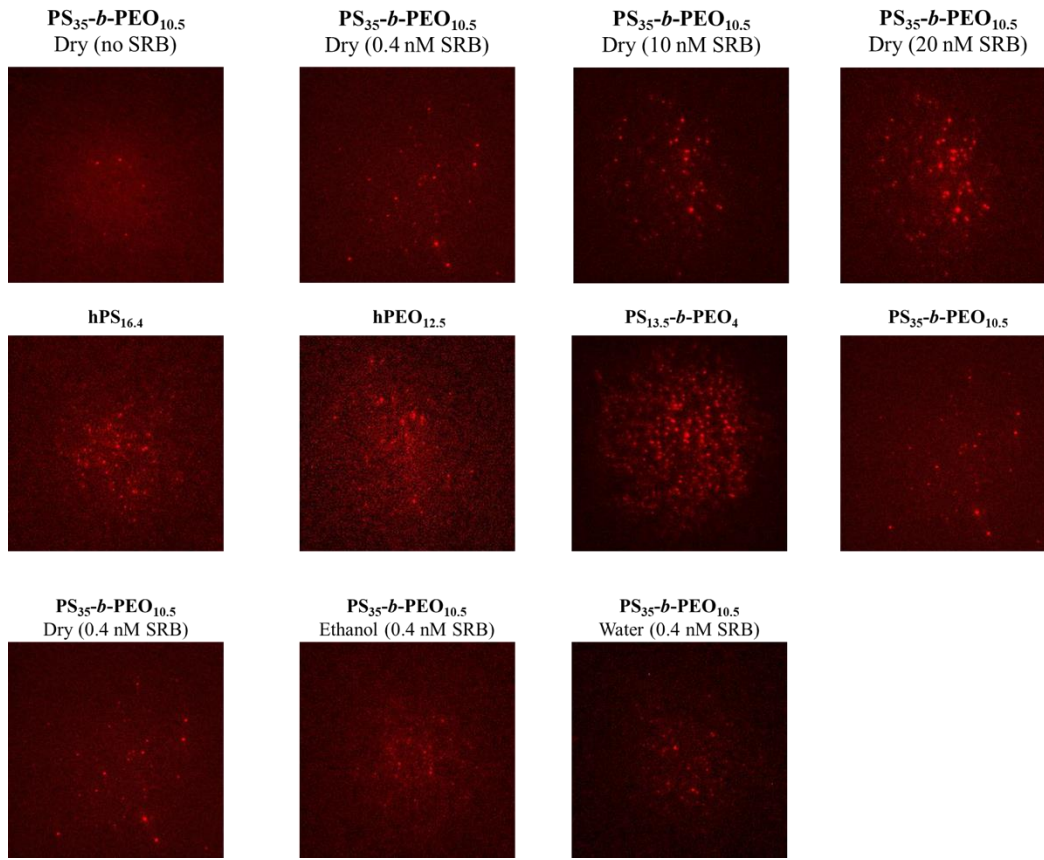


Figure 5-6: The upper row shows an increase in the number of the fluorescent spots with increasing SRB concentration, which supports the detection of single molecules. The middle row shows typical fluorescence images for thin SRB-doped films of hPEO_{12.5}, hPS_{16.4}, PS_{13.5}-*b*-PEO₄ and PS₃₅-*b*-PEO_{10.5} (0.4 nM SRB; 100 nm film thickness). Bottom images are typical data obtained for thin PS₃₅-*b*-PEO_{10.5} films image under dry condition and ethanol or water vapor. All the images are 16 x 16 μm²

These spots were basically immobile prior to exposure to solvent vapor. Upon exposure to ethanol or water vapor, fluorescent spots in the PS-*b*-PEO films seemed to possibly move due to the swelling of the PEO microdomains. In contrast, the motions of spots in hPEO_{12.5} films were not observed, possibly because the films were not swollen by ethanol and because molecules in water-swollen films moved too fast to record the EM-CCD camera (0.1 msec as a cycle time).

The SMT videos were analyzed to assess the diffusion coefficient of SRB molecules in these films using two different approaches. The first approach was the “manual method”, which

was based on the visual identification of the positions of a target molecule. The single molecule trajectory was created by linking the positions obtained from Dr. Higgins' LabView software. The second approach was the "software-based method", which provided a single-molecule trajectory using Dr. Higgins' LabView software with a certain threshold value on single frame displacement.³⁰ The latter approach is free from human bias, but suffers from a bias defined by the threshold as well as the inappropriate linking due to immobile spots. Once a trajectory was created, the diffusion coefficient was calculated from the slope of a plot of the mean square displacement (MSD) of the trajectory against time, as described in Figure 2-7.⁹⁸

Table 5-1 summarizes the diffusion coefficients (95% confidence interval) of SRB molecules in thin films of hPEO_{12.5}, PS₃₅-*b*-PEO_{10.5} and PS_{13.5}-*b*-PEO₄ that were calculated using the two approaches. For the case of the values obtained manually, the number of trajectories is seven and six for PS₃₅-*b*-PEO_{10.5} under water and ethanol, respectively. And four for the cases of PS_{13.5}-*b*-PEO₄ under ethanol vapor. The values obtained from the LabView software are averaged from more than 20 trajectories in all cases.

Table 5-1: Diffusion coefficients obtained from SMT data obtained in vapor-exposed thin films of hPEO_{12.5}, PS₃₅-*b*-PEO_{10.5} and PS_{13.5}-*b*-PEO₄. $D_{LabView}$ was obtained using the "software-based method", and D_{Manual} was obtained by the "manual method".

Polymer	Condition	$D_{LabView}$ ($\mu\text{m}^2/\text{s}$)	D_{Manual} ($\mu\text{m}^2/\text{s}$)
hPEO _{12.5}	Water	0.023 ± 0.006	NA
PS ₃₅ - <i>b</i> -PEO _{10.5}	Water	0.007 ± 0.002	$0.9 \pm 0.0_6$
PS ₃₅ - <i>b</i> -PEO _{10.5}	Ethanol	0.280 ± 0.435	$0.8 \pm 0.0_8$
PS _{13.5} - <i>b</i> -PEO ₄	Water	0.191 ± 0.382	NA
PS _{13.5} - <i>b</i> -PEO ₄	Ethanol	0.066 ± 0.012	$1.1 \pm 0.0_6$

*NA means that trajectories could not be created for these films without making arbitrary assumptions in linking the spots.

5.4.3.1 SMT Data Analysis with the “Manual Method”

Figure 5-7 shows an example of a trajectory obtained by the “manual method” for SRB molecules in a PS₃₅-*b*-PEO_{10.5} film under ethanol vapor. This analysis was examined to tackle the possibility of long displacements that could not be linked by the LabView software. This method could provide trajectories with longer step sizes, and thus a larger apparent diffusion coefficient (D_{Manual}) as compared with that obtained with the “software-based method” ($D_{LabView}$). Indeed, Table 5-1 shows larger D_{Manual} values than $D_{LabView}$ values for PS₃₅-*b*-PEO_{10.5} and PS_{13.5}-*b*-PEO₄ under water or ethanol vapor. Of note, D_{Manual} could not be obtained for water-exposed PS_{13.5}-*b*-PEO₄ films because reliable trajectories could not be obtained, possibly due to molecular motions that were too quick to follow.

The manual method was examined to solve the problems of the “software-based method”. However, a drawback of this method was recognized in the process: only a small number of trajectories could be created and analyzed because of the undefined criteria for linking. SRB molecules in these films moved in random directions, and sometimes “blinked”, that is their fluorescence intensity temporarily changed. The small number of trajectories prevented statistical discussion of the results and could only be used to qualitatively discuss changes in molecular motion induced by solvent vapor exposure.

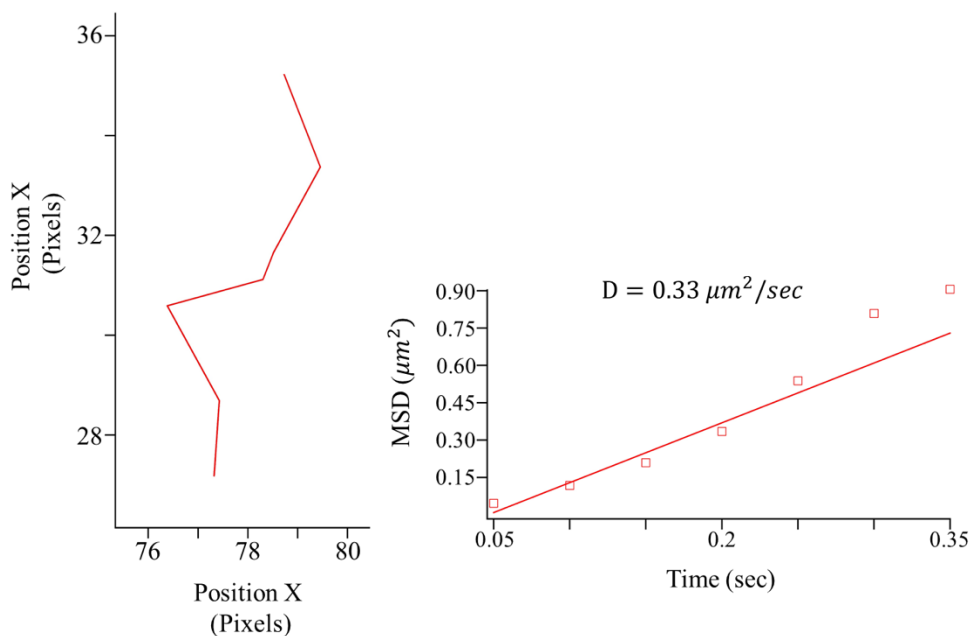


Figure 5-7: A trajectory of a SRB molecule in a PS₃₅-*b*-PEO_{10.5} film under ethanol vapor that was obtained using the “manual method”.

5.4.3.2 SMT Data Analysis with the “Software-Based Method”

The “software-based method” using the LabView software gave a much larger number of trajectories, permitting to obtain two parameters regarding molecular diffusion behavior: single molecule displacement (step size) and diffusion coefficient ($D_{LabView}$). As shown in Figure 5-8, mobile molecules should give larger molecular displacements (on average) than immobile ones.

Displacements obtained for immobile molecules originate from the localization precision of the measurement, which is defined by the imaging experiment (i.e., small uncontrolled motion of the microscopy stage) and the error of the Gaussian fitting controlled by the S/N of the image. Figure 5-8b shows histograms of molecular displacements obtained in thin films of hPEO_{12.5}, PS₃₅-*b*-PEO_{10.5} and PS_{13.5}-*b*-PEO₄ under different vapor environments. The histograms for hPEO_{12.5} show negligible change in the distribution of molecular displacement upon ethanol vapor exposure, and an increase in displacement upon water vapor exposure. These observations were consistent

with the ellipsometry data (Figure 5-5). Unfortunately, the histograms for PS₃₅-*b*-PEO_{10.5} and PS_{13.5}-*b*-PEO₄ did not show a clear increase in molecular displacement, possibly due to the bias defined by the threshold. In the software-based method, molecules moving quickly could not provide a trajectory because of their displacement larger than the threshold. The threshold value needed to be relatively small because of the presence of immobile spots that led to inappropriate linking.

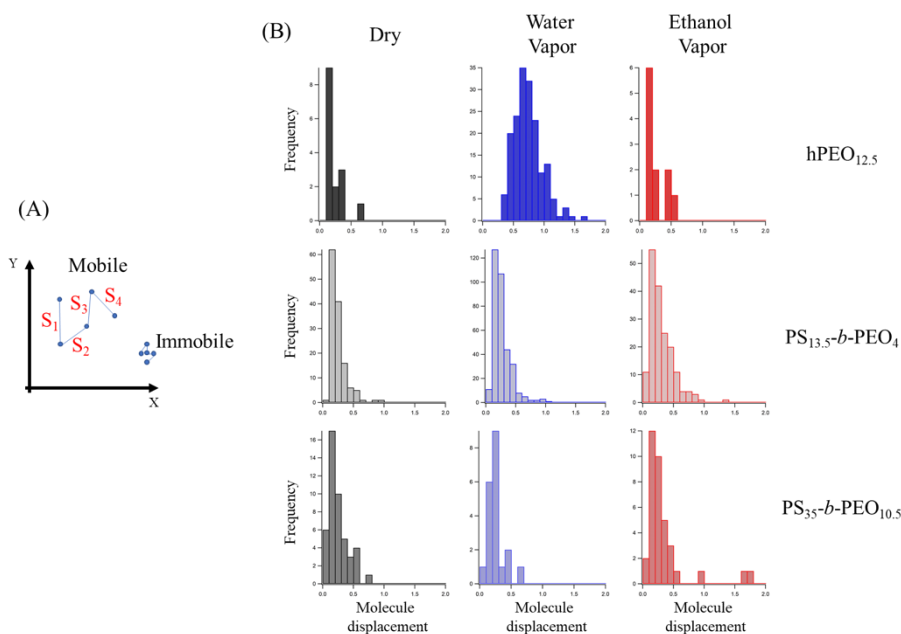


Figure 5-8: (A) Schematic trajectories of mobile and immobile molecules. The former shows larger displacements (step sizes). (B) Histograms of single molecule displacements for SRB molecules in thin films of hPEO_{12.5} (top), PS_{13.5}-*b*-PEO₄ (middle) and PS₃₅-*b*-PEO_{10.5} (bottom) under N₂ (left, black), water vapor (center, blue) and ethanol vapor (right, red).

The trajectory data were also used to determine the diffusion coefficient of each molecule ($D_{LabView}$). Here, all the trajectories were analyzed to obtain $D_{LabView}$ values from MSD plots as shown in Figure 5-7.

Figure 5-9 shows histograms for $D_{LabView}$ values obtained from SMT data for each polymer at each condition. The majority of trajectories in dry films under N_2 (left; shown in black) gave $D_{LabView}$ values below $2 \times 10^{-2} \mu m^2/s$. This D value was used as a threshold to judge whether molecules were mobile or immobile. Apparently, water-exposed hPEO_{12.5} (top), PS_{13.5}-*b*-PEO₄ (middle) and PS₃₅-*b*-PEO_{10.5} films gave trajectories with $D_{LabView}$ values larger than the threshold, indicating that the PEO moieties were swollen by water. In contrast, ethanol vapor exposure seemed to negligibly affect $D_{LabView}$ for hPEO_{12.5} films, and to give larger $D_{LabView}$ only for PS_{13.5}-*b*-PEO₄ (middle) and PS₃₅-*b*-PEO_{10.5} films. These observations for ethanol vapor were consistent with the ellipsometry data (Figure 5-4), supporting that ethanol vapor could swell PEO microdomains in PS-*b*-PEO films but not hPEO_{12.5} films. The non-Gaussian distribution of the $D_{LabView}$ values may suggest the heterogeneity of the extent of swelling in the polymer films.

Table 5-1 summarizes the $D_{LabView}$ values for these three polymers under ethanol or water vapor. Unfortunately, it was impossible to extract any trend on the swelling of PS-*b*-PEO and hPEO films by water and ethanol from the $D_{LabView}$ values, possibly because of the bias defined by the initial parameters for the linking as well as the insufficient number of trajectories analyzed in the SMT experiments.

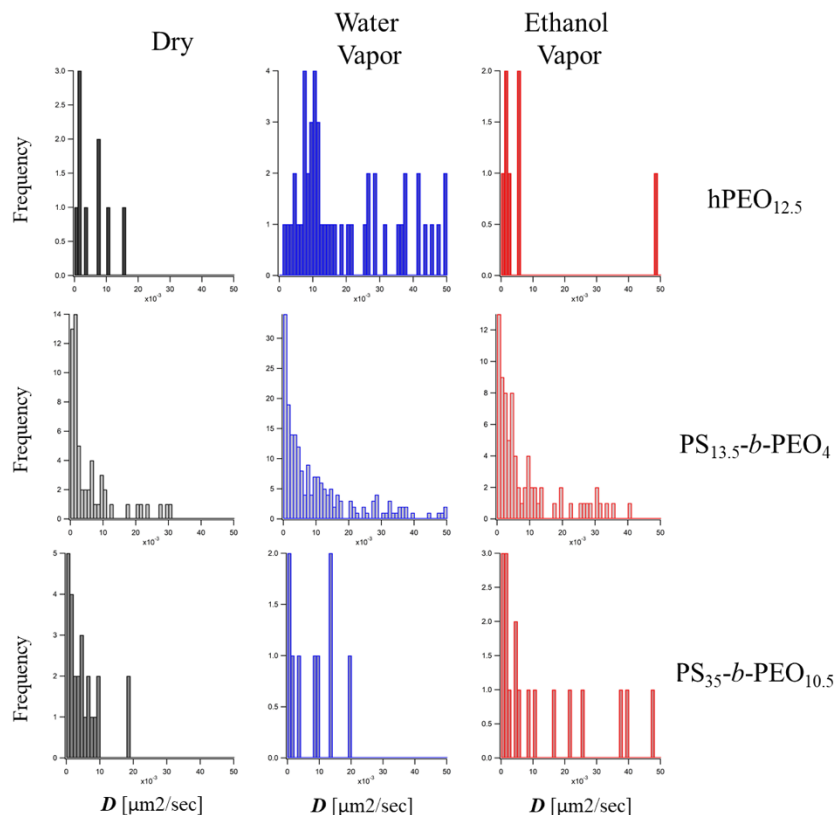


Figure 5-9: Histograms for $D_{LabView}$ values obtained in thin films of hPEO_{12.5} (top), PS_{13.5-*b*}-PEO₄ (middle) and PS_{35-*b*}-PEO_{10.5} (bottom) under N₂ (left, black), water vapor (center, blue) and ethanol vapor (right, red).

5.4.4 FCS Data for SRB

FCS was used to unveil fast molecular diffusion that could not be measured using SMT. Figure 5-10 shows (a) typical time course data and (b) autocorrelation functions obtained for hPEO_{12.5}, PS_{35-*b*}-PEO_{10.5} and PS_{13.5-*b*}-PEO₄ films under water vapor or ethanol vapor. No autocorrelation decay was found for films in N₂, because the films were not swollen. More interestingly, ethanol-exposed hPEO_{12.5} films gave no autocorrelation decay, either, supporting that hPEO_{12.5} films were not swollen by ethanol. For the other data, the autocorrelation function was fitted using the equation for two 2D diffusive components given in Table 2-3, which was hypothesized by a faster diffusion pathway corresponding to a surface solvent layer and a slower

pathway inside the polymer film. Table 5-2 summarizes the 95% confidence interval of diffusion coefficients obtained for hPEO_{12.5}, PS₃₅-*b*-PEO_{10.5}, and PS_{13.5}-*b*-PEO₄ under water or ethanol vapor. These data were obtained from 4-5 different areas of 3-4 different films.

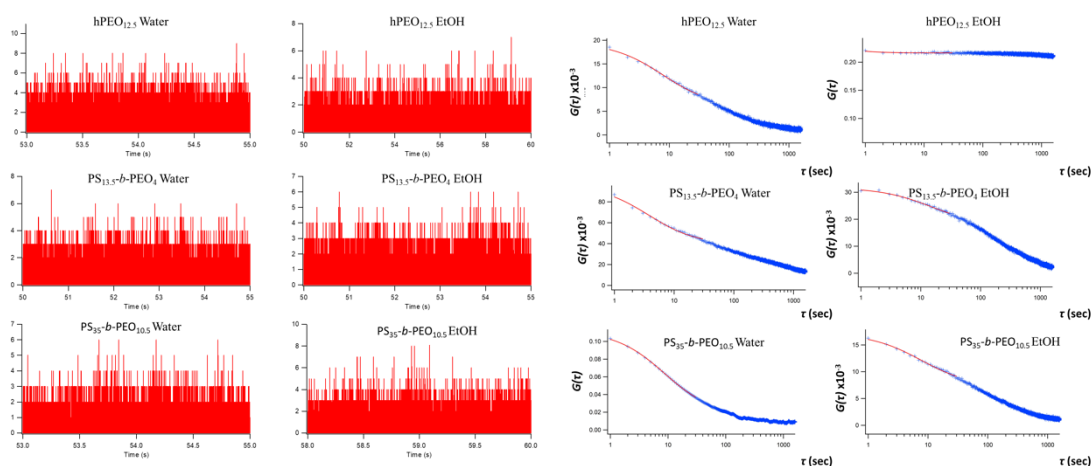


Figure 5-10: Left: Typical fluorescent time course data for hPEO_{12.5}, PS₃₅-*b*-PEO_{10.5} and PS_{13.5}-*b*-PEO₄ films under water vapor and ethanol vapor. Right: Autocorrelation functions obtained from the time course data for each polymer and condition.

Table 5-2: Diffusion coefficients obtained using FCS for the polymer films under different vapor conditions.

Polymer	Condition	D_{Fast} ($\mu\text{m}^2/\text{s}$)	D_{Slow} ($\mu\text{m}^2/\text{s}$)
hPEO _{12.5}	Water	495 ± 227	37.9 ± 12.5
PS ₃₅ - <i>b</i> -PEO _{10.5}	Water	252 ± 53	9.1 ± 2.0
PS _{13.5} - <i>b</i> -PEO ₄	Water	807 ± 293	20.7 ± 7.8
PS ₃₅ - <i>b</i> -PEO _{10.5}	Ethanol	4.7 ± 1.1	1.2 ± 0.5
PS _{13.5} - <i>b</i> -PEO ₄	Ethanol	28.6 ± 8.7	1.5 ± 0.8

The results indicate that for hPEO_{12.5}, PS₃₅-*b*-PEO_{10.5} and PS_{13.5}-*b*-PEO₄ under water vapor exposure, the SRB molecules diffuse in two different modes. The D_{Fast} values obtained in all the polymers are close to the value reported for SRB in solution as mentioned in Table 2-1. This result corroborates the hypothesis that the swollen PEO microdomain on the interface of the thin film “bloomed”. In that region the SRB molecules can move faster. The D_{Slow} values obtained can be assigned to the diffusion of the SRB molecules inside the thin films. In that case, the hPEO_{12.5} shows a faster diffusion of the molecules in comparison with the DBC where PS_{13.5}-*b*-PEO₄ shows a faster diffusion coefficient than PS₃₅-*b*-PEO_{10.5}. These results confirm that the use of the model based on two 2D components was appropriate for the autocorrelation fitting.

When exposed to ethanol vapor, hPEO_{12.5} shows no autocorrelation decay. This result is in agreement with SMT data where there was no observable motion of the SRB molecules. The D_{Fast} and D_{Slow} values for each of PS₃₅-*b*-PEO_{10.5} and PS_{13.5}-*b*-PEO₄ were close to each other and were significantly smaller than that in solution. This suggests that the fluctuations of fluorescence intensity observed came from SRB molecules inside the thin films. Interestingly, the D values observed for PS_{13.5}-*b*-PEO₄ were faster than those for PS₃₅-*b*-PEO_{10.5}, as with the D_{Slow} values obtained by water vapor exposure. The faster diffusion for smaller PS-*b*-PEO suggests a domain size effect on the swelling capabilities of the PEO microdomains.

5.4.5 Two-Color Imaging

5.4.5.1 Two-Color Ensemble Imaging

Two-color ensemble imaging with NR was used to discuss how polarity environment around the NR molecules changed upon exposure of the polymer films to solvent vapor, as

discussed in Section 2.2.2.1.1. The $E_{ensemble}$ value was calculated from the emission intensity at 580 ± 20 nm and 625 ± 20 nm using the following equation (eq. 2.7):

$$E = \frac{I_{polar} - I_{non\ polar}}{I_{polar} + I_{non\ polar}} = \frac{I_{625} - I_{580}}{I_{625} + I_{580}}$$

As shown in Figure 2-2(b), $E_{ensemble}$ is smaller in non-polar environments, permitting solvent-induced changes in environment polarity to be assessed. Figure 5-11 shows typical two-color images for the three polymers under three vapor conditions.

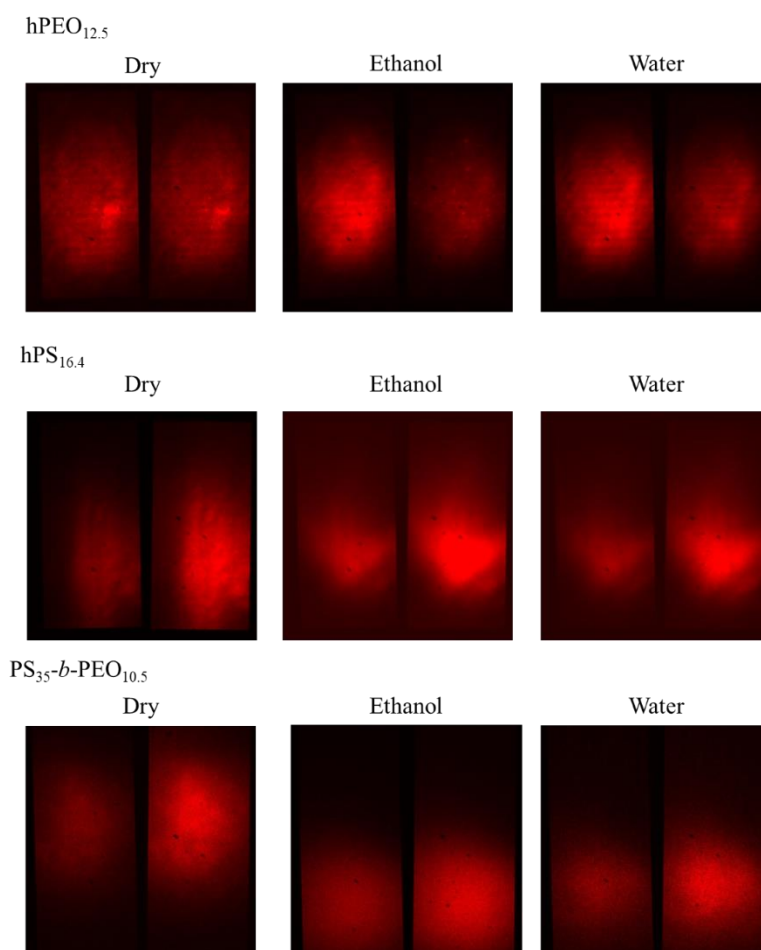


Figure 5-11: Typical two-color images for the three polymers under three vapor conditions. Left: 625 ± 20 nm; Right: 580 ± 20 nm. Film thickness: *ca.* 100 nm. Image size $16 \times 16 \mu\text{m}^2$

The average fluorescence intensity values of the images for the 580 ± 20 nm and 625 ± 20 nm channels were used to calculate $E_{ensemble}$. Table 5-3 summarizes $E_{ensemble}$ values for hPEO_{12.5}, PS_{35-b}-PEO_{10.5} and hPS_{16.4} thin films under different solvent vapor exposure conditions.

Table 5-3: $E_{ensemble}$ values (95% confidence interval) from NR doped in 100-nm thick films of hPEO_{12.5}, PS_{35-b}-PEO_{10.5} and hPS_{16.4} under N₂ (dry), ethanol vapor or water vapor.

<i>Polymer</i>	<i>Condition</i>	<i>E_{ensemble}</i>
hPEO _{12.5}	Dry	0.062 ± 0.006
hPEO _{12.5}	Water	0.220 ± 0.005
hPEO _{12.5}	Ethanol	0.307 ± 0.009
PS _{35-b} -PEO _{10.5}	Dry	-0.295 ± 0.002
PS _{35-b} -PEO _{10.5}	Water	-0.287 ± 0.003
PS _{35-b} -PEO _{10.5}	Ethanol	-0.255 ± 0.007
hPS _{16.4}	Dry	-0.340 ± 0.011
hPS _{16.4}	Water	-0.324 ± 0.031
hPS _{16.4}	Ethanol	-0.305 ± 0.011

The $E_{ensemble}$ values obtained in dry conditions for each film reveal the nature of the NR environment and therefore its location. For the case of hPS_{16.4}, the resulting $E_{ensemble}$ value is negative due to the non-polar environment of the NR in the homopolymer film. On the contrary, hPEO_{12.5} gives a positive $E_{ensemble}$ value, expected from a more polar environment than the polystyrene homopolymer thin film. These values were later used to conclude that the negative $E_{ensemble}$ value obtained from the PS_{35-b}-PEO_{10.5} is evidence of the NR located in the PS microdomains.

Upon identification of the NR microenvironment, the effect of solvent vapor on the PS microdomains was attested by the $E_{ensemble}$ calculated at each condition for each polymer. The $E_{ensemble}$ for hPS_{16.4} did not show any significant change upon solvent vapor exposure, reflecting no swelling of the thin film. For the case of hPEO_{12.5}, the $E_{ensemble}$ calculated under water vapor exposure confirmed the penetration of water molecules in the PEO thin film, increasing the $E_{ensemble}$ value. The increase in the $E_{ensemble}$ value upon ethanol vapor exposure can be associated with the Nile Red molecules exposed on the film/air interface. This might arise as a result of the poor partition of the probe inside the polymer film that set most of the probe in the interface. Another possible explanation for the large $E_{ensemble}$ value could be the penetration of the ethanol into the film. However, the penetration of the ethanol vapor into the hPEO_{12.5} did not show an increase in film thickness (see above), meaning that the penetration might be only happening in heterogeneous regions of the film.

For the case of the DBC, the NR located in the PS microdomains did not show any change in the $E_{ensemble}$ value. This observation reinforces the hypothesis that NR partitions into the of the PS microdomains as a structural block that it is not changed by exposure to poor solvents like water or ethanol.²³¹

Of note, Kim et. al.⁴⁷ showed that NR molecules in very thin PS films emitted red-shifted fluorescence due to their preferential distribution to the air/film and film/substrate interfaces, which could be more polar than the bulk PS. The effects of film thickness on $E_{ensemble}$ were measured for hPS_{16.4}, hPEO_{12.5} and PS_{35-*b*}-PEO_{10.5} to verify that the results obtained for 100-nm thick films primarily reflected solvent-induced changes in the environmental polarity of the films (Figure 5-12).

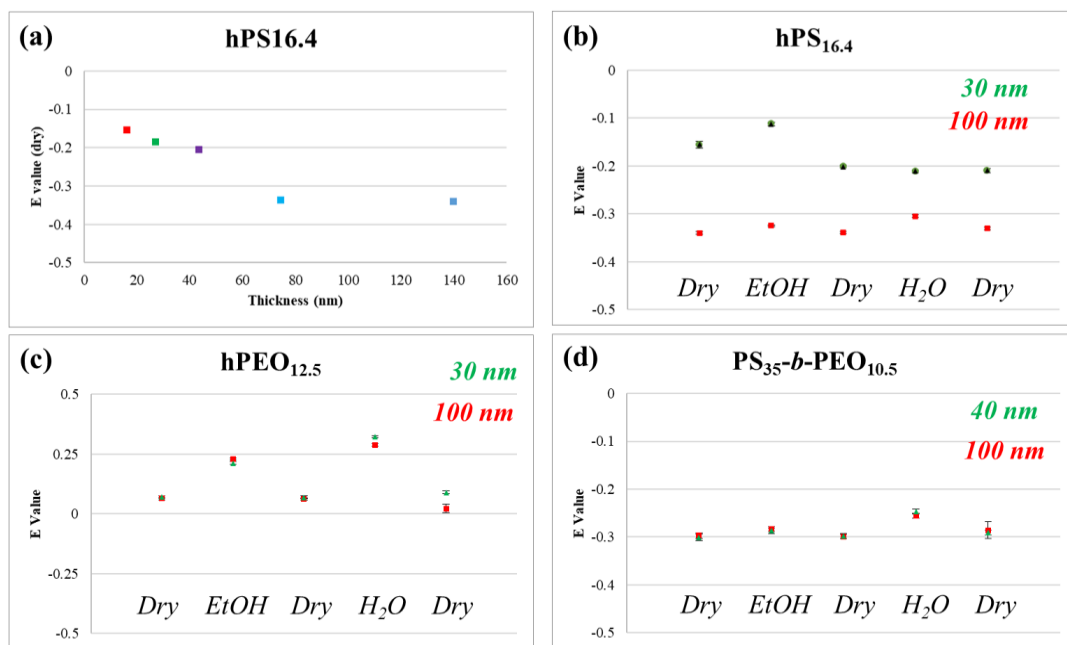


Figure 5-12: (a) Relationship between $E_{ensemble}$ and film thickness for hPS_{16.4}. (b,c,d) $E_{ensemble}$ for (b) hPS_{16.4}, (c) hPEO_{12.5} and (d) PS_{35-b}-PEO_{10.5} films of different thicknesses under N₂, ethanol and water vapor.

As reported by Kim, et al.,⁴⁷ $E_{ensemble}$ increased with decreasing thickness of hPS_{16.4} films (Figure 5-12ab). The thinner the hPS_{16.4} film showed a slightly larger increase in $E_{ensemble}$ upon exposure to ethanol vapor, suggesting the preferential distribution of NR molecules near the interfaces. In contrast, $E_{ensemble}$ was similar for hPEO_{12.5} and PS_{35-b}-PEO_{10.5} films with thicknesses of 30~100 nm regardless of the vapor exposure conditions (Figure 5-12cd). These results support that NR molecules in the PS_{35-b}-PEO_{10.5} films were present in the PS microdomains to give the negative $E_{ensemble}$ values. Moreover, a negligible change in $E_{ensemble}$ regardless of film thickness indicates that the PS microdomains are not permeable for ethanol and water vapor.

5.4.5.2 Nile Red Single Molecule Spectroscopic Imaging

SMT videos obtained for NR molecules in PS_{35-b}-PEO_{10.5} films showed no motion under any solvent exposure (water or ethanol). Figure 5-13a shows typical two-color images showing

individual NR molecules for hPEO_{12.5}, PS₃₅-*b*-PEO_{10.5} and hPS_{16.4}. Figure 5-13b shows the increase in spot number as the concentration of NR increases providing evidence that the spot is primarily coming from the single molecule observation.

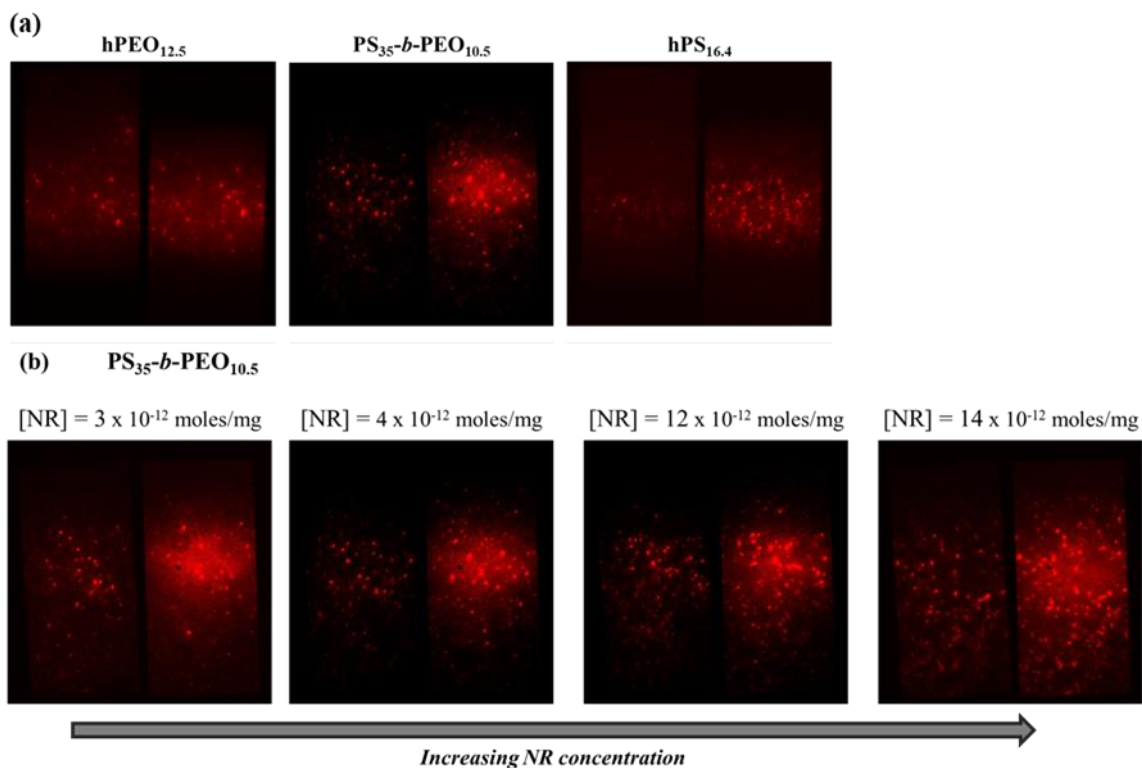


Figure 5-13: (a) Typical two-color images showing individual NR molecules in a two-window set up for hPEO_{12.5}, PS₃₅-*b*-PEO_{10.5} and hPS_{16.4}. (b) Typical two-color images of PS₃₅-*b*-PEO_{10.5} (≈ 100 nm) thin film at different NR concentrations. Left: 580 ± 20 nm; right: 625 ± 20 nm. Image size $16 \times 16 \mu\text{m}^2$.

The fluorescence intensity values of each molecule in each channel (580 ± 20 nm and 625 ± 20 nm) were used to calculate E_{SM} . Figure 5-14 shows histograms giving the E_{SM} values of single NR molecules in thin PS₃₅-*b*-PEO_{10.5} films under different solvent exposure conditions.

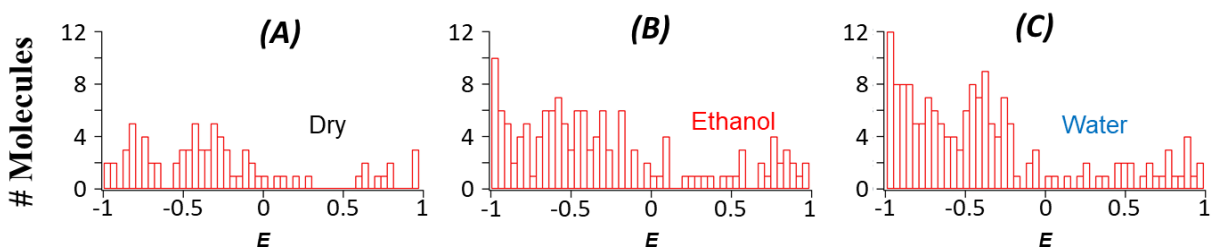


Figure 5-14: Histograms for the E_{SM} values of single NR molecules in thin PS₃₅-*b*-PEO_{10.5} films (*ca.* 100 nm thick) upon exposure to (A) N₂, (B) ethanol vapor and (C) water vapor.

The majority of NR molecules gave negative E_{SM} values, indicating that they were located in non-polar environments such as inside the PS microdomains. The average E_{SM} values obtained from the histograms were similar to the $E_{ensemble}$ values ($\overline{E_{SM}^{Dry}} = -0.319 \pm 0.035$; $\overline{E_{SM}^{Ethanol}} = -0.331 \pm 0.042$; $\overline{E_{SM}^{Water}} = -0.421 \pm 0.055$). More importantly, E_{SM} showed no significant change upon solvent exposure, confirming that no swelling of the PS microdomains occurred. It is worth mentioning that molecules that gave positive E_{SM} values may be located at the film/glass or film/air interfaces.⁴⁷

5.4.6 Nile Red Spectroscopic Measurements in Thin Films

The location of NR molecules in thin films were also discussed from fluorescence emission spectra to verify the conclusions obtained from the two-color measurements.^{232,233}

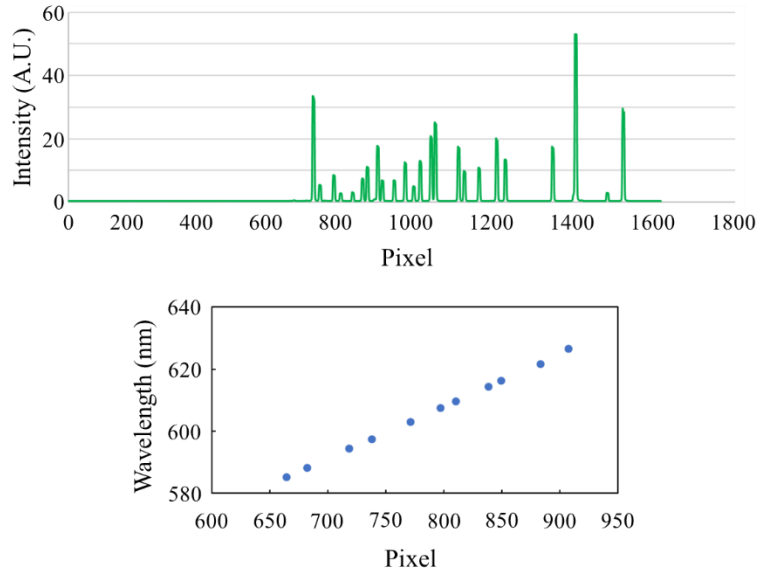


Figure 5-15: (a) Spectra from a Ne lamp used for the wavelength calibration of the spectrometer. (b) Calibration curve for the spectrometer pixel position.

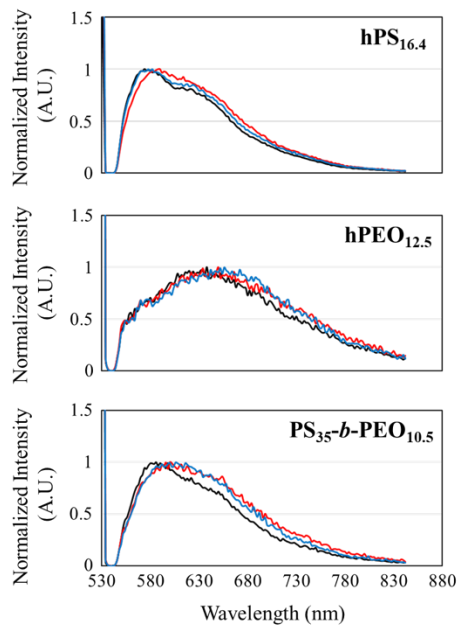


Figure 5-16: Fluorescence emission spectra of NR in ~100-nm thick films of hPEO_{12.5}, hPS_{16.4} and PS₃₅-*b*-PEO_{10.5} under N₂ (black), ethanol vapor (red) and water vapor (blue).

Figure 5-16 shows the NR fluorescence emission spectra in thin films of hPEO_{12.5}, hPS_{16.4} and PS₃₅-*b*-PEO_{10.5}. The spectra from hPS_{16.4} and PS₃₅-*b*-PEO_{10.5} thin films showed the characteristic shoulder from NR in a non-polar environment. In contrast, the spectra in the hPEO_{12.5} film showed a red shift. These results are consistent with the conclusions from the E values as discussed above. Upon exposure to ethanol or water vapor, the emission peak slightly red-shifted not only in the hPEO_{12.5} film but also in the hPS_{16.4} and PS₃₅-*b*-PEO_{10.5} films. The latter observations may be due to NR molecules located at the film/air and film/glass interfaces. Indeed, the E_{bulk} values were slightly more positive under ethanol and water vapor (Table 5-3). The spectroscopic data thus support that NR molecules were located in the PS microdomains of the PS-*b*-PEO film.

5.5 Conclusions

This study showed the swelling behavior of thin PS-*b*-PEO films upon exposure to water and ethanol vapor and compared it with that of PS and PEO homopolymers. Spectroscopic ellipsometry data showed a reversible increase in the thickness of PS-*b*-PEO films upon exposure to ethanol and water vapor. Thickness gain was proportional to the thickness of the dry film, indicating that the entire film was swollen by the solvents. PEO homopolymer films were swollen by water vapor, but not by ethanol vapor, and PS homopolymer films were not swollen by either of the solvents. These results suggested that the PEO microdomains were swollen by ethanol in contrast to PEO homopolymer. The swelling of PS-*b*-PEO films was verified by assessing the diffusion behavior of a fluorescent probe, SRB, that preferentially partitioned to PEO using SMT and FCS, in addition to a solvatochromic fluorescent probe, NR. The enhanced diffusion of SRB molecules in PS-*b*-PEO films was observed upon exposure to ethanol vapor as well as to water vapor, consistent with the swelling of the PEO microdomains by these solvents. In contrast, the

enhancement of diffusion was not revealed in hPEO films exposed to ethanol vapor. Furthermore, two-color imaging of NR molecules verified that PS microdomains in PS-*b*-PEO films were not swollen by these solvents. This observation supports that the PS microdomains can serve as structural pillars of PEO microdomains in PS-*b*-PEO monoliths.

FCS data suggested that the diffusion of SRB molecules in PEO microdomains swollen by ethanol and water vapors was faster in PS_{15.5}-*b*-PEO₄ films than PS₃₅-*b*-PEO_{10.5} films. The faster diffusion in the smaller PEO microdomains as well as the ethanol-induced swelling of PEO microdomains seem to reflect the poor packing of PEO microdomains. The poorer polymer packing in diblock copolymer microdomains was related to the results for polydimethylsiloxane (PDMS) microdomains in PS-*b*-PDMS films reported by del Valle-Carrandi et al.²³⁴ The poor packing may prevent the crystallization of PEO and enhance the dynamics of the PEO chains, which facilitated the swelling of PEO even by a poor solvent like ethanol.

The right selection of fluorescent probe dyes for single-molecule fluorescence methods makes it possible to obtain detailed information about nanoscale structures with distinct chemical properties. This strategy allows for valuable information on the properties of individual nanostructures to be extracted, which is not accessible using conventional ensemble-averaged methods.

6. General Conclusion and Future Directions

This dissertation demonstrates the use of small molecules' diffusion to control the modification of the inner surface of μm -scale polymeric pores and to explore the properties of polymer films swollen by solvent. Chapter 2 discusses the fundamental properties and measurement methods of molecular diffusion, and Chapter 3 summarizes the properties of polymers and analytical techniques used in my research.

In Chapter 4, the diffusion of small catalytic molecules was used to longitudinally control the surface modification of poly(ethylene terephthalate) (PET) track-etched pores. We took advantage of the electrochemical reduction and oxidation of a Cu-TBTA complex at the underlying electrode to control the diffusion-controlled distribution of catalytic Cu(I)-TBTA along μm -scale cylindrical and cone-shaped pores. The Cu(I)-TBTA led to the modification of the alkyne-tethered pore surfaces with azide-tagged fluorescent dyes via azide-alkyne cycloaddition click reaction. The pore modification was assessed from the cross-sectional profile of pores using fluorescence microscopy to investigate a relationship between the duration of Cu(I) production and modification length, which was supported by COMSOL finite element simulations done by Dr. Khanh-Hoa Tran-Ba. This approach based on electrochemically-controlled click reaction led to μm -scale gradient modification along the pore axis, permitting the asymmetrical modification of cylindrical pores with two different fluorescent dyes in the opposite direction of the membrane and the selective visualization of the tip and base openings of conical pores.

We explored the nanometer-scale control of longitudinal modification using the addition of a competitive oxidizing reagent (H_2O_2) to the solution and the application of short reduction potential pulses but was not successful. The presence of a gap between the underlying electrode and the membrane seemed not to deteriorate the control of pore modification at the μm scale

according to the COMSOL simulations but should be minimized for nm-scale control. A competitive oxidizing agent with slower reaction kinetics with Cu(I)-TBTA may help attain nm-scale modification. Furthermore, experimental conditions, including the density of surface alkyne groups and the number of short reduction potential pulses, should have been examined more carefully to immobilize a sufficient number of fluorescent dyes for the fluorescence microscopy detection. In addition, the following two approaches could be examined for the nm-scale modification. The first approach is the use of convective flow through the pores from the gap with the counter/reference electrode to that with the working electrode. The other approach is the use of a more viscous media to slow the diffusion of the catalyst.

In Chapter 5, the swelling of polymer films was assessed by measuring the diffusion of small fluorescent dyes such as sulforhodamine B (SRB) and Nile red (NR) in thin PS-*b*-PEO, PS homopolymer and PEO homopolymer films. Spectroscopic ellipsometry data unexpectedly revealed that thin films of PS_{15.5}-*b*-PEO₄ and PS₃₅-*b*-PEO_{10.5} could be swollen by ethanol, in contrast to those of hPS_{16.4} and PEO homopolymers (hPEO_{12.5} and hPEO_{3.8}). The swelling of PEO and PS microdomains in PS-*b*-PEO was investigated using fluorescence techniques including SMT, FCS, and two-color measurements with NR. The diffusion of SRB was observed in thin PS-*b*-PEO films exposed to ethanol vapor, indicating that ethanol-induced swelling observed for thin PS-*b*-PEO films reflected the swelling of the PEO microdomains of the thin films. In contrast, the diffusion of SRB in thin hPEO_{12.5} films was not observed upon ethanol vapor exposure, consistent with negligible swelling of the PEO homopolymer films. Both PEO microdomains in thin PS-*b*-PEO films and thin hPEO_{12.5} films could be swollen by water vapor, as shown by the diffusion of SRB. The immutability of hPS_{16.4} and the PS microdomains of PS-*b*-PEO under these solvent vapors was confirmed from the fluorescence emission of solvatochromic NR using two-color

wide-field microscopy at ensemble and single molecule levels as well as by spectroscopy. Furthermore, FCS was used to quantitatively assess swelling-induced changes in diffusion behavior of SRB in PEO microdomains. FCS results showed the faster SRB diffusion for PS_{15.5}-*b*-PEO₄ than PS₃₅-*b*-PEO_{10.5}, suggesting that the smaller PEO microdomains were swollen more significantly. This observation suggested the lower effective packing of the polymeric chains in the smaller PEO microdomains, leading to the facilitated swelling by ethanol. The lower packing in DBC microdomains were previously proposed by the lower T_g and dielectric spectra for PS-*b*-PDMS films by Del Valle Carrandi et al.²³⁴

Through this research, a series of interesting problems and questions showed up, including DBC solvent swelling mechanisms and the analysis methods of SMT data. As for the DBC solvent swelling, the mechanisms of solvent vapor annealing (SVA) has not been understood completely.^{50,235} Multiple techniques such as GISAXS,²³⁶ simultaneous SE and fluorescence microscopy,²²⁶ and in situ small-angle neutron scattering (SANS) and neutron reflectivity (NR),²³⁷ have been combined to unveil processes that drive the re-organization of microdomains during SVA. One possible future direction might be to record SMT data with different dyes during the SVA process, and to create a “structural map with super spatial resolution”. This map is expected to show the inner structural change of the microdomains through time and will be compared with the topographic images using AFM. Systematic in situ measurements with SMT and AFM for different DBCs with different sizes will deepen our understanding of SVA processes.

In SMT, I encountered two problems: the linking capability of the software used to create trajectories, and the impurities as a source of bad linking (in SMT) or unclear spots (while measuring E values for single NR molecules). To tackle the bad linking, one possible direction is to use artificial intelligence (AI) as a tool²³⁸ to get the most probable linking that can exceed the

“closest spot” range. AI is currently been exploited in several sciences,²³⁹ and is particularly common in image analysis for healthcare systems.²⁴⁰ The advances in image analysis can solve the problem with the creation of trajectories, since the software can create all possible trajectories and “choose” the most probable one. The AI “choosing” method relies on data fed to the AI software, which can be not only from experiments but also from simulations obtained for molecules diffusing within nanoscale pathways with known structures.²⁴¹ The use of simulation data may provide another level of information with a statistical value, in contrast to the current linking approaches where the resulting trajectories cannot be statistically evaluated. AI would also help with the nanoscale 3D structural mapping inside thin DBC or other nanostructured films.

Another source of error in SMT studies is bright spots that arise from impurities. In principle, impurities in a DBC can be reduced by the use of better/cleaner materials and methods used during the synthesis. However, it is very difficult to obtain impurity-free DBCs. During the analysis of my NR data, Dr. Higgins wrote a code for creating an image where each pixel is coming from a fluorescent spectrum. Figure 6-1 shows how an image is created using this code. A spectrum is recorded at each position of the stage. In a second step, a wavelength range is selected and the signal from that range is used to create the spectral image.

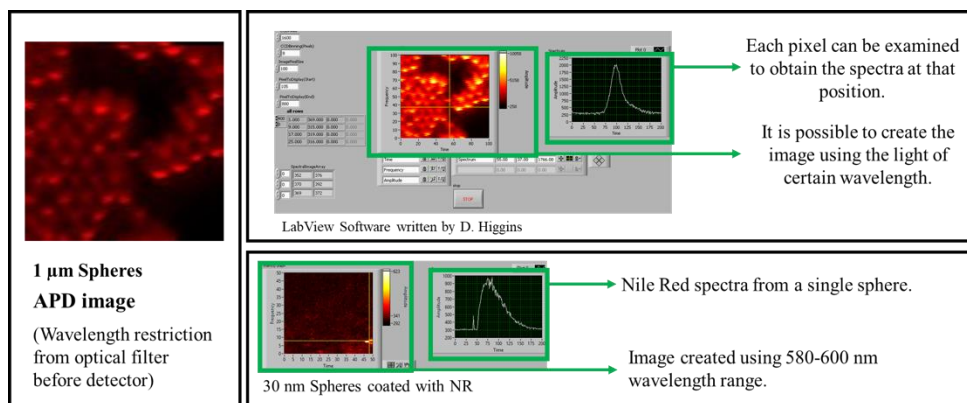


Figure 6-1: Image of 1 μm fluorosphere obtained with the APD detector. Same image obtained from the recompilation of spectroscopic fluorescences. Software written by Dr. Higgins.

This clever strategy would allow one to obtain the 3D distribution of single molecules that can be identified by their fluorescence spectra. Local polarity mapping can be achieved by the use of NR as a fluorescent probe. Furthermore, a “white laser”²⁴² can be used as an illumination source to simultaneously acquire a spectrally-resolved 3D image for a broad variety of fluorescent probes including those shown in Table 2-2.

In this study, the spectroscopic ellipsometer was modified to measure the thickness and refractive index of thin films against time. This modification allowed me to measure the swelling/deswelling kinetics of thin DBC films. Meanwhile, “evapo-porometry” was used to correlate a swelling/deswelling thickness profile with pore size in a membrane using the Kelvin equation.^{243–245} This method would be applicable to measure cavity size in a PS-*b*-PEO film after SVA if the microdomains form porous structures.

Another future direction might be the development of an FCS setup that collects fluorescence fluctuations only from the inside of a film, rather than across the entire film thickness. As mentioned in Chapter 2, FCS is widely used in biological systems as well as in material sciences. However, fluorescence signals are observed from the outer part of a thin film, including the air-film interface, due to the sub- μm -scale confocal volume (Figure 2-3d). It is well-known that molecular behavior at an air-film interface is different from that inside the film.^{106,107,246–248} Thus, it is desired to use a method that can only illuminate the inside of the film for measuring molecular diffusion from negligible influences from interfacial molecules. The use of the total internal reflection mode^{249–252} will be used to excite molecules only near the film-substrate interface on the basis of an evanescent wave, and thus will minimize the influence of molecules at

the air-film interface. This method depends entirely on empirical conditions, since in theory only a limit range of rays from the laser will hit at the proper angle required for the TIRF mode.

References

- (1) Bates, F. S.; Hillmyer, M. A.; Lodge, T. P.; Bates, C. M.; Delaney, K. T.; Fredrickson, G. H. Multiblock Polymers: Panacea or Pandora's Box? *Science*. **2012**, *336*, 434-440. <https://doi.org/10.1126/science.1215368>.
- (2) Elabd, Y. A.; Hickner, M. A. Block Copolymers for Fuel Cells. *Macromolecules*. **2011**, *44*, 1-11. <https://doi.org/10.1021/ma101247c>.
- (3) Phillip, W. A.; O'Neill, B.; Rodwogin, M.; Hillmyer, M. A.; Cussler, E. L. Self-Assembled Block Copolymer Thin Films as Water Filtration Membranes. *ACS Appl. Mater. Interfaces* **2010**, *2* (3), 847–853. <https://doi.org/10.1021/am900882t>.
- (4) Armstrong, J. A.; Bernal, E. E. L.; Yaroshchuk, A.; Bruening, M. L. Separation of Ions Using Polyelectrolyte-Modified Nanoporous Track-Etched Membranes. *Langmuir* **2013**, *29*, 10287-10296. <https://doi.org/10.1021/la401934v>.
- (5) Harandizadeh, Z.; Ito, T. Block Copolymer-Derived Recessed Nanodisk-Array Electrodes as Platforms for Folding-Based Electrochemical DNA Sensors. *ChemElectroChem*, **2019**, *6* (22), 5627–5632. <https://doi.org/10.1002/celec.201901562>.
- (6) Fick, A. 'On Liquid Diffusion'. *Philos. Mag. J. Sci.* **1855**, *10*, 31–39.
- (7) Einstein, A. Motion of Suspended Particles on the Kinetic Theory. *Ann. Phys.*, **1905**.
- (8) Skoog, D. A.; Holler, F. J.; Crouch, S. R. *Principles of Instrumental Analysis*, 6th ed.; Brooks/Cole, **2006**.
- (9) Ploem, J. S. *Introduction to Fluorescence Microscopy*; Oxford University Press, **1987**.
- (10) Krichevsky, O.; Bonnet, G. Fluorescence Correlation Spectroscopy: The Technique and Its Applications. *Reports Prog. Phys.* **2002**, *65* (2), 251–297. <https://doi.org/10.1088/0034-4885/65/2/203>.
- (11) Basché, T.; Ambrose, W. P.; Moerner, W. E. Optical Spectra and Kinetics of Single Impurity Molecules in a Polymer: Spectral Diffusion and Persistent Spectral Hole Burning. *J. Opt. Soc. Am. B* **1992**, *9* (5), 829. <https://doi.org/10.1364/JOSAB.9.000829>.
- (12) Carus, L. Titus L. On the Nature of the Universe. In *Titi Lvcreti Cari: De Rerum Natura: Libri Sex, Vol. 1: Prolegomena, Text and Critical Apparatus; Translation*; Bailey, C., Ed.; Oxford University Press, **1947**; pp 172–360. <https://doi.org/10.1093/oseo/instance.00168568>.
- (13) Ingen-Housz, J. *Nouvelles Expériences et Observations Sur Divers Objets De Physique*; **1784**.
- (14) Brown, R. Histoire Botanique Du Comté D'Angus. *Bull. la Société Bot. Fr.* **1872**, *19* (6), 214–222. <https://doi.org/10.1080/00378941.1872.10827631>.
- (15) Bard, A. J.; Faulkner, L. R. *Electrochemical Methods, Fundamentals and Applications*; ed. Wiley: New York. **2001**.
- (16) Levine, I. N. *Physical Chemistry 4*; ed: McGraw-Hill, Ed.; **1995**.
- (17) Einstein, A. Eine Neue Bestimmung Der Moleküldimensionen. *Ann. Phys.* **1906**, *324* (2), 289–306. <https://doi.org/10.1002/andp.19063240204>.
- (18) Wilke, C. R.; Chang, P. Correlation of Diffusion Coefficients in Dilute Solutions. *AIChE J.* **1955**, *1* (2), 264–270. <https://doi.org/10.1002/aic.690010222>.
- (19) Scheibel, E. G. Correspondence. Liquid Diffusivities. Viscosity of Gases. *Ind. Eng. Chem.* **1954**. <https://doi.org/10.1021/ie50537a062>.
- (20) Reid, R. C.; Sherwood, T. K.; Street, R. E. The Properties of Gases and Liquids. *Phys. Today* **1959**, *12* (4), 38–40. <https://doi.org/10.1063/1.3060771>.

- (21) Dymond, J. H. Corrected Enskog Theory and the Transport Coefficients of Liquids. *J. Chem. Phys.* **1974**, *60* (3), 969–973. <https://doi.org/10.1063/1.1681175>.
- (22) Funazukuri, T.; Ishiwata, Y.; Wakao, N. Predictive Correlation for Binary Diffusion Coefficients in Dense Carbon Dioxide. *AIChE J.* **1992**, *38* (11), 1761–1768. <https://doi.org/10.1002/aic.690381109>.
- (23) Catchpole, O. J.; King, M. B. Measurement and Correlation of Binary Diffusion Coefficients in Near Critical Fluids. *Ind. Eng. Chem. Res.* **1994**, *33* (7), 1828–1837. <https://doi.org/10.1021/ie00031a024>.
- (24) Liu, H.; Ruckenstein, E. A Predictive Equation for the Tracer Diffusion of Various Solutes in Gases, Supercritical Fluids, and Liquids. *Ind. Eng. Chem. Res.* **1997**, *36* (12), 5488–5500. <https://doi.org/10.1021/ie970331t>.
- (25) Einstein, A. *Investigations on the Theory of the Brownian Movement*; **1926**.
- (26) Graham, T. XII.—On the Application of Liquid Diffusion to Produce Decompositions. *Q. J. Chem. Soc.* **1851**, *3* (1), 60–67. <https://doi.org/10.1039/QJ8510300060>.
- (27) Graham, T. A Short Account of Experimental Researches on the Diffusion of Gases Through Each Other, and Their Separation by Mechanical Means. *Quart. J. Sci.* **1829**, *2*, 74–83.
- (28) Graham, T. On the Law of the Diffusion of Gases. *Phil. Mag.* **1833**, *2*, 175-190 269-276, 351–358.
- (29) Wisniak, J. Thomas Graham. I. Contributions to Thermodynamics, Chemistry, and the Occlusion of Gases. *Educ. Química* **2013**, *24* (3), 316–325. [https://doi.org/10.1016/S0187-893X\(13\)72481-9](https://doi.org/10.1016/S0187-893X(13)72481-9).
- (30) Higgins, D. A.; Park, S. C.; Tran-Ba, K.-H.; Ito, T. Single-Molecule Investigations of Morphology and Mass Transport Dynamics in Nanostructured Materials. *Annu. Rev. Anal. Chem.* **2015**, *8* (1), 193–216. <https://doi.org/10.1146/annurev-anchem-071114-040153>.
- (31) Gendron, P. O.; Avaltroni, F.; Wilkinson, K. J. Diffusion Coefficients of Several Rhodamine Derivatives as Determined by Pulsed Field Gradient-Nuclear Magnetic Resonance and Fluorescence Correlation Spectroscopy. *J. Fluoresc.* **2008**, *18*(6), 1093–1101. <https://doi.org/10.1007/s10895-008-0357-7>.
- (32) ThermoFisher, S. Reagents for Analysis of Low Molecular Weight amines <https://www.thermofisher.com/us/en/home/references/molecular-probes-the-handbook/fluorophores-and-their-amine-reactive-derivatives/reagents-for-analysis-of-low-molecular-weight-amines.html>.
- (33) Hiss, T. G.; Cussler, E. L. Diffusion in High Viscosity Liquids. *AIChE J.* **1973**, *19*(4), 698-703. <https://doi.org/10.1002/aic.690190404>.
- (34) Bogdan, M.; Brugger, D.; Rosenstiel, W.; Speiser, B. Estimation of Diffusion Coefficients from Voltammetric Signals by Support Vector and Gaussian Process Regression. *J. Cheminform.* **2014**, *6* (1), 30. <https://doi.org/10.1186/1758-2946-6-30>.
- (35) Masset, P.; Bottomley, D.; Konings, R.; Malmbeck, R.; Rodrigues, A.; Serp, J.; Glatz, J. P. Electrochemistry of Uranium in Molten LiCl-KCl Eutectic. *J. Electrochem. Soc.* **2005**, *152*(6), 1109-1115. <https://doi.org/10.1149/1.1901083>.
- (36) Cohen, Y.; Slovak, S. Diffusion NMR for the Characterization, in Solution, of Supramolecular Systems Based on Calixarenes, Resorcinarenes, and Other Macrocyclic Arenes. *Org. Chem. Front.* **2019**, *6* (10), 1705–1718. <https://doi.org/10.1039/C9QO00329K>.
- (37) Stejskal, E. O.; Tanner, J. E. Spin Diffusion Measurements: Spin Echoes in the Presence

- of a Time-Dependent Field Gradient. *J. Chem. Phys.* **1965**, *42* (1), 288–292.
<https://doi.org/10.1063/1.1695690>.
- (38) Dominguez-Medina, S.; Chen, S.; Blankenburg, J.; Swanglap, P.; Landes, C. F.; Link, S. Measuring the Hydrodynamic Size of Nanoparticles Using Fluctuation Correlation Spectroscopy. *Annu. Rev. Phys. Chem.* **2016**. <https://doi.org/10.1146/annurev-physchem-040214-121510>.
- (39) Kisley, L.; Poongavanam, M. V.; Kourentzi, K.; Willson, R. C.; Landes, C. F. PH-Dependence of Single-Protein Adsorption and Diffusion at a Liquid Chromatographic Interface. *J. Sep. Sci.* **2016**. <https://doi.org/10.1002/jssc.201500809>.
- (40) Faulón Marruecos, D.; Kastantin, M.; Schwartz, D. K.; Kaar, J. L. Dense Poly(Ethylene Glycol) Brushes Reduce Adsorption and Stabilize the Unfolded Conformation of Fibronectin. *Biomacromolecules* **2016**, *17* (3), 1017–1025.
<https://doi.org/10.1021/acs.biomac.5b01657>.
- (41) Hou, Y.; Higgins, D. A. Single Molecule Studies of Dynamics in Polymer Thin Films and at Surfaces: Effect of Ambient Relative Humidity. *J. Phys. Chem. B* **2002**, *106*(40), 10306-10315. <https://doi.org/10.1021/jp021200v>.
- (42) Jacob, M. H.; Ghosh, I.; D'Souza, R. N.; Nau, W. M. Two Orders of Magnitude Variation of Diffusion-Enhanced Förster Resonance Energy Transfer in Polypeptide Chains. *Polymers (Basel)*. **2018**, *10*(10), 1079. <https://doi.org/10.3390/polym10101079>.
- (43) Tran-Ba, K. H.; Higgins, D. A.; Ito, T. Fluorescence Recovery after Photobleaching and Single-Molecule Tracking Measurements of Anisotropic Diffusion within Identical Regions of a Cylinder-Forming Diblock Copolymer Film. *Anal. Chem.* **2015**, *87* (11), 5802–5809. <https://doi.org/10.1021/acs.analchem.5b01041>.
- (44) Martinez, V.; Henary, M. Nile Red and Nile Blue: Applications and Syntheses of Structural Analogues. *Chem. - A Eur. J.* **2016**, *22* (39), 13764–13782.
<https://doi.org/10.1002/chem.201601570>.
- (45) Giri, D.; Hanks, C. N.; Collinson, M. M.; Higgins, D. A. Single-Molecule Spectroscopic Imaging Studies of Polarity Gradients Prepared by Infusion-Withdrawal Dip-Coating. *J. Phys. Chem. C* **2014**, *118* (12), 6423–6432. <https://doi.org/10.1021/jp412508c>.
- (46) Hess, C. M.; Riley, E. A.; Palos-Chávez, J.; Reid, P. J. Measuring the Spatial Distribution of Dielectric Constants in Polymers through Quasi-Single Molecule Microscopy. *J. Phys. Chem. B* **2013**, *117*(23), 7106-7112. <https://doi.org/10.1021/jp4008398>.
- (47) Kim, H.-H.; Song, N. W.; Park, T. S.; Yoon, M. Laser Scanning Confocal Microscope (LSCM)-Fluorescence Spectral Properties of Nile Red Embedded in Polystyrene Film of Different Thickness. *Chem. Phys. Lett.* **2006**, *432* (1–3), 200–204.
<https://doi.org/10.1016/j.cplett.2006.10.049>.
- (48) Faulón Marruecos, D.; Kienle, D. F.; Kaar, J. L.; Schwartz, D. K. Grafting Density Impacts Local Nanoscale Hydrophobicity in Poly(Ethylene Glycol) Brushes. *ACS Macro Lett.* **2018**, *7*(4), 498-503. <https://doi.org/10.1021/acsmacrolett.8b00004>.
- (49) Amaro, M.; Filipe, H. A. L.; Prates Ramalho, J. P.; Hof, M.; Loura, L. M. S. Fluorescence of Nitrobenzoxadiazole (NBD)-Labeled Lipids in Model Membranes Is Connected Not to Lipid Mobility but to Probe Location. *Phys. Chem. Chem. Phys.* **2016**, *18*,7042-7054 .
<https://doi.org/10.1039/c5cp05238f>.
- (50) Lodge, T. P. Block Copolymers: Past Successes and Future Challenges. *Macromolecular Chemistry and Physics.* **2003**, *204*, 265-273. <https://doi.org/10.1002/macp.200290073>.
- (51) Ba, K. H. T.; Everett, T. A.; Ito, T.; Higgins, D. A. Trajectory Angle Determination in

- One Dimensional Single Molecule Tracking Data by Orthogonal Regression Analysis. *Phys. Chem. Chem. Phys.* **2011**, *13* (5), 1827. <https://doi.org/10.1039/c0cp01581d>.
- (52) Bannwarth, M.; Corrêa, I. R.; Sztretye, M.; Pouvreau, S.; Fella, C.; AnninaAebischer; Royer, L.; Ríos, E.; Johnsson, K. Indo-1 Derivatives for Local Calcium Sensing. *ACS Chem. Biol.* **2009**, *4*(3). <https://doi.org/10.1021/cb800258g>.
- (53) Hunter, R. C.; Beveridge, T. J. Application of a PH-Sensitive Fluoroprobe (C-SNARF-4) for PH Microenvironment Analysis in Pseudomonas Aeruginosa Biofilms. *Appl. Environ. Microbiol.* **2005**, *71*, 2501-2510. <https://doi.org/10.1128/AEM.71.5.2501-2510.2005>.
- (54) Marini, A.; Muñoz-Losa, A.; Biancardi, A.; Mennucci, B. What Is Solvatochromism? *J. Phys. Chem. B* **2010**, *114*, 51, 17128-1735. <https://doi.org/10.1021/jp1097487>.
- (55) Guido, C. A.; Mennucci, B.; Jacquemin, D.; Adamo, C. Planar vs. Twisted Intramolecular Charge Transfer Mechanism in Nile Red: New Hints from Theory. *Phys. Chem. Chem. Phys.* **2010**, *12*, 8016-8023. <https://doi.org/10.1039/b927489h>.
- (56) Mataga, N.; Kaifu, Y.; Koizumi, M. Solvent Effects upon Fluorescence Spectra and the Dipolemoments of Excited Molecules. *Bull. Chem. Soc. Jpn.* **1956**, *29* (4), 465–470. <https://doi.org/10.1246/bcsj.29.465>.
- (57) Lippert, E. Dipolmoment Und Elektronenstruktur von Angeregten Molekülen. *Zeitschrift für Naturforsch. A* **1955**, *10* (7). <https://doi.org/10.1515/zna-1955-0707>.
- (58) Lippert, E. Lösungsmittelkorrektur Und Unechte Maxima in Absorptionsspektren. *Angew. Chemie* **1955**, *67* (22), 704–704. <https://doi.org/10.1002/ange.19550672205>.
- (59) Hess, C. M.; Rudolph, A. R.; Reid, P. J. Imaging the Effects of Annealing on the Polymorphic Phases of Poly(Vinylidene Fluoride). *J. Phys. Chem. B* **2015**, *119*, 10, 4127-4132. <https://doi.org/10.1021/jp512486n>.
- (60) Dutta, A. K.; Kamada, K.; Ohta, K. Spectroscopic Studies of Nile Red in Organic Solvents and Polymers. *J. Photochem. Photobiol. A Chem.* **1996**, *93* (1), 57–64. [https://doi.org/10.1016/1010-6030\(95\)04140-0](https://doi.org/10.1016/1010-6030(95)04140-0).
- (61) Rood, J. Microscopy's Growth Through the Years <https://www.the-scientist.com/features/microscopys-growth-through-the-years-32775>.
- (62) Coceancigh, H.; Higgins, D. A.; Ito, T. Optical Microscopic Techniques for Synthetic Polymer Characterization. *Analytical Chemistry*. **2019**, *91*, 1, 405-424. <https://doi.org/10.1021/acs.analchem.8b04694>.
- (63) Cole-Palmer. Cole-Parmer Compound Trinocular Microscope with Tablet Display and Camera, Plan-Phase, 110-220 VAC <https://www.coleparmer.com/i/cole-parmer-compound-trinocular-microscope-with-tablet-display-and-camera-plan-phase-110-220-vac/4892314?searchterm=EW-48923-14>.
- (64) Klar, T. A.; Hell, S. W. Subdiffraction Resolution in Far-Field Fluorescence Microscopy. *Opt. Lett.* **1999**, *24*, 14, 954-956. <https://doi.org/10.1364/ol.24.000954>.
- (65) Hell, S. W.; Wichmann, J. Breaking the Diffraction Resolution Limit by Stimulated Emission: Stimulated-Emission-Depletion Fluorescence Microscopy. *Opt. Lett.* **1994**, *19*, 11, 780-782. <https://doi.org/10.1364/ol.19.000780>.
- (66) Abbe, E. Beiträge Zur Theorie Des Mikroskops Und Der Mikroskopischen Wahrnehmung. *Arch. für Mikroskopische Anat.* **1873**, *9* (1), 413–468. <https://doi.org/10.1007/BF02956173>.
- (67) Thompson, R. E.; Larson, D. R.; Webb, W. W. Precise Nanometer Localization Analysis for Individual Fluorescent Probes. *Biophys. J.* **2002**, *82* (5), 2775–2783. [https://doi.org/10.1016/S0006-3495\(02\)75618-X](https://doi.org/10.1016/S0006-3495(02)75618-X).

- (68) Betzig, E.; Patterson, G. H.; Sougrat, R.; Lindwasser, O. W.; Olenych, S.; Bonifacino, J. S.; Davidson, M. W.; Lippincott-Schwartz, J.; Hess, H. F. Imaging Intracellular Fluorescent Proteins at Nanometer Resolution. *Science*, **2006**, *313* (5793), 1642–1645. <https://doi.org/10.1126/science.1127344>.
- (69) Rust, M. J.; Bates, M.; Zhuang, X. Sub-Diffraction-Limit Imaging by Stochastic Optical Reconstruction Microscopy (STORM). *Nat. Methods* **2006**, *3* (10), 793–796. <https://doi.org/10.1038/nmeth929>.
- (70) Hess, S. T.; Girirajan, T. P. K.; Mason, M. D. Ultra-High Resolution Imaging by Fluorescence Photoactivation Localization Microscopy. *Biophys. J.* **2006**, *91* (11), 4258–4272. <https://doi.org/10.1529/biophysj.106.091116>.
- (71) Moerner, W. E. Microscopy beyond the Diffraction Limit Using Actively Controlled Single Molecules. *J. Microsc.* **2012**, *246* (3), 213–220. <https://doi.org/10.1111/j.1365-2818.2012.03600.x>.
- (72) Klar, T. A.; Jakobs, S.; Dyba, M.; Egner, A.; Hell, S. W. Fluorescence Microscopy with Diffraction Resolution Barrier Broken by Stimulated Emission. *Proc. Natl. Acad. Sci.* **2000**, *97* (15), 8206–8210. <https://doi.org/10.1073/pnas.97.15.8206>.
- (73) Wöll, D.; Braeken, E.; Deres, A.; De Schryver, F. C.; Uji-i, H.; Hofkens, J. Polymers and Single Molecule Fluorescence Spectroscopy, What Can We Learn? *Chem. Soc. Rev.* **2009**, *38* (2), 313–328. <https://doi.org/10.1039/B704319H>.
- (74) Moerner, W. E.; Shechtman, Y.; Wang, Q. Single-Molecule Spectroscopy and Imaging over the Decades. *Faraday Discuss.* **2015**, *184*, 9–36. <https://doi.org/10.1039/c5fd00149h>.
- (75) Moerner, W. E.; Fromm, D. P. Methods of Single-Molecule Fluorescence Spectroscopy and Microscopy. *Rev. Sci. Instrum.* **2003**, *74* (8), 3597–3619. <https://doi.org/10.1063/1.1589587>.
- (76) Webb, W. W. Fluorescence Correlation Spectroscopy: Genesis, Evolution, Maturation and Prognosis. *Springer Ser. Chem. Phys.* **2001**.
- (77) Magde, D.; Elson, E. L.; Webb, W. W. Fluorescence Correlation Spectroscopy. II. An Experimental Realization. *Biopolymers* **1974**, *13* (1), 29–61. <https://doi.org/10.1002/bip.1974.360130103>.
- (78) Haustein, E.; Schwille, P. Fluorescence Correlation Spectroscopy: Novel Variations of an Established Technique. *Annual Review of Biophysics and Biomolecular Structure.* **2007**, *36*, 151–169. <https://doi.org/10.1146/annurev.biophys.36.040306.132612>.
- (79) Haustein, E. Ultrasensitive Investigations of Biological Systems by Fluorescence Correlation Spectroscopy. *Methods* **2003**, *29* (2), 153–166. [https://doi.org/10.1016/S1046-2023\(02\)00306-7](https://doi.org/10.1016/S1046-2023(02)00306-7).
- (80) Aragón, S. R.; Pecora, R. Fluorescence Correlation Spectroscopy as a Probe of Molecular Dynamics. *J. Chem. Phys.* **1976**, *64* (4), 1791–1803. <https://doi.org/10.1063/1.432357>.
- (81) Kirkemide, A. W.; Torres, T.; Ito, T.; Higgins, D. A. Multiple Diffusion Pathways in Pluronic F127 Mesophases Revealed by Single Molecule Tracking and Fluorescence Correlation Spectroscopy. *J. Phys. Chem. B* **2011**, *115* (44), 12736–12743. <https://doi.org/10.1021/jp208234b>.
- (82) Brehm, E. H. M. Introduction - What Actually Is FCS. *Fluoresc. Correl. Spectrosc.* **2002**, 1–33. http://www.praktika.physik.uni-bayreuth.de/fcs_schwille.pdf
- (83) Banks, D. S.; Fradin, C. Anomalous Diffusion of Proteins Due to Molecular Crowding. *Biophys. J.* **2005**, *89*(5), 2960–2971. <https://doi.org/10.1529/biophysj.104.051078>.
- (84) Wachsmuth, M.; Waldeck, W.; Langowski, J. Anomalous Diffusion of Fluorescent Probes

- inside Living Cell Investigated by Spatially-Resolved Fluorescence Correlation Spectroscopy. *J. Mol. Biol.* **2000**, 298(4), 677-689. <https://doi.org/10.1006/jmbi.2000.3692>.
- (85) Rigler, R.; Mets, U.; Widengren, J.; Kask, P. Fluorescence Correlation Spectroscopy with High Count Rate and Low Background: Analysis of Translational Diffusion. *Eur. Biophys. J.* **1993**, 22 (3). <https://doi.org/10.1007/BF00185777>.
- (86) Haupts, U.; Maiti, S.; Schwille, P.; Webb, W. W. Dynamics of Fluorescence Fluctuations in Green Fluorescent Protein Observed by Fluorescence Correlation Spectroscopy. *Proc. Natl. Acad. Sci. U. S. A.* **1998**, 95(23), 13573-13578. <https://doi.org/10.1073/pnas.95.23.13573>.
- (87) Schwille, P.; Haupts, U.; Maiti, S.; Webb, W. W. Molecular Dynamics in Living Cells Observed by Fluorescence Correlation Spectroscopy with One- and Two-Photon Excitation. *Biophys. J.* **1999**, 77 (4), 2251–2265. [https://doi.org/10.1016/S0006-3495\(99\)77065-7](https://doi.org/10.1016/S0006-3495(99)77065-7).
- (88) Heikal, A. A.; Hess, S. T.; Baird, G. S.; Tsien, R. Y.; Webb, W. W. Molecular Spectroscopy and Dynamics of Intrinsically Fluorescent Proteins: Coral Red (DsRed) and Yellow (Citrine). *Proc. Natl. Acad. Sci.* **2000**, 97 (22), 11996–12001. <https://doi.org/10.1073/pnas.97.22.11996>.
- (89) Skaug, M. J.; Mabry, J. N.; Schwartz, D. K. Single-Molecule Tracking of Polymer Surface Diffusion. *J. Am. Chem. Soc.* **2014**, 136 (4), 1327–1332. <https://doi.org/10.1021/ja407396v>.
- (90) Chin, H. Y.; Wang, D.; Schwartz, D. K. Dynamic Molecular Behavior on Thermoresponsive Polymer Brushes. *Macromolecules* **2015**, 48 (13), 4562–4571. <https://doi.org/10.1021/acs.macromol.5b00729>.
- (91) Weisenburger, S.; Sandoghdar, V. Light Microscopy: An Ongoing Contemporary Revolution. *Contemp. Phys.* **2015**, 56 (2), 123–143. <https://doi.org/10.1080/00107514.2015.1026557>.
- (92) Paradiso, S.P., Delaney, K.T., Garcia-Cervera, C.J., Ceniceros, H.D., Fredrikson, G.H., Block Copolymer Self Assembly during Rapid Solvent Evaporation: Insights into Cylinder Growth and Stability, *ACS Macro. Lett.*, **2014**, 3, 16-20.
- (93) Heisenberg, W. K. *The Physical Principles of the Quantum Theory*; Chicago University Press: Chicago, **1930**.
- (94) Gelles, J.; Schnapp, B. J.; Sheetz, M. P. Tracking Kinesin-Driven Movements with Nanometre-Scale Precision. *Nature* **1988**, 331 (6155), 450–453. <https://doi.org/10.1038/331450a0>.
- (95) Mortensen, K. I.; Churchman, L. S.; Spudich, J. A.; Flyvbjerg, H. Optimized Localization Analysis for Single-Molecule Tracking and Super-Resolution Microscopy. *Nat. Methods* **2010**, 7 (5), 377–381. <https://doi.org/10.1038/nmeth.1447>.
- (96) Hua, Q. X.; Xin, B.; Xiong, Z. J.; Gong, W. L.; Li, C.; Huang, Z. L.; Zhu, M. Q. Super-Resolution Imaging of Self-Assembly of Amphiphilic Photoswitchable Macrocycles. *Chem. Commun.* **2017**, 53, 2669-2672. <https://doi.org/10.1039/c7cc00044h>.
- (97) Park, S. C.; Ito, T.; Higgins, D. A. Single Molecule Tracking Studies of Flow-Aligned Mesoporous Silica Monoliths: Aging-Time Dependence of Pore Order. *J. Phys. Chem. B* **2013**, 117 (16), 4222–4230. <https://doi.org/10.1021/jp303586h>.
- (98) Sapkota, D. R.; Tran-Ba, K.-H.; Elwell-Cuddy, T.; Higgins, D. A.; Ito, T. Single-Molecule Tracking Study of the Permeability and Transverse Width of Individual Cylindrical

- Microdomains in Solvent-Swollen Polystyrene- Block -Poly(Ethylene Oxide) Films. *J. Phys. Chem. B* **2016**, *120* (47), 12177–12183. <https://doi.org/10.1021/acs.jpccb.6b08368>.
- (99) Von Diezmann, A.; Shechtman, Y.; Moerner, W. E. Three-Dimensional Localization of Single Molecules for Super-Resolution Imaging and Single-Particle Tracking. *Chemical Reviews*. **2017**, *117*, 11, 7244–7275. <https://doi.org/10.1021/acs.chemrev.6b00629>.
- (100) Kumarasinghe, R.; Higgins, E. D.; Ito, T.; Higgins, D. A. Spectroscopic and Polarization-Dependent Single-Molecule Tracking Reveal the One-Dimensional Diffusion Pathways in Surfactant-Templated Mesoporous Silica. *J. Phys. Chem. C* **2016**, *120*, 1, 715–723. <https://doi.org/10.1021/acs.jpcc.5b10152>.
- (101) Sbalzarini, I. F.; Koumoutsakos, P. Feature Point Tracking and Trajectory Analysis for Video Imaging in Cell Biology. *J. Struct. Biol.* **2005**, *151* (2), 182–195. <https://doi.org/10.1016/j.jsb.2005.06.002>.
- (102) Sergé, A.; Bertaux, N.; Rigneault, H.; Marguet, D. Dynamic Multiple-Target Tracing to Probe Spatiotemporal Cartography of Cell Membranes. *Nat. Methods* **2008**, *5*(8), 687–694. <https://doi.org/10.1038/nmeth.1233>.
- (103) Claytor, K.; Khatua, S.; Guerrero, J. M.; Tcherniak, A.; Tour, J. M.; Link, S. Accurately Determining Single Molecule Trajectories of Molecular Motion on Surfaces. *J. Chem. Phys.* **2009**, *130* (16), 164710. <https://doi.org/10.1063/1.3118982>.
- (104) Seebacher, C.; Hellriegel, C.; Deeg, F.-W.; Bräuchle, C.; Altmaier, S.; Behrens, P.; Müllen, K. Observation of Translational Diffusion of Single Terrylenediimide Molecules in a Mesostructured Molecular Sieve. *J. Phys. Chem. B* **2002**, *106* (22), 5591–5595. <https://doi.org/10.1021/jp013198y>.
- (105) Hellriegel, C.; Kirstein, J.; Bräuchle, C.; Latour, V.; Pigot, T.; Olivier, R.; Lacombe, S.; Brown, R.; Guieu, V.; Payrastré, C.; et al. Diffusion of Single Streptocyanine Molecules in the Nanoporous Network of Sol–Gel Glasses †. *J. Phys. Chem. B* **2004**, *108* (38), 14699–14709. <https://doi.org/10.1021/jp049412a>.
- (106) Wang, D.; He, C.; Stoykovich, M. P.; Schwartz, D. K. Nanoscale Topography Influences Polymer Surface Diffusion. *ACS Nano* **2015**, *9* (2), 1656–1664. <https://doi.org/10.1021/nn506376n>.
- (107) Wang, D.; Wu, H.; Schwartz, D. K. Three-Dimensional Tracking of Interfacial Hopping Diffusion. *Phys. Rev. Lett.* **2017**, *119* (26), 1–6. <https://doi.org/10.1103/PhysRevLett.119.268001>.
- (108) Whinfield, J. R.; Dickson, J. T. A Process for Preparing Highly Polymeric Polyester (DE972503C), **1941**.
- (109) Bergmann, M.; Gutow, L.; Klages, M. *Marine Anthropogenic Litter*; Eds.; Springer International Publishing: Cham, **2015**. <https://doi.org/10.1007/978-3-319-16510-3>.
- (110) Apel, P. Track Etching Technique in Membrane Technology. *Radiat. Meas.* **2001**, *34*, 559–566. [https://doi.org/10.1016/S1350-4487\(01\)00228-1](https://doi.org/10.1016/S1350-4487(01)00228-1).
- (111) Apel, P. Y.; Blonskaya, I. V.; Dmitriev, S. N.; Mamonova, T. I.; Orelovitch, O. L.; Sartowska, B.; Yamauchi, Y. Surfactant-Controlled Etching of Ion Track Nanopores and Its Practical Applications in Membrane Technology. *Radiat. Meas.* **2008**, *43*, S552–S559. <https://doi.org/10.1016/j.radmeas.2008.04.057>.
- (112) Sartowska, B.; Starosta, W.; Apel, P.; Orelovitch, O.; Blonskaya, I. Polymeric Track Etched Membranes - Application for Advanced Porous Structures Formation. *Acta Phys. Pol. A* **2013**, *123* (5), 819–821. <https://doi.org/10.12693/APhysPolA.123.819>.
- (113) Ensinger, W.; Sudowe, R.; Brandt, R.; Neumann, R. Gas Separation in Nanoporous

- Membranes Formed by Etching Ion Irradiated Polymer Foils. *Radiat. Phys. Chem.* **2010**, 79 (3), 204–207. <https://doi.org/10.1016/j.radphyschem.2009.08.045>.
- (114) Lepoittevin, B.; Roger, P. Poly(Ethylene Terephthalate). In *Handbook of Engineering and Speciality Thermoplastics*; John Wiley & Sons, Inc.: Hoboken, NJ, USA, **2011**; pp 97–126. <https://doi.org/10.1002/9781118104729.ch4>.
- (115) Ulbricht, M. Advanced Functional Polymer Membranes. *Polymer*, **2006**, 47 (7), 2217–2262. <https://doi.org/10.1016/j.polymer.2006.01.084>.
- (116) Jenkins, A. D.; Kratochvíl, P.; Stepto, R. F. T.; Suter, U. W. Glossary of Basic Terms in Polymer Science (IUPAC Recommendations 1996). *Pure Appl. Chem.* **1996**, 68 (12), 2287–2311. <https://doi.org/10.1351/pac199668122287>.
- (117) Leibler, L. Theory of Microphase Separation in Block Copolymers. *Macromolecules* **1980**, 13 (6), 1602–1617. <https://doi.org/10.1021/ma60078a047>.
- (118) Matsushita, Y. Microphase Separation (of Block Copolymers). In *Encyclopedia of Polymeric Nanomaterials*; Kobayashi, S., Müllen, K., Eds.; Springer Berlin Heidelberg: Berlin, Heidelberg, **2014**; pp 1–6. https://doi.org/10.1007/978-3-642-36199-9_149-1.
- (119) Bates, F. S.; Hillmyer, M. A.; Lodge, T. P.; Bates, C. M.; Delaney, T.; Fredrickson, G. H.; Multiblock Polymers : Panacea or Pandora’s Box ? *Science*. **2012**, 336 (6080), 434–440.
- (120) Bates, F. S.; Fredrickson, G. H. Block Copolymers—Designer Soft Materials. *Phys. Today*, **1999**, 52 (2), 32–38. <https://doi.org/10.1063/1.882522>.
- (121) Ruzette, A.-V.; Leibler, L. Block Copolymers in Tomorrow’s Plastics. *Nat. Mater.* **2005**, 4 (1), 19–31. <https://doi.org/10.1038/nmat1295>.
- (122) Hamley, I. W. Structure and Flow Behaviour of Block Copolymers. *J. Phys. Condens. Matter* **2001**, 13 (33), R643–R671. <https://doi.org/10.1088/0953-8984/13/33/201>.
- (123) Ito, T. Block Copolymer-Derived Monolithic Polymer Films and Membranes Comprising Self-Organized Cylindrical Nanopores for Chemical Sensing and Separations. *Chemistry - An Asian Journal*. **2014**. <https://doi.org/10.1002/asia.201402136>.
- (124) Anastasiadis, Spiros, H. Diblock Copolymer Dynamics. *Curr. Opin. colloid interfaces Sci.* **2000**, 5, 324–333.
- (125) Matsen, M. W.; Schick, M. Stable and Unstable Phases of a Diblock Copolymer Melt. *Phys. Rev. Lett.* **1994**, 72 (16), 2660–2663. <https://doi.org/10.1103/PhysRevLett.72.2660>.
- (126) Matsen, M. W.; Schick, M. Stable and Unstable Phases of a Linear Multiblock Copolymer Melt. *Macromolecules* **1994**, 27 (24), 7157–7163. <https://doi.org/10.1021/ma00102a025>.
- (127) Schacher, F. H.; Rugar, P. A.; Manners, I. Functional Block Copolymers: Nanostructured Materials with Emerging Applications. *Angew. Chemie Int. Ed.* **2012**, 51 (32), 7898–7921. <https://doi.org/10.1002/anie.201200310>.
- (128) Tseng, Y. C.; Darling, S. B. Block Copolymer Nanostructures for Technology. *Polymers*. **2010**, 2(4), 470–489. <https://doi.org/10.3390/polym2040470>.
- (129) Segalman, R. A. Patterning with Block Copolymer Thin Films. *Mater. Sci. Eng. R Reports* **2005**, 48 (6), 191–226. <https://doi.org/10.1016/j.mser.2004.12.003>.
- (130) Joo, W.; Park, M. S.; Kim, J. K. Block Copolymer Film with Sponge-like Nanoporous Structure for Antireflection Coating. *Langmuir* **2006**, 22, 19, 7960–7963. <https://doi.org/10.1021/la061441k>.
- (131) Urade, V. N.; Wei, T.-C.; Tate, M. P.; Kowalski, J. D.; Hillhouse, H. W. Nanofabrication of Double-Gyroid Thin Films. *Chem. Mater.* **2007**, 19 (4), 768–777. <https://doi.org/10.1021/cm062136n>.
- (132) Crossland, E. J. W.; Kamperman, M.; Nedelcu, M.; Ducati, C.; Wiesner, U.; Smilgies, D.

- M.; Toombes, G. E. S.; Hillmyer, M. A.; Ludwigs, S.; Steiner, U. A Bicontinuous Double Gyroid Hybrid Solar Cell. *Nano Lett.* **2009**, *9*, 8, 2807-2812.
<https://doi.org/10.1021/nl803174p>.
- (133) Ruiz, R.; Kang, H.; Detcheverry, F. A.; Dobisz, E.; Kercher, D. S.; Albrecht, T. R.; de Pablo, J. J.; Nealey, P. F. Density Multiplication and Improved Lithography by Directed Block Copolymer Assembly. *Science*, **2008**, *321* (5891), 936–939.
<https://doi.org/10.1126/science.1157626>.
- (134) Park, S.; Wang, J. Y.; Kim, B.; Xu, J.; Russell, T. P. A Simple Route to Highly Oriented and Ordered Nanoporous Block Copolymer Templates. *ACS Nano* **2008**, *2*, 4, 766-772.
<https://doi.org/10.1021/nn7004415>.
- (135) Park, M. Block Copolymer Lithography: Periodic Arrays of 1011 Holes in 1 Square Centimeter. *Science (80-.)*. **1997**, *276* (5317), 1401–1404.
<https://doi.org/10.1126/science.276.5317.1401>.
- (136) Thurn-Albrecht, T.; Steiner, R.; DeRouchey, J.; Stafford, C. M.; Huang, E.; Bal, M.; Tuominen, M.; Hawker, C. J.; Russell, T. P. Nanoscopic Templates from Oriented Block Copolymer Films. *Adv. Mater.* **2000**, *12* (11), 787–791.
[https://doi.org/10.1002/\(SICI\)1521-4095\(200006\)12:11<787::AID-ADMA787>3.0.CO;2-1](https://doi.org/10.1002/(SICI)1521-4095(200006)12:11<787::AID-ADMA787>3.0.CO;2-1).
- (137) Olson, D. A.; Chen, L.; Hillmyer, M. A. Templating Nanoporous Polymers with Ordered Block Copolymers. *Chemistry of Materials*. **2008**, *20*, 3, 869-890.
<https://doi.org/10.1021/cm702239k>.
- (138) Yang, S. Y.; Ryu, I.; Kim, H. Y.; Kim, J. K.; Jang, S. K.; Russell, T. P. Nanoporous Membranes with Ultrahigh Selectivity and Flux for the Filtration of Viruses. *Adv. Mater.* **2006**, *18*(6), 709-712. <https://doi.org/10.1002/adma.200501500>.
- (139) Park, S.; Wang, J.-Y.; Kim, B.; Chen, W.; Russell, T. P. Solvent-Induced Transition from Micelles in Solution to Cylindrical Microdomains in Diblock Copolymer Thin Films. *Macromolecules* **2007**, *40* (25), 9059–9063. <https://doi.org/10.1021/ma071321z>.
- (140) Cavicchi, K. A.; Berthiaume, K. J.; Russell, T. P. Solvent Annealing Thin Films of Poly(Isoprene-b-Lactide). *Polymer*, **2005**, *46* (25), 11635–11639.
<https://doi.org/10.1016/j.polymer.2005.09.072>.
- (141) Kim, G.; Libera, M. Morphological Development in Solvent-Cast Polystyrene-Polybutadiene-Polystyrene (SBS) Triblock Copolymer Thin Films. *Macromolecules*, **1998**, *31*, 8, 2569-2577. <https://doi.org/10.1021/ma971349i>.
- (142) Kim, S. H.; Misner, M. J.; Russell, T. P. Controlling Orientation and Order in Block Copolymer Thin Films. *Adv. Mater.* **2008**, *20* (24), 4851–4856.
<https://doi.org/10.1002/adma.200701206>.
- (143) Kim, S. H.; Misner, M. J.; Russell, T. P. Solvent-Induced Ordering in Thin Film Diblock Copolymer/Homopolymer Mixtures. *Adv. Mater.* **2004**, *16* (23–24), 2119–2123.
<https://doi.org/10.1002/adma.200306577>.
- (144) Peng, J.; Han, Y.; Knoll, W.; Kim, D. H. Development of Nanodomain and Fractal Morphologies in Solvent Annealed Block Copolymer Thin Films. *Macromol. Rapid Commun.* **2007**, *28* (13), 1422–1428. <https://doi.org/10.1002/marc.200700206>.
- (145) Landmarks, A. C. S. N. H. C. Hermann Staudinger and the Foundation of Polymer Science
<https://www.acs.org/content/acs/en/education/whatischemistry/landmarks/staudingerpolymerscience.html>.

- (146) Darain, F.; Gan, K. L.; Tjin, S. C. Antibody Immobilization on to Polystyrene Substrate—on-Chip Immunoassay for Horse IgG Based on Fluorescence. *Biomed. Microdevices* **2009**, *11* (3), 653–661. <https://doi.org/10.1007/s10544-008-9275-3>.
- (147) Browne, M. M.; Lubarsky, G. V.; Davidson, M. R.; Bradley, R. H. Protein Adsorption onto Polystyrene Surfaces Studied by XPS and AFM. *Surf. Sci.* **2004**, *553*, 155-167. <https://doi.org/10.1016/j.susc.2004.01.046>.
- (148) Lourenço, A. *Comptes Rendus Chim.* **1859**, *49*, 619.
- (149) Lourenço, A. *Ann. Chim. Phys.* **1863**, *67*, 257.
- (150) Kahovec, J.; Fox, R. B.; Hatada, K. Nomenclature of Regular Single-Strand Organic Polymers (IUPAC Recommendations 2002). *Pure Appl. Chem.* **2002**, *74* (10), 1921–1956. <https://doi.org/10.1351/pac200274101921>.
- (151) Bailey, F.E., Koleske J. V., Proprieties of Poly(ethylene oxide); *Elsevier*, **1976**; pp 105–149. <https://doi.org/10.1016/B978-0-12-073250-0.50010-6>.
- (152) Ingham, J. D.; Lawson, D. D. Refractive Index–Molecular Weight Relationships for Poly(Ethylene Oxide). *J. Polym. Sci. Part A Gen. Pap.* **1965**, *3*, 7, 2707-2710. <https://doi.org/10.1002/pol.1965.100030728>.
- (153) Zalipsky, S.; Harris, J. M. Introduction to Chemistry and Biological Applications of Poly(Ethylene Glycol). *ACS Symp. Ser.* Washington DC, **1997**, .
- (154) Zalipsky, S. Chemistry of Polyethylene Glycol Conjugates with Biologically Active Molecules. *Advanced Drug Delivery Reviews.* **1995**, *16*, 157-182. [https://doi.org/10.1016/0169-409X\(95\)00023-Z](https://doi.org/10.1016/0169-409X(95)00023-Z).
- (155) Paternostre, L.; Damman, P.; Dosiere, M. Morphology and Crystal Structure of the Poly(Ethylene Oxide)-Hydroquinone Molecular Complex. *J. Polym. Sci. Part B Polym. Phys.* **1999**, *37* (12), 1197–1208. [https://doi.org/10.1002/\(SICI\)1099-0488\(19990615\)37:12<1197::AID-POLB1>3.0.CO;2-C](https://doi.org/10.1002/(SICI)1099-0488(19990615)37:12<1197::AID-POLB1>3.0.CO;2-C).
- (156) Strawhecker, K. E.; Manias, E. Crystallization Behavior of Poly(Ethylene Oxide) in the Presence of Na⁺ Montmorillonite Fillers. *Chem. Mater.* **2003**, *15*, 4, 844-849. <https://doi.org/10.1021/cm0212865>.
- (157) Lightfoot, P.; Mehta, M. A.; Bruce, P. G. Crystal Structure of the Polymer Electrolyte Poly(Ethylene Oxide)₃LiCF₃SO₃. *Science*, **1993**, *262* (5135), 883–885. <https://doi.org/10.1126/science.262.5135.883>.
- (158) Jeon, S. .; Lee, J. .; Andrade, J. .; De Gennes, P. . Protein—Surface Interactions in the Presence of Polyethylene Oxide. *J. Colloid Interface Sci.* **1991**, *142* (1), 149–158. [https://doi.org/10.1016/0021-9797\(91\)90043-8](https://doi.org/10.1016/0021-9797(91)90043-8).
- (159) Scriven, L. E. Physics and Applications of DIP Coating and Spin Coating. *MRS Proc.* **1988**, *121*, 717. <https://doi.org/10.1557/PROC-121-717>.
- (160) Lawrence, C. J. The Mechanics of Spin Coating of Polymer Films. *Phys. Fluids* **1988**, *31* (10), 2786. <https://doi.org/10.1063/1.866986>.
- (161) Ossila. Spin Coating: A Guide to Theory and Techniques <https://www.ossila.com/pages/spin-coating>.
- (162) Danglad-Flores, J.; Eickelmann, S.; Riegler, H. Deposition of Polymer Films by Spin Casting: A Quantitative Analysis. *Chem. Eng. Sci.* **2018**, *179*, 257–264. <https://doi.org/10.1016/j.ces.2018.01.012>.
- (163) Tompkins, H. G.; Irene, E. A. *Handbook of Ellipsometry*; William Andrew Publishing, Springer, **2005**.
- (164) J.A. Woollam Ellipsometry Solutions. Ellipsometry tutorial

- www.jawoollam.com/resources/ellipsometry-tutorial.
- (165) Guenther, R. B. Augustin-Louis Cauchy: A Biography (Bruno Belhoste). *SIAM Rev.* **1992**, *34* (3), 508–509. <https://doi.org/10.1137/1034103>.
- (166) Kissinger, P. T.; Heineman, W. R. Cyclic Voltammetry. *J. Chem. Educ.* **1983**, *60* (9), 702. <https://doi.org/10.1021/ed060p702>.
- (167) Coceancigh, H.; Tran-Ba, K.-H.; Siepser, N.; Baker, L. A.; Ito, T. Longitudinally Controlled Modification of Cylindrical and Conical Track-Etched Poly(Ethylene Terephthalate) Pores Using an Electrochemically Assisted Click Reaction. *Langmuir* **2017**, *33* (43), 11998–12006. <https://doi.org/10.1021/acs.langmuir.7b02778>.
- (168) Yang, H. C.; Hou, J.; Chen, V.; Xu, Z. K. Janus Membranes: Exploring Duality for Advanced Separation. *Angewandte Chemie - International Edition*. **2016**. <https://doi.org/10.1002/anie.201601589>.
- (169) Tian, X.; Jin, H.; Sainio, J.; Ras, R. H. A.; Ikkala, O. Droplet and Fluid Gating by Biomimetic Janus Membranes. *Adv. Funct. Mater.* **2014**, *28*, 38, 6023-6028. <https://doi.org/10.1002/adfm.201400714>.
- (170) Wang, Z.; Wang, Y.; Liu, G. Rapid and Efficient Separation of Oil from Oil-in-Water Emulsions Using a Janus Cotton Fabric. *Angew. Chemie - Int. Ed.* **2016**, *55*, 1291-1294. <https://doi.org/10.1002/anie.201507451>.
- (171) Wang, H.; Zhou, H.; Niu, H.; Zhang, J.; Du, Y.; Lin, T. Dual-Layer Superamphiphobic/Superhydrophobic-Oleophilic Nanofibrous Membranes with Unidirectional Oil-Transport Ability and Strengthened Oil-Water Separation Performance, *Adv. Mater. Interfaces* **2015**, *2* (4), 1400506. <https://doi.org/10.1002/admi.201570023>.
- (172) Vlassiouk, I.; Siwy, Z. S. Nanofluidic Diode. *Nano Lett.* **2007**, *7*, 3, 552-556. <https://doi.org/10.1021/nl062924b>.
- (173) Zhang, H.; Hou, X.; Zeng, L.; Yang, F.; Li, L.; Yan, D.; Tian, Y.; Jiang, L. Bioinspired Artificial Single Ion Pump. *J. Am. Chem. Soc.* **2013**, *135*, 43, 16102-16110. <https://doi.org/10.1021/ja4037669>.
- (174) Schachtschneider, A.; Wessig, M.; Spitzbarth, M.; Donner, A.; Fischer, C.; Drescher, M.; Polarz, S. Directional Materials-Nanoporous Organosilica Monoliths with Multiple Gradients Prepared Using Click Chemistry. *Angew. Chemie Int. Ed.* **2015**, *54* (36), 10465–10469. <https://doi.org/10.1002/anie.201502878>.
- (175) Yang, H.-C.; Hou, J.; Wan, L.-S.; Chen, V.; Xu, Z.-K. Janus Membranes with Asymmetric Wettability for Fine Bubble Aeration. *Adv. Mater. Interfaces* **2016**, *3* (9), 1500774. <https://doi.org/10.1002/admi.201500774>.
- (176) Genzer, J.; Bhat, R. R. Surface-Bound Soft Matter Gradients. *Langmuir* **2008**, *24*, 6, 2294-2317. <https://doi.org/10.1021/la7033164>.
- (177) Polcari, D.; Dauphin-Ducharme, P.; Mauzeroll, J. Scanning Electrochemical Microscopy: A Comprehensive Review of Experimental Parameters from 1989 to 2015. *Chemical Reviews*. **2016**, *116*, 22, 13234-13278. <https://doi.org/10.1021/acs.chemrev.6b00067>.
- (178) Krabbenborg, S. O.; Huskens, J. Electrochemically Generated Gradients. *Angew. Chemie Int. Ed.* **2014**, *53* (35), 9152–9167. <https://doi.org/10.1002/anie.201310349>.
- (179) Nicosia, C.; Krabbenborg, S. O.; Chen, P.; Huskens, J. Shape-Controlled Fabrication of Micron-Scale Surface Chemical Gradients via Electrochemically Activated Copper(I) “Click” Chemistry. *J. Mater. Chem. B* **2013**, *1* (40), 5417. <https://doi.org/10.1039/c3tb20902d>.
- (180) Krabbenborg, S. O.; Nicosia, C.; Chen, P.; Huskens, J. Reactivity Mapping with

- Electrochemical Gradients for Monitoring Reactivity at Surfaces in Space and Time. *Nat. Commun.* **2013**, *4*, 1667. <https://doi.org/10.1038/ncomms2688>.
- (181) Rostovtsev, V. V.; Green, L. G.; Fokin, V. V.; Sharpless, K. B. A Stepwise Huisgen Cycloaddition Process: Copper(I)-Catalyzed Regioselective “Ligation” of Azides and Terminal Alkynes. *Angew. Chemie Int. Ed.* **2002**, *41* (14), 2596–2599. [https://doi.org/10.1002/1521-3773\(20020715\)41:14<2596::AID-ANIE2596>3.0.CO;2-4](https://doi.org/10.1002/1521-3773(20020715)41:14<2596::AID-ANIE2596>3.0.CO;2-4).
- (182) Tornøe, C. W.; Christensen, C.; Meldal, M. Peptidotriazoles on Solid Phase: [1,2,3]-Triazoles by Regiospecific Copper(I)-Catalyzed 1,3-Dipolar Cycloadditions of Terminal Alkynes to Azides. *J. Org. Chem.* **2002**, *67* (9), 3057–3064. <https://doi.org/10.1021/jo011148j>.
- (183) Meldal, M.; Tomøe, C. W. Cu-Catalyzed Azide - Alkyne Cycloaddition. *Chemical Reviews.* **2008**, *108*, 8, 2952-3015. <https://doi.org/10.1021/cr0783479>.
- (184) Schlossbauer, A.; Schaffert, D.; Kecht, J.; Wagner, E.; Bein, T. Click Chemistry for High-Density Biofunctionalization of Mesoporous Silica. *J. Am. Chem. Soc.* **2008**, *130*, 38, 12558-12559. <https://doi.org/10.1021/ja803018w>.
- (185) Nakazawa, J.; Stack, T. D. P. Controlled Loadings in a Mesoporous Material: Click-on Silica. *J. Am. Chem. Soc.* **2008**, *130*, 44, 14360-14361. <https://doi.org/10.1021/ja804237b>.
- (186) Chatelet, B.; Joucla, L.; Dutasta, J.-P.; Martinez, A.; Dufaud, V. Immobilization of a N-Substituted Azaphosphatrane in Nanopores of SBA-15 Silica for the Production of Cyclic Carbonates. *J. Mater. Chem. A* **2014**, *2* (34), 14164–14172. <https://doi.org/10.1039/C4TA01500B>.
- (187) Guan, B.; Ciampi, S.; Le Saux, G.; Gaus, K.; Reece, P. J.; Gooding, J. J., Different Functionalization of the Internal and External Surfaces in Mesoporous Materials for Biosensing Applications Using “Click” Chemistry. *Langmuir* **2011**, *27* (1), 328–334. <https://doi.org/10.1021/la102599m>.
- (188) Ciampi, S.; Bocking, T.; Kilian, K. A.; Harper, J. B.; Gooding, J. J. Click Chemistry in Mesoporous Materials: Functionalization of Porous Silicon Rugate Filters. *Langmuir* **2008**, *24*, 11, 5888-5892. <https://doi.org/10.1021/la800435d>.
- (189) Guo, F.; Jankova, K.; Schulte, L.; Vigild, M. E.; Ndoni, S. Surface Modification of Nanoporous 1,2-Polybutadiene by Atom Transfer Radical Polymerization or Click Chemistry. *Langmuir* **2010**, *26* (3), 2008–2013. <https://doi.org/10.1021/la9025443>.
- (190) Devaraj, N. K.; Dinolfo, P. H.; Chidsey, C. E. D.; Collman, J. P. Selective Functionalization of Independently Addressed Microelectrodes by Electrochemical Activation and Deactivation of a Coupling Catalyst. *J. Am. Chem. Soc.* **2006**, *128* (6), 1794–1795. <https://doi.org/10.1021/ja058380h>.
- (191) Cañete, S. J. P.; Lai, R. Y. Fabrication of an Electrochemical DNA Sensor Array via Potential-Assisted “Click” Chemistry. *Chem. Commun.* **2010**, *46* (22), 3941. <https://doi.org/10.1039/c002371j>.
- (192) Ku, S.-Y.; Wong, K.-T.; Bard, A. J. Surface Patterning with Fluorescent Molecules Using Click Chemistry Directed by Scanning Electrochemical Microscopy. *J. Am. Chem. Soc.* **2008**, *130* (8), 2392–2393. <https://doi.org/10.1021/ja078183d>.
- (193) Hansen, T. S.; Lind, J. U.; Daugaard, A. E.; Hvilsted, S.; Andresen, T. L.; Larsen, N. B. Complex Surface Concentration Gradients by Stenciled “Electro Click Chemistry.” *Langmuir* **2010**. <https://doi.org/10.1021/la102652p>.
- (194) Shida, N.; Ishiguro, Y.; Atobe, M.; Fuchigami, T.; Inagi, S. Electro-Click Modification of Conducting Polymer Surface Using Cu(I) Species Generated on a Bipolar Electrode in a

- Gradient Manner. *ACS Macro Lett.* **2012**, *1* (6), 656–659.
<https://doi.org/10.1021/mz300210w>.
- (195) Baker, L. A.; Jin, P.; Martin, C. R. Biomaterials and Biotechnologies Based on Nanotube Membranes. *Critical Reviews in Solid State and Materials Sciences.* **2005**, *30*, 183–205.
<https://doi.org/10.1080/10408430500198169>.
- (196) Marchand-Brynaert, J.; Deldime, M.; Dupont, I.; Dewez, J.-L.; Schneider, Y.-J. Surface Functionalization of Poly(Ethylene Terephthalate) Film and Membrane by Controlled Wet Chemistry: Chemical Characterization of Carboxylated Surfaces. *J. Colloid Interface Sci.* **1995**, *173* (1), 236–244. <https://doi.org/10.1006/jcis.1995.1319>.
- (197) Geismann, C.; Ulbricht, M. Photoreactive Functionalization of Poly(Ethylene Terephthalate) Track-Etched Pore Surfaces with "Smart" Polymer Systems. *Macromol. Chem. Phys.* **2005**, *206* (2), 268–281. <https://doi.org/10.1002/macp.200400374>.
- (198) Chan, T. R.; Hilgraf, R.; Sharpless, K. B.; Fokin, V. V. Polytriazoles as Copper(I)-Stabilizing Ligands in Catalysis. *Org. Lett.* **2004**, *6*, 17, 2853–2855.
<https://doi.org/10.1021/ol0493094>.
- (199) Scopece, P.; Baker, L. A.; Ugo, P.; Martin, C. R. Conical Nanopore Membranes: Solvent Shaping of Nanopores. *Nanotechnology* **2006**, *17* (15), 3951–3956.
<https://doi.org/10.1088/0957-4484/17/15/057>.
- (200) Xu, H.; Minter, C. J.; Nagasaka, S.; Ito, T.; Higgins, D. A. Elongation, Alignment, and Guided Electrophoretic Migration of Ds-DNA in Flow-Aligned Hexagonal F127 Gels. *J. Phys. Chem. B* **2014**, *118* (15), 4151–4159. <https://doi.org/10.1021/jp501175h>.
- (201) Papra, A.; Hicke, H. G.; Paul, D. Synthesis of Peptides onto the Surface of Poly(Ethylene Terephthalate) Particle Track Membranes. *J. Appl. Polym. Sci.* **1999**, *74*, 7, 1669–1674.
[https://doi.org/10.1002/\(SICI\)1097-4628\(19991114\)74:7<1669::AID-APP9>3.0.CO;2-W](https://doi.org/10.1002/(SICI)1097-4628(19991114)74:7<1669::AID-APP9>3.0.CO;2-W).
- (202) Parlett, C. M. A.; Isaacs, M. A.; Beaumont, S. K.; Bingham, L. M.; Hondow, N. S.; Wilson, K.; Lee, A. F. Spatially Orthogonal Chemical Functionalization of a Hierarchical Pore Network for Catalytic Cascade Reactions. *Nat. Mater.* **2016**, *15*, 178–182.
<https://doi.org/10.1038/nmat4478>.
- (203) Kim, S. H.; Misner, M. J.; Xu, T.; Kimura, M.; Russell, T. P. Highly Oriented and Ordered Arrays from Block Copolymers via Solvent Evaporation. *Adv. Mater.* **2004**, *16* (3), 226–231. <https://doi.org/10.1002/adma.200304906>.
- (204) Lin, Z. Q.; Kim, D. H.; Wu, X. D.; Boosahda, L.; Stone, D.; LaRose, L.; Russell, T. P. A Rapid Route to Arrays of Nanostructures in Thin Films. *Adv. Mater.* **2002**, *14*, 19, 1373–1376. [https://doi.org/10.1002/1521-4095\(20021002\)14:19<1373::AID-ADMA1373>3.0.CO;2-F](https://doi.org/10.1002/1521-4095(20021002)14:19<1373::AID-ADMA1373>3.0.CO;2-F).
- (205) Hillmyer, M. A. Nanoporous Materials from Block Copolymer Precursors. In *Block Copolymers II*; Springer-Verlag: Berlin/Heidelberg, **2005**; pp 137–181.
https://doi.org/10.1007/12_002.
- (206) Albalak, R. J.; Capel, M. S.; Thomas, E. L. Solvent Swelling of Roll-Cast Triblock Copolymer Films. *Polymer*, **1998**, *39*, 1647–1656. [https://doi.org/10.1016/S0032-3861\(97\)00497-7](https://doi.org/10.1016/S0032-3861(97)00497-7).
- (207) Nunes, S. P. Block Copolymer Membranes for Aqueous Solution Applications. *Macromolecules* **2016**, *49* (8), 2905–2916.
<https://doi.org/10.1021/acs.macromol.5b02579>.
- (208) Yang, H.; Guo, L.; Wang, Z.; Yan, N.; Wang, Y. Nanoporous Films with Superior Resistance to Protein Adsorption by Selective Swelling of Polystyrene-Block-

- Poly(Ethylene Oxide). *Ind. Eng. Chem. Res.* **2016**, *55*, 29, 8133-8140.
<https://doi.org/10.1021/acs.iecr.6b02008>.
- (209) Banerjee, I.; Pangule, R. C.; Kane, R. S. Antifouling Coatings: Recent Developments in the Design of Surfaces That Prevent Fouling by Proteins, Bacteria, and Marine Organisms. *Advanced Materials*. **2011**, *23*, 690-718.
<https://doi.org/10.1002/adma.201001215>.
- (210) Lowe, S.; O'Brien-Simpson, N. M.; Connal, L. A. Antibiofouling Polymer Interfaces: Poly(Ethylene Glycol) and Other Promising Candidates. *Polymer Chemistry*. **2015**, *6*, 198-212. <https://doi.org/10.1039/c4py01356e>.
- (211) Errede, L. A., A Molecular Interpretation of Polymer Swelling. *J. Phys. Chem.* **1989**, *93*(6), 2668–2671. <https://doi.org/10.1021/j100343a083>.
- (212) Papanu, J. S.; Hess, D. W.; Soane (Soong), D. S.; Bell, A. T. Swelling of Poly(Methyl Methacrylate) Thin Films in Low Molecular Weight Alcohols. *J. Appl. Polym. Sci.* **1990**, *39* (4), 803–823. <https://doi.org/10.1002/app.1990.070390404>.
- (213) Kang, Y.; Walsh, J. J.; Gorishnyy, T.; Thomas, E. L. Broad-Wavelength-Range Chemically Tunable Block-Copolymer Photonic Gels. *Nat. Mater.* **2007**, *6* (12), 957–960. <https://doi.org/10.1038/nmat2032>.
- (214) Masuda, T.; Kajisa, T.; Akimoto, A. M.; Fujita, A.; Nagase, K.; Okano, T.; Sakata, T.; Yoshida, R. Dynamic Electrical Behaviour of a Thermoresponsive Polymer in Well-Defined Poly(N-Isopropylacrylamide)-Grafted Semiconductor Devices. *RSC Adv.* **2017**, *7*, 55, 34517-34521. <https://doi.org/10.1039/c7ra05786e>.
- (215) Gensel, J.; Liedel, C.; Schoberth, H. G.; Tsarkova, L., "Micro-Structure-Macro-Response" Relationship in Swollen Block Copolymer Films. *Soft Matter* **2009**, *5*, 2534-2537. <https://doi.org/10.1039/b907332a>.
- (216) Zettl, U.; Knoll, A.; Tsarkova, L. Effect of Confinement on the Mesoscale and Macroscopic Swelling of Thin Block Copolymer Films. *Langmuir* **2010**, *26*, 9, 6610-6617. <https://doi.org/10.1021/la903922y>.
- (217) Vogt, B. D.; Soles, C. L.; Jones, R. L.; Wang, C.-Y.; Lin, E. K.; Wu, W.; Satija, S. K.; Goldfarb, D. L.; Angelopoulos, M. Interfacial Effects on Moisture Absorption in Thin Polymer Films. *Langmuir* **2004**, *20*(13), 5285–5290. <https://doi.org/10.1021/la035830f>.
- (218) Mukherjee, M.; Singh, A.; Daillant, J.; Menelle, A.; Cousin, F. Effect of Solvent–Polymer Interaction in Swelling Dynamics of Ultrathin Polyacrylamide Films: A Neutron and X-Ray Reflectivity Study. *Macromolecules* **2007**, *40* (4), 1073–1080. <https://doi.org/10.1021/ma061745d>.
- (219) Wu, W. -L.; Orts, W. J.; Hunston, D. L.; Majkrzak, C. J. Water Adsorption at a Polyimide/Silicon Wafer Interface. *Polym. Eng. Sci.* **1995**, *35*, 12, 1000-1004. <https://doi.org/10.1002/pen.760351206>.
- (220) Wang, W.; Troll, K.; Kaune, G.; Metwalli, E.; Ruderer, M.; Skrabania, K.; Laschewsky, A.; Roth, S. V.; Papadakis, C. M.; Müller-Buschbaum, P. Thin Films of Poly(N-Isopropylacrylamide) End-Capped with n-Butyltrithiocarbonate. *Macromolecules* **2008**, *41*, 9, 3209-3218. <https://doi.org/10.1021/ma7027775>.
- (221) Vogt, B. D.; Soles, C. L.; Lee, H. J.; Lin, E. K.; Wu, W. L. Moisture Absorption into Ultrathin Hydrophilic Polymer Films on Different Substrate Surfaces. *Polymer*, **2005**, *46*, 5, 1635-1342. <https://doi.org/10.1016/j.polymer.2004.11.114>.
- (222) Tang, Y.; Lu, J. R.; Lewis, A. L.; Vick, T. A.; Stratford, P. W. Structural Effects on Swelling of Thin Phosphorylcholine Polymer Films. *Macromolecules*, **2002**, *35*, 10, 3955-

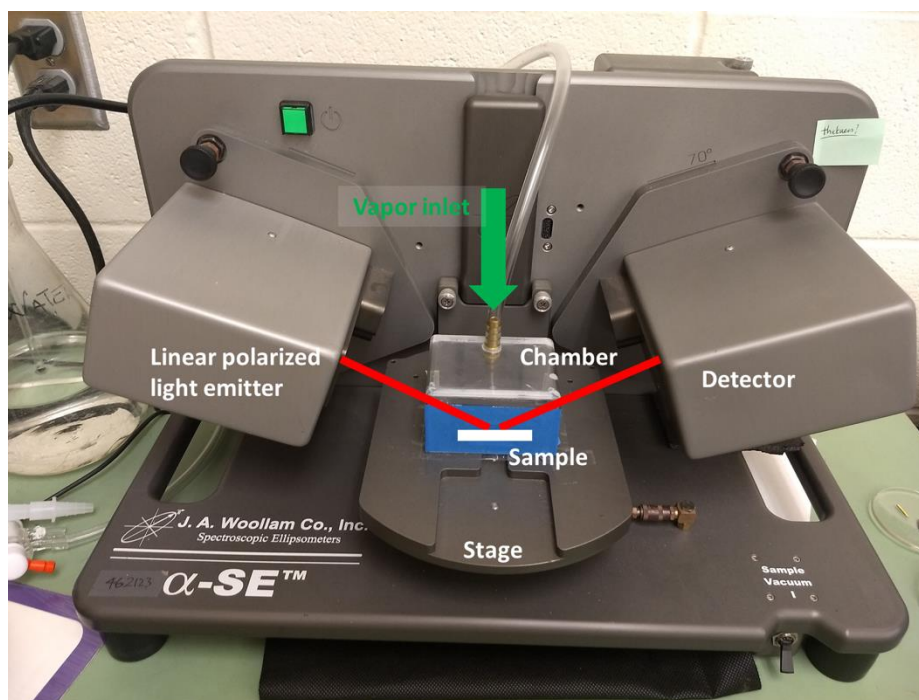
3964. <https://doi.org/10.1021/ma0117918>.
- (223) Spaeth, K.; Gauglitz, G. Characterisation of the Optical Properties of Thin Polymer Films for Their Application in Detection of Volatile Organic Compounds. *Mater. Sci. Eng. C* **1998**, *5*, 187-191. [https://doi.org/10.1016/S0928-4931\(97\)00041-6](https://doi.org/10.1016/S0928-4931(97)00041-6).
- (224) Ogieglo, W.; Wormeester, H.; Eichhorn, K. J.; Wessling, M.; Benes, N. E. In Situ Ellipsometry Studies on Swelling of Thin Polymer Films: A Review. *Progress in Polymer Science*, **2015**, *42*, 42-78. <https://doi.org/10.1016/j.progpolymsci.2014.09.004>.
- (225) Li, J.; Rao, J.; Pu, K. Recent Progress on Semiconducting Polymer Nanoparticles for Molecular Imaging and Cancer Phototherapy. *Biomaterials* **2018**, *155* (20), 217–235. <https://doi.org/10.1016/j.biomaterials.2017.11.025>.
- (226) Hoang, D. T.; Yang, J.; Paeng, K.; Kwon, Y.; Kweon, O. S.; Kaufman, L. J. In Situ Multimodal Monitoring of Solvent Vapor Swelling in Polymer Thin Films. *Rev. Sci. Instrum.* **2016**, *87* (1), 015106. <https://doi.org/10.1063/1.4939669>.
- (227) Schneider, C. A.; Rasband, W. S.; Eliceiri, K. W. NIH Image to ImageJ: 25 Years of Image Analysis. *Nature Methods*. **2012**, *7*, 671–675. <https://doi.org/10.1038/nmeth.2089>.
- (228) Haynes, W. M. *CRC Handbook of Chemistry and Physics*; CRC Press, **2011**.
- (229) Source, P. Polymer Source TM <https://www.polymersource.ca/>.
- (230) Tran-Ba, K.-H.; Higgins, D. A.; Ito, T. Single-Molecule Tracking Studies of Flow-Induced Microdomain Alignment in Cylinder-Forming Polystyrene–Poly(Ethylene Oxide) Diblock Copolymer Films. *J. Phys. Chem. B* **2014**, *118* (38), 11406–11415. <https://doi.org/10.1021/jp507594t>.
- (231) Yang, H.; Guo, L.; Wang, Z.; Yan, N.; Wang, Y. Nanoporous Films with Superior Resistance to Protein Adsorption by Selective Swelling of Polystyrene-Block-Poly(Ethylene Oxide). *Ind. Eng. Chem. Res.* **2016**, *55* (29), 8133–8140. <https://doi.org/10.1021/acs.iecr.6b02008>.
- (232) Hou, Y.; Bardo, A. M.; Martinez, C.; Higgins, D. A. Characterization of Molecular Scale Environments in Polymer Films by Single Molecule Spectroscopy. *J. Phys. Chem. B* **2000**, *104* (2), 212–219. <https://doi.org/10.1021/jp992312y>.
- (233) P, D. *CRC Handbook of Chemistry and Physics. J. Mol. Struct.* **1992**, *268* (1–3), 320. [https://doi.org/10.1016/0022-2860\(92\)85083-S](https://doi.org/10.1016/0022-2860(92)85083-S).
- (234) Del Valle-Carrandi, L.; Alegría, A.; Arbe, A.; Colmenero, J. Unexpected PDMS Behavior in Segregated Cylindrical and Spherical Nanophases of PS-PDMS Asymmetric Diblock Copolymers. *Macromolecules* **2012**, *45*, 1, 491-502. <https://doi.org/10.1021/ma202107m>.
- (235) Lodge, T. P. Celebrating 50 Years of Macromolecules. *Macromolecules*, **2017**, *50* (24), 9525–9527. <https://doi.org/10.1021/acs.macromol.7b02507>.
- (236) Sun, Z.; Russell, T. P. In Situ Grazing Incidence Small-Angle X-Ray Scattering Study of Solvent Vapor Annealing in Lamellae-Forming Block Copolymer Thin Films: Trade-off of Defects in Deswelling. *J. Polym. Sci. Part B Polym. Phys.* **2017**, *55* (13), 980–989. <https://doi.org/10.1002/polb.24346>.
- (237) Shelton, C. K.; Jones, R. L.; Dura, J. A.; Epps, T. H. Tracking Solvent Distribution in Block Polymer Thin Films during Solvent Vapor Annealing with in Situ Neutron Scattering. *Macromolecules* **2016**, *49* (19), 7525–7534. <https://doi.org/10.1021/acs.macromol.6b02046>.
- (238) Wang, M.; Ong, L.-L. S.; Dauwels, J.; Asada, H. H. Multicell Migration Tracking within Angiogenic Networks by Deep Learning-Based Segmentation and Augmented Bayesian Filtering. *J. Med. Imaging*, **2018**, *5*, 024005. <https://doi.org/10.1117/1.jmi.5.2.024005>.

- (239) Appenzeller, T. The AI Revolution in Science. *Science Mag.*, **2017**
<https://www.sciencemag.org/news/2017/07/ai-revolution-science>.
- (240) Ho, C. W. L.; Soon, D.; Caals, K.; Kapur, J. Governance of Automated Image Analysis and Artificial Intelligence Analytics in Healthcare. *Clinical Radiology*. **2019**, *74*, 5, 329-337. <https://doi.org/10.1016/j.crad.2019.02.005>.
- (241) Murphy, J. N.; Harris, K. D.; Buriak, J. M. Automated Defect and Correlation Length Analysis of Block Copolymer Thin Film Nanopatterns. *PLoS One*, **2015**, *10* (7), e0133088. <https://doi.org/10.1371/journal.pone.0133088>.
- (242) Narukawa, Y.; Ichikawa, M.; Sanga, D.; Sano, M.; Mukai, T. White Light Emitting Diodes with Super-High Luminous Efficacy. *J. Phys. D. Appl. Phys.* **2010**, *43* (35), 354002. <https://doi.org/10.1088/0022-3727/43/35/354002>.
- (243) Krantz, W. B.; Greenberg, A. R.; Kujundzic, E.; Yeo, A.; Hosseini, S. S. Evaporometry: A Novel Technique for Determining the Pore-Size Distribution of Membranes. *J. Memb. Sci.* **2013**, *438*, 153–166. <https://doi.org/10.1016/j.memsci.2013.03.045>.
- (244) Akhondi, E.; Zamani, F.; Chew, J. W.; Krantz, W. B.; Fane, A. G. Improved Design and Protocol for Evaporometry Determination of the Pore-Size Distribution. *J. Memb. Sci.* **2015**, *496*, 334–343. <https://doi.org/10.1016/j.memsci.2015.09.013>.
- (245) Zamani, F.; Akhondi, E.; Koops, G.-H.; Krantz, W. B.; Fane, A. G.; Chew, J. W. Evaporometry Adaptation to Determine the Lumen-Side Pore-Size Distribution (PSD) of Hollow Fiber and Tubular Membranes. *J. Memb. Sci.* **2017**, *526*, 1–8. <https://doi.org/10.1016/j.memsci.2016.12.024>.
- (246) Kastantin, M.; Walder, R.; Schwartz, D. K. Identifying Mechanisms of Interfacial Dynamics Using Single- Molecule Tracking. *Langmuir* **2012**, *6* (28), 12443–12456. <https://doi.org/10.1021/la3017134>.
- (247) Cai, Y.; Schwartz, D. K. Mapping the Functional Tortuosity and Spatiotemporal Heterogeneity of Porous Polymer Membranes with Super-Resolution Nanoparticle Tracking. *ACS Appl. Mater. Interfaces* **2017**, *9* (49), 43258–43266. <https://doi.org/10.1021/acsami.7b15335>.
- (248) Mabry, J. N.; Schwartz, D. K. Tuning the Flight Length of Molecules Diffusing on a Hydrophobic Surface. *J. Phys. Chem. Lett.* **2015**, *6* (11), 2065–2069. <https://doi.org/10.1021/acs.jpcclett.5b00799>.
- (249) Hassler, K.; Leutenegger, M.; Rigler, P.; Rao, R.; Rigler, R.; Gösch, M.; Lasser, T. Total Internal Reflection Fluorescence Correlation Spectroscopy (TIR-FCS) with Low Background and High Count-Rate per Molecule. *Opt. Express* **2005**, *13*, 19, 7415-7423. <https://doi.org/10.1364/opex.13.007415>.
- (250) Thompson, N. L.; Burghardt, T. P.; Axelrod, D. Measuring Surface Dynamics of Biomolecules by Total Internal Reflection Fluorescence with Photobleaching Recovery or Correlation Spectroscopy. *Biophys. J.* **1981**, *33* (3), 435–454. [https://doi.org/10.1016/S0006-3495\(81\)84905-3](https://doi.org/10.1016/S0006-3495(81)84905-3).
- (251) Weger, L.; Hoffmann-Jacobsen, K. A Total Internal Reflection-Fluorescence Correlation Spectroscopy Setup with Pulsed Diode Laser Excitation. *Rev. Sci. Instrum.* **2017**, *88* (9), 093102. <https://doi.org/10.1063/1.4986235>.
- (252) Ries, J.; Schwille, P. New Concepts for Fluorescence Correlation Spectroscopy on Membranes. *Physical Chemistry Chemical Physics*. **2008**, *10*, 3487-3497. <https://doi.org/10.1039/b718132a>.

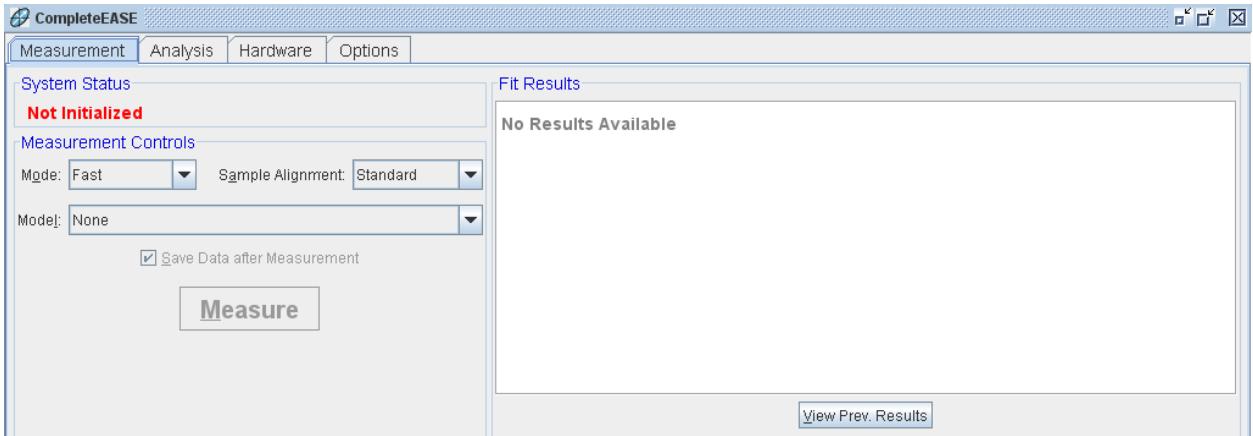
Appendix A -Spectroscopic Ellipsometry in Time-

In Chapter 5, spectroscopic ellipsometry data were recorded as a function of time to assess the effects of solvent vapor exposure on the thickness and refractive index of polymer thin films. For such measurements, the software needs to set up according to the following steps explained in this appendix.

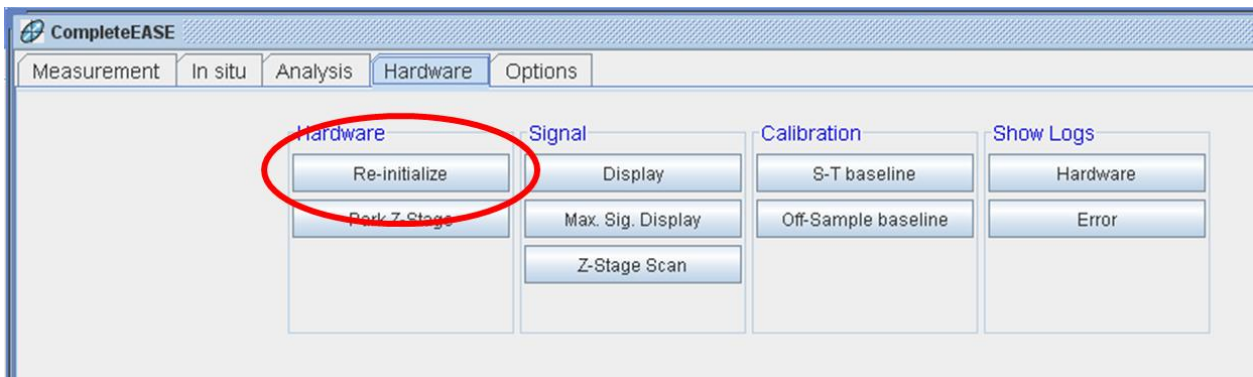
1. The picture below shows a setup for ellipsometry measurements in a vapor chamber. An inlet to flow gas or vapor into the chamber is shown in green, and a beam path for ellipsometry measurements is shown in red for clarification.



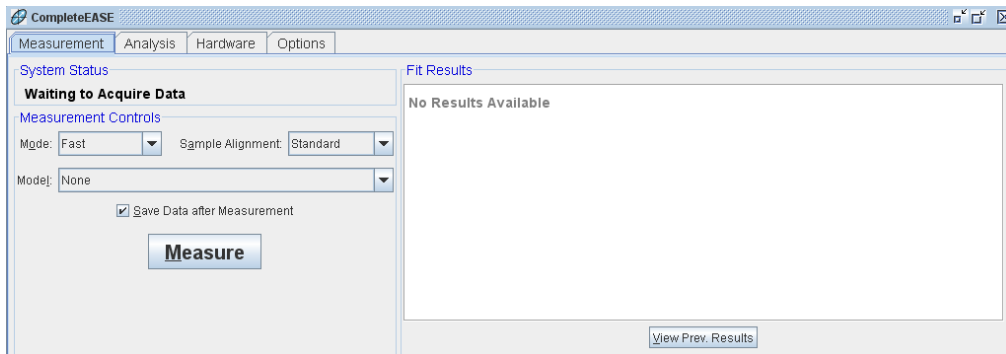
2. Open completeEASE® software , **only once the ellipsometer is on**. Once opened the app, the screen will show the following window:



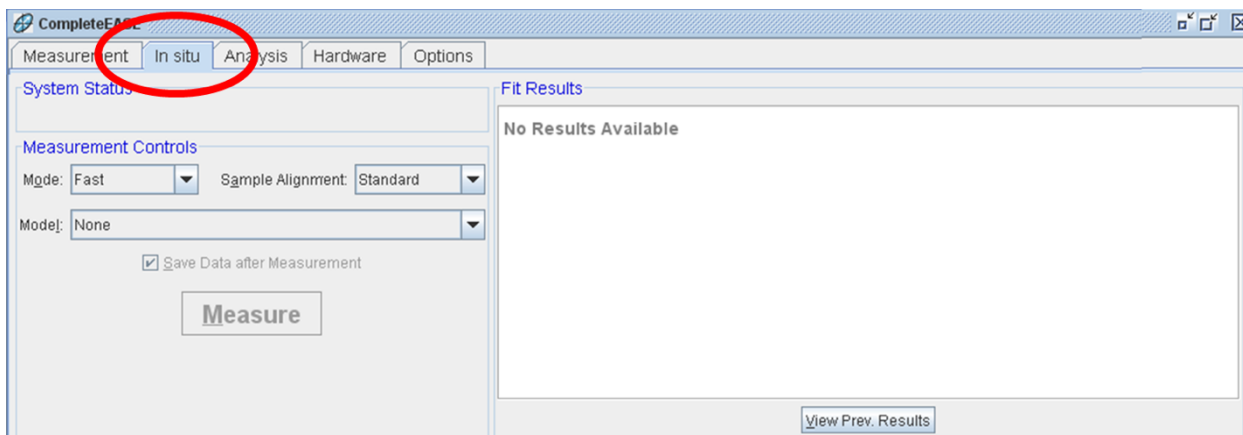
3. If the system status is “**Not Initialized**” (as it is in the above image), the user has two options: (i) Turn off the software and start again; or (ii) click in the hardware section and click “Re Initialize” in the tab (mark in the image below).



4. After the initialization, the windows must look as:



5. Once the system is properly working, the user must press “Ctrl + Shift + Alt + I” to open the hidden “In situ” tab. The new tab will appear as shown in the image bellow.



6. On that tab, the options are identical to the regular “Measurement” tab.

Mode defines the time of the data acquisition.

Sample alignment defines the position of the sample at the time of data acquisition.

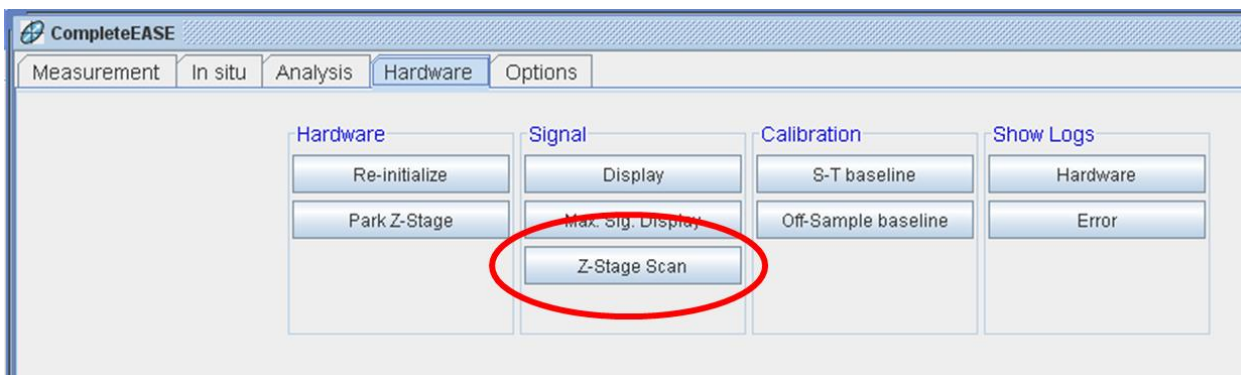
Project indicates the folder where the data will be saved.

Model defines a model used for the fitting and calculation after the data acquisition.

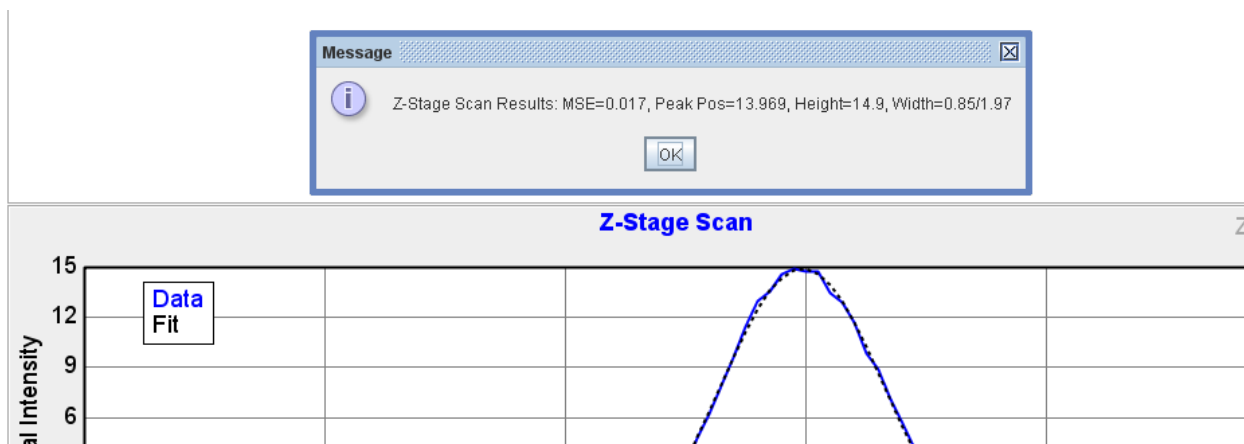
7. For continuous recording of spectroscopic ellipsometry data, the sample must remain in a fixed position (rather than a regular mode that has the instrument optimize the vertical position of the sample prior to each measurement) for the following two reasons. First, the (vertical) motion of the stage may disrupt the beam path that must pass through holes in the chamber. Second, the measurements at a fixed sample position permits one to record ellipsometry data at a higher time

resolution, which is needed for kinetics measurements. To set the stage in a fixed position, first the initial position of the sample must be verified.

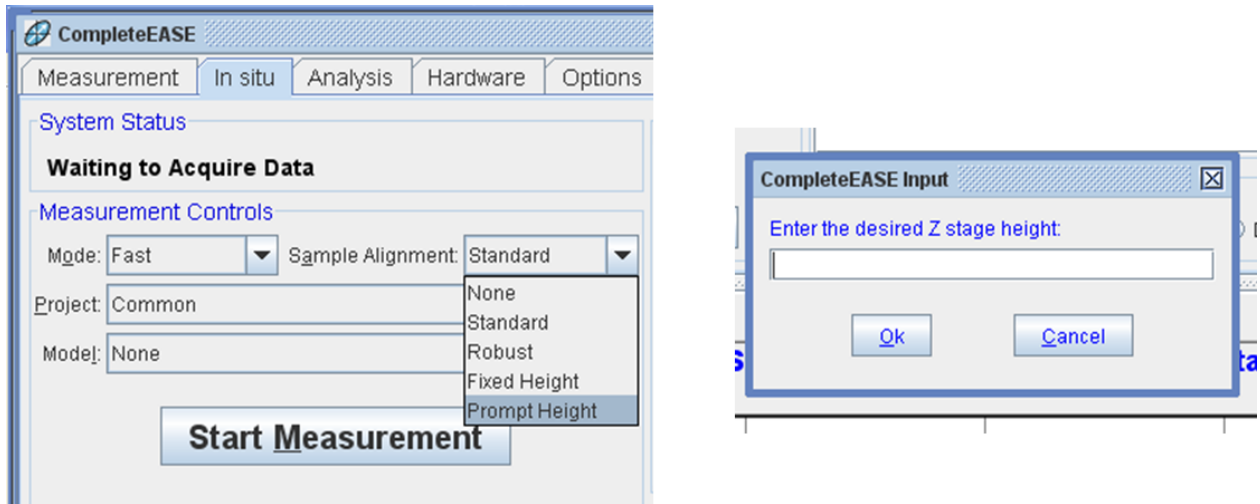
8. After the sample is in position and the chamber is aligned, go to “**Hardware**” tab and select “**Z-Stage Scan**”.



9. This command measures detector intensity as a function of Z position (vertical axis). Once the scan is done, the position of the stage will be shown in the screen. *Take note of the stage height value (peak pos).*

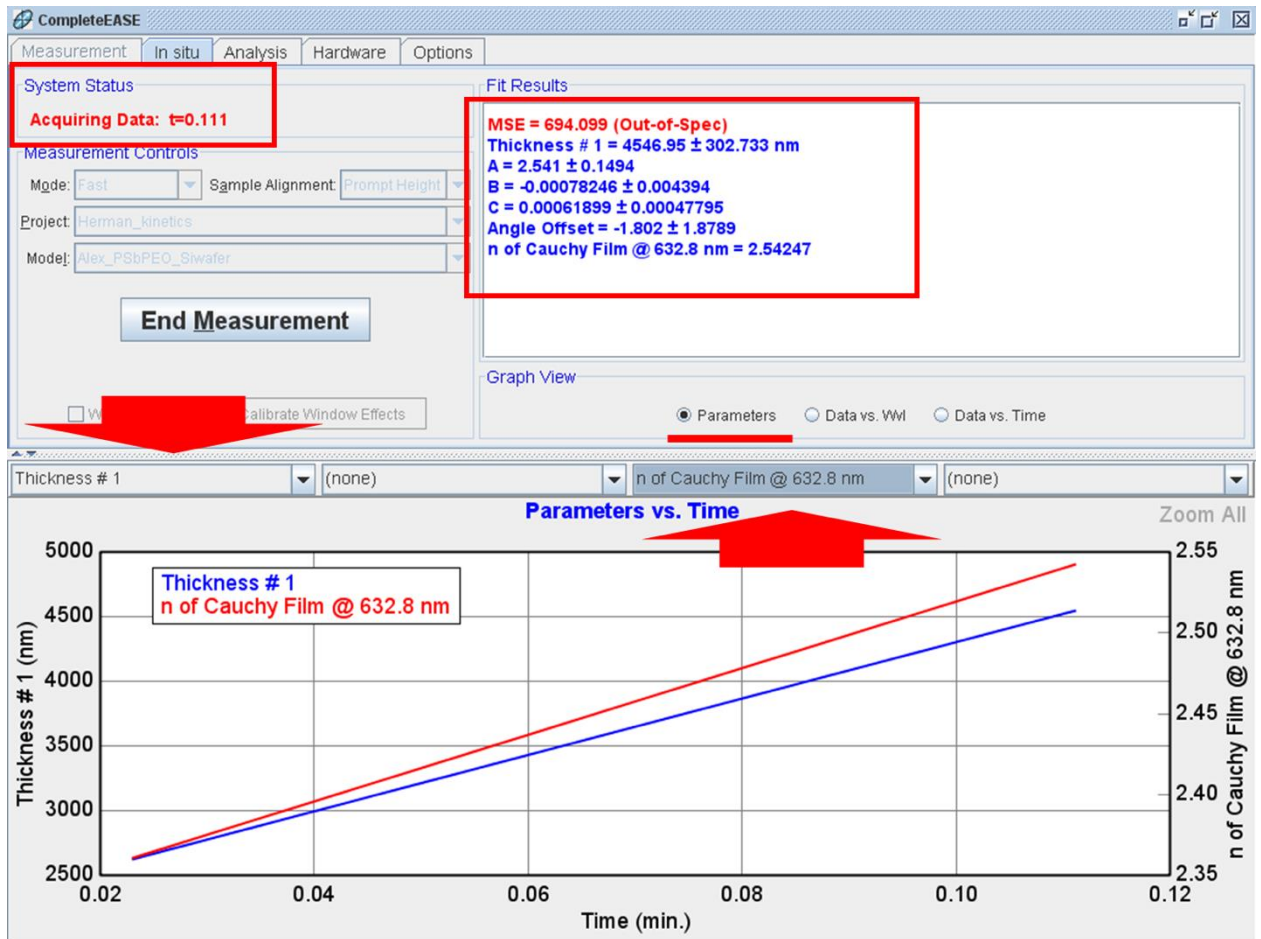


10. With the stage position noted (peak pos value), go to “**In situ**” tab to start the measurement. Under “**Mode**”, select “**Fast**”, under “**Sample Alignment**”, select “**Prompt position**”, and select a proper model for the sample to be measured.



11. Click “**Start Measurement**” when ready and a dialogue box will pop up asking for the stage position, complete with the value noted. Another window will pop up asking for destination and file name for the data. Select the proper one.

12. The data acquisition will start after selecting the right destination and file name, however the software had a problem and it cannot display the thickness and refractive index at the same plot. This problem can be overcome by clicking “**Stop Measurement**” and “**Start Measurement**” again. It will ask again for stage position and file destination and name. Overwrite the previous data to avoid repetitions. To show the values as a function of time, select the options: Thickness #1 and n of Cauchy film #1 (as marked below).



It is worth to mention that the complete result for each data point will be displayed as usual on the top right window, as well as **time of the data acquisition** (Acquiring Data, see top left in the above image). Time resolution of the data set can be obtained by subtracting two consecutive **time of the data acquisition** values.

13. Once finished, the data acquisition and measurement is stopped. Right click on the plot to open the display and select “**Copy data to clipboard**” to get the data as a “thickness (nm) vs. time (min)” plot.



14. The data will be saved as a series of single measurements that need to be opened by the software to obtain parameters of interest from the box after applying the proper model.